Origins of Strength and Ductility in Mg-RE Binary Alloys

ORIGINS OF STRENGTH AND DUCTILITY IN MG-RE BINARY ALLOYS

BY

KEVIN NOBLE, B.Eng. & Mgmt.

A THESIS

SUBMITTED TO THE DEPARTMENT OF MATERIALS SCIENCE & ENGINEERING

AND THE SCHOOL OF GRADUATE STUDIES

OF MCMASTER UNIVERSITY

IN PARTIAL FULFILMENT OF THE REQUIREMENTS

FOR THE DEGREE OF

MASTER OF APPLIED SCIENCE

Master of Applied Science (2011)   McMaster University

(Materials Science & Engineering)   Hamilton, Ontario, Canada

TITLE: Origins of Strength and Ductility in Mg-RE Binary Al-
                    loys

AUTHOR: Kevin Noble
                    B.Eng. & Mgmt., (Materials Science and Engineering)
                    McMaster University, Hamilton, ON, Canada

SUPERVISOR: Dr. Marek Niewczas

NUMBER OF PAGES: xvii, 142

To my family and friends

Abstract

With the poor room temperature formability of magnesium, rare earth (RE) additions have proven a promising avenue for wrought magnesium products. However, not much is known regarding the effect of these elements on strength and ductility. Stanford *et al.* (2010b) summarized it best: "Although the addition of rare earth elements offers the possibility of greatly improved mechanical properties, we still lack fairly basic knowledge about the behaviour of these alloying elements"[p.6773]. Through a systematic study across three Mg-RE binary systems, the effect of gadolinium, samarium and scandium on solution strengthening, work hardening behaviour and strain rate sensitivity of Mg-RE binary alloys have been characterized.

The results suggest that samarium offers the greatest solid solution strengthening in both tension and compression relative to the other two binary systems. For the binary alloys explored, only gadolinium and samarium in compression followed the Labusch theory of solution strengthening; in which the yield strength scales with $c^{\frac{2}{3}}$. Gadolinium additions provide the largest strength and ductility in tension and compression. Increasing solute content in the binary systems leads to a decrease of the strain rate sensitivity of the alloys. At the highest level of solute, both Mg-Gd and Mg-Sm exhibit negative strain rate sensitivity under tension. In compression, Mg-Gd also exhibits a negative strain rate sensitivity at the highest level solute, whereas Mg-Sm has a low, but positive value. The asymmetry in

work hardening behaviour and the form of the flow curves between tension and compression is the result of the difference in the dominating modes of deformation at a given stage of the plastic flow. The extent of the work performed established the hardening levels and thermodynamic deformation parameters which control the flow stress and work hardening behaviour, that can be applied in future work.

Acknowledgements

I would like to thank my family, friends, and classmates for the support they threw behind me in the pursuit of higher education. With their encouragement, I was able to facilitate working relationships with many people at McMaster that enabled me to complete my research, and become a more rounded Materials Scientist. Special thanks to my professor, Marek Niewczas, for support and guidance, and ultimately the opportunity to work towards my Master's degree. Additionally, much of the experimental work and analysis couldn't have been acheived with out the help of Dr. Zohreh Keshavarz. Her expertise within the field, and her devotion to sharing her knowledge allowed me to get up to speed and become productive far quicker than I would have been able to do solo. Although a late addition to the research group within Dr. Niewczas's group, Anna Kula's contributions have helped me add additional information to my thesis. By continuing the next stage of the research, and being so gracious to complete a few XRD experiments, Anna has allowed me to complete a few loose ends in the analysis of the body of work I have focused on in the past two years. Finally, the support of technical staff such as Doug Culley, and Jim Garett allowed for out-side of the box thinking to solve problems I encountered in my research.

Thank you to all those inside and outside of the Department of Materials Science and Engineering that has made all of this possible. I hope to one day be able to give back my

time and effort to those in a similar position as myself, as you have done for me.

Contents

List of Tables

List of Figures

Chapter 1

Introduction

1.1 Objective.

With the poor room temperature formability of magnesium, rare earth (RE) additions have proven a promising avenue for wrought magnesium products. However, not much is known regarding the effect of these elements on strength and ductility. Stanford *et al.* (2010b) summarized it best:

> Although the addition of rare earth elements offers the possibility of greatly improved mechanical properties, we still lack fairly basic knowledge about the behaviour of these alloying elements.(Stanford *et al.*, 2010b, p.6773)

Through a systematic study across three Mg-RE binary systems, the effect of gadolinium (Gd), samarium (Sm), and scandium (Sc) on solution strengthening, work hardening behaviour and strain rate sensitivity of Mg-RE binary alloys are to be examined. This fundamental research will be the basis for future exploration in alloying magnesium with rare earth additions.

1.2   Binary Systems.

It was reported by McDonald (1940) and Leontis (1951) that the addition of certain rare earth elements increases the ductility of magnesium (Stanford and Barnett, 2008). These rare earth elements are classified as elements from atomic number 57 through 71, with yttrium and scandium included in the classification (Rokhlin, 2003). The lanthanoid series rare earth elements are classified into two subgroups, the cerium subgroup (La, Ce, Pr, Nd, Sm, Eu), and the yttrium subgroup (Gd, Tb, Dy, Ho, Er, Tm). Additions of rare earth elements increase the strength of magnesium alloys mainly through precipitation hardening and solid solution strengthening (Gao *et al.*, 2009). The solubility of the rare earth elements in solid magnesium is depicted in Figure 1.1 (Rokhlin, 1998). It can be seen that the subgroups exhibit different solid solubility, with the cerium subgroup having very minimal solid solubility in solid magnesium, and the yttrium subgroup having medium to large solid solubility in solid magnesium. Trends within the subgroups can also be observed; with increasing atomic number (with the exception of Eu, and Tm) there is an increase in the solid solubility (Rokhlin, 1998). These solid solubility trends within the rare earth metals, combined with the age hardening response (discussed in Section 1.2.1), provided a starting point for the binary systems explored.

1.2.1   Magnesium-Gadolinium (Mg-Gd).

Gadolinium is classified under the yttrium-subgroup of the lanthanide rare earth series, with medium solubility in solid magnesium, as depicted in the Mg-Gd phase diagram in Figure 1.2 (Rokhlin, 2003). The maximum solid solubility of gadolinium in solid magnesium is 23.0 wt% (Rokhlin, 2003).
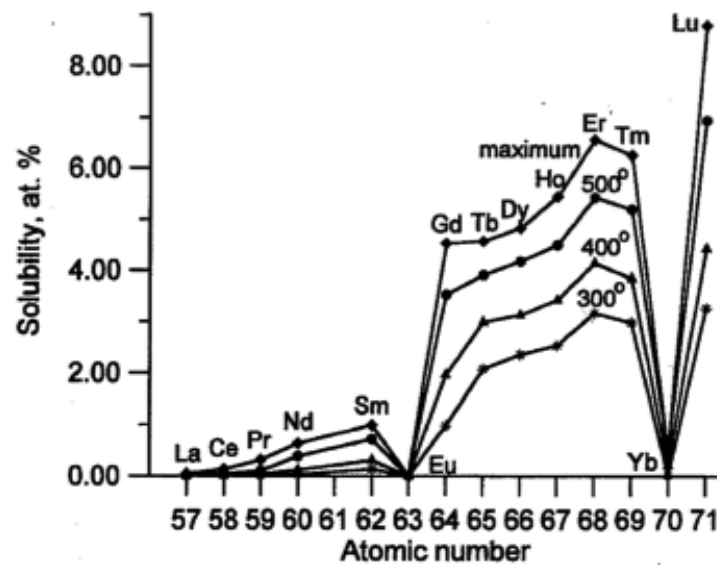
Figure 1.1: Solubility of Rare Earth Metals in solid magnesium as a function of the atomic number of the rare earth metal. (Rokhlin, 1998, p.142)

As shown in Figure 1.1 (Rokhlin, 1998), gadolinium has the lowest solid solubility of the yttrium subgroup, thus it is expected that the solid solution strengthening of gadolinium in magnesium will be less than all other elements of the sub-group. However, it is the ageing response that has attracted interest in this alloying system, with gadolinium displaying the greatest age hardening response of both the lanthanide subgroups (Rokhlin, 2003).

1.2.2   Magnesium-Samarium (Mg-Sm).

Samarium is classified under the cerium-subgroup of the lanthanide rare earth series, with very low solubility in solid magnesium, as depicted in the Mg-Sm phase diagram in Figure 1.3 (Rokhlin, 2003). The maximum solid solubility of samarium in magnesium is 5.8 wt % (Rokhlin, 2003). As shown in Figure 1.1 (Rokhlin, 1998), samarium has the highest solid
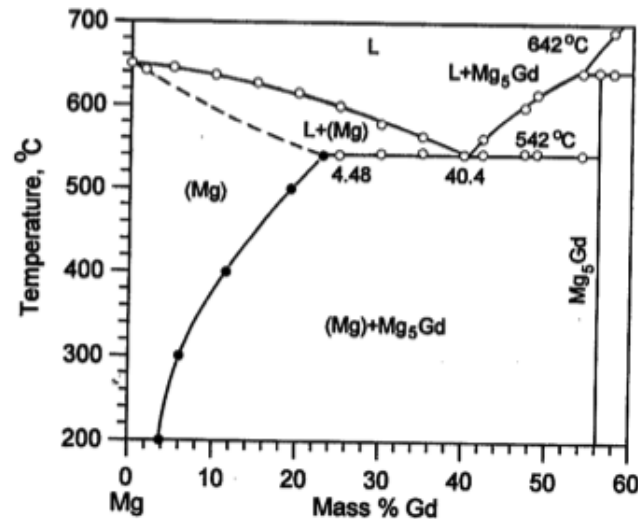
Figure 1.2: Mg-rich side of the Mg-Gd phase diagram. (Rokhlin, 2003, p.44)

solubility of the cerium subgroup. Thus it is expected that the solid solution strengthening of samarium in magnesium will be greater than all other elements of the sub-group.

1.2.3   Magnesium-Scandium (Mg-Sc).

The addition of scandium to magnesium has received growing interest recently due to its improved mechanical properties (Pisch *et al.*, 1998), and its superior creep resistance compared to other magnesium alloys (Mordike, 2001). Although scandium does not belong to the cerium or yttrium subgroup, and has a lower atomic number than those elements, it is still considered a rare earth element due to its lack of abundance in the earth's crust (Rokhlin, 2003). The classical phase diagram is presented below in Figure 1.4 (Rokhlin, 2003, p.64), which depicts a peritectic transformation, as well as a large range of solid solubility ($\approx$16 at% Sc) in magnesium.
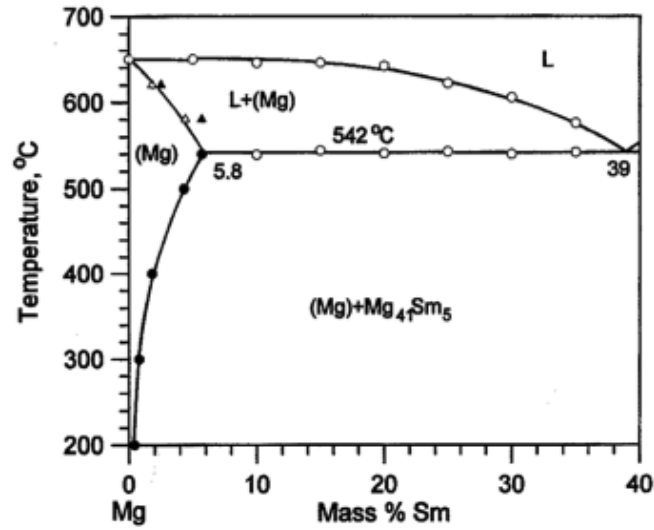
Figure 1.3: Mg-rich side of the Mg-Sm phase diagram. (Rokhlin, 2003, p.39)
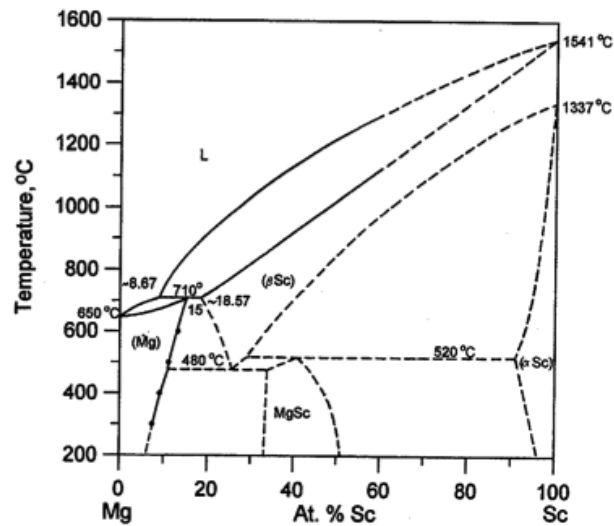
Figure 1.4: Mg-Sc phase diagram.(Rokhlin, 2003, p.64)

The dashed lines on the phase diagram (Figure 1.4) represent calculated regions, as opposed to experimentally obtained results. This uncertainty, although prevalent in the Sc-rich area of the phase diagram, is also present in the Mg-rich area of the phase diagram. The lack of information regarding the decomposition of the super saturated solution led Pisch *et al.* (1998), to re-evaluate the Mg-rich side of the Mg-Sc phase diagram. Figure 1.5 depicts the revised phase diagram obtained experimentally (Pisch *et al.*, 1998, p.475). The sharp decrease in solid solubility with decreasing temperature now poises this binary system for potential age hardening via the decomposition of the super saturated solid solution.
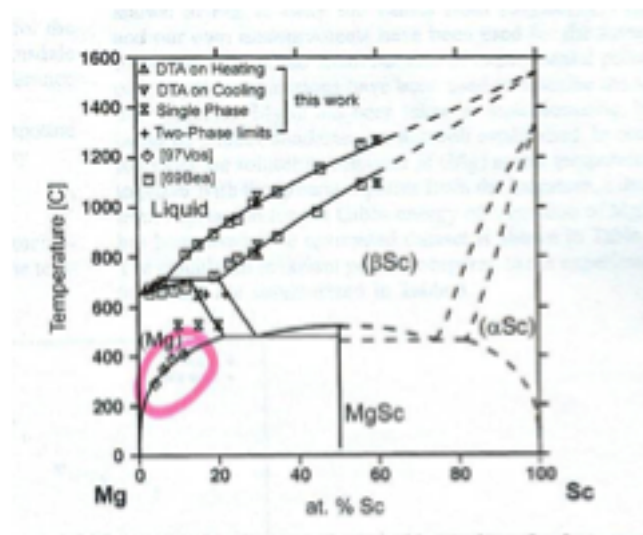
Figure 1.5: Updated Mg-Sc phase diagram.(Pisch *et al.*, 1998, p.475)

1.2.4   Age-Hardening Response of Rare Earth Alloys.

With decreasing solid solubility of rare earth elements in solid magnesium with decreasing temperatures, solutionized alloys can exhibit improved mechanical properties through precipitation hardening. Just as the solid solubility was seen in the previous sections to depend on which lanthanide sub-group a particular element belonged to, so does the age-hardening response (Rokhlin, 2006). The binary Mg-RE ageing response for select compositions is depicted below in Figure 1.6, with the top graph displaying the yttrium-sub group, and the bottom graph displaying the cerium-sub group(Rokhlin, 2006, p.488).
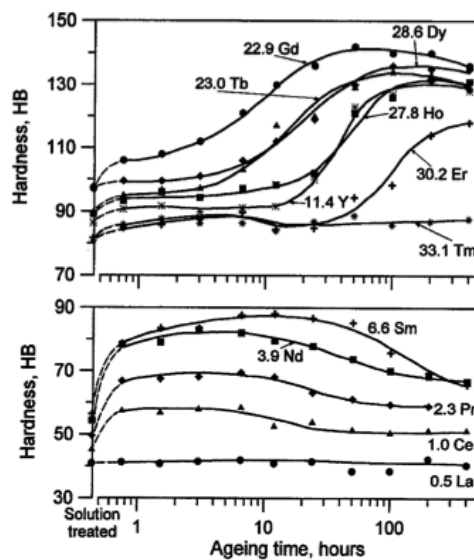
(a) Top graph depicts the yttrium subgroup, lower graph depicts the cerium subgroup; the content of elements is reported in wt%.

Figure 1.6: Variation of the hardness of solid-solution-hardened binary magnesium alloys in the process of ageing at 200°C.(Rokhlin, 2006, p.488)

From Figure 1.6, it can be seen that the two sub-groups differ greatly in the ultimate hardness achieved, and the time required to do so. The cerium sub-group rapidly increases

hardness in a short ageing time, and reach peak hardness in only a few hours. Conversely, the yttrium sub-group has a long incubation period before significant hardness increases are seen. Although the ageing response is delayed in the yttrium sub-group, the elements reach greater peak aged hardness than elements in the cerium sub-group (Rokhlin, 2006). The differences in the two sub-group ageing times is attributed to the rate of decomposition, with elements in the yttrium sub-group having a greatly decreased rate compared to the cerium sub-group. Trends within the sub-groups can also be observed, with increasing atomic number in the cerium sub-group results in increased peak aged hardness, whereas the yttrium sub-group displays decreasing peak aged hardness with increasing atomic number (Rokhlin, 2006). The trend in the cerium sub-group is attributed to increased solid solubility in solid magnesium with increasing atomic number, whereas the reasons for the decreasing hardness with increasing atomic number in the yttrium have not been sufficiently explained (Rokhlin, 2003).

1.3   Texture Evolution.

Senn and Agnew (2008) reported that the mechanical properties of magnesium alloys are "strongly affected by the presence of crystallographic texture" (Senn and Agnew, 2008, p.153). The texture evolution of magnesium alloys is a consequence of basal slip and extension twinning required to accommodate processing (Senn and Agnew, 2008). These deformation mechanisms align the c-axis perpendicular to applied tensile strains, or for sheet and plate, the c-axis align in the normal direction to sheet plane (Senn and Agnew, 2008). Senn and Agnew (2008, p.153), state that "there is both experimental and theoretical evidence that if the texture of wrought magnesium alloys could be reduced, it would

lead to an improvement in formability" for magnesium alloys. The basal texture evolution of a non rare earth containing magnesium alloy (ZK41) is shown in Figure 1.7(Senn and Agnew, 2008, p.157). Deformation alters the alignment of the basal poles 20 degrees away from the normal direction of the plane, towards the rolling direction (Senn and Agnew, 2008). After deformation, thermal processes are employed that result in minimal changes in the basal pole intensity, and tilt towards the rolling direction is reduced, bringing the greatest basal pole intensity back to perpendicular with the plane normal direction.
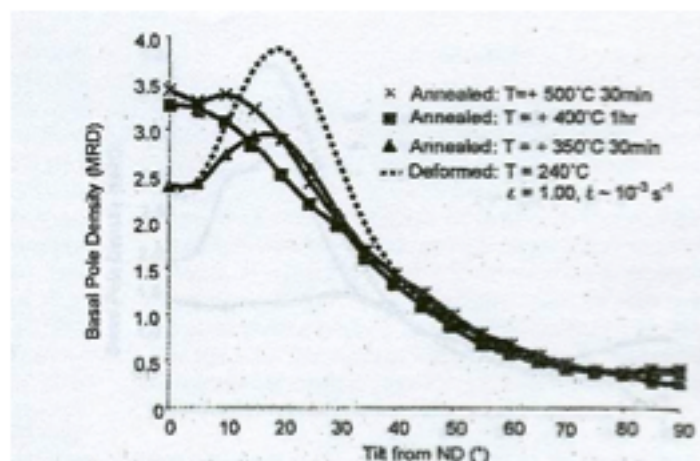
Figure 1.7: Basal texture evolution during annealing of ZK41.(Senn and Agnew, 2008, p.157)

Stanford and Barnett (2008, p.399) reported that, recent work on annealing textures has shown that it is difficult to dramatically alter the texture through changes in thermo-mechanical processing. This behaviour was displayed in Figure 1.7, as the basal pole intensity was not significantly altered with annealing cycles (Senn and Agnew, 2008). It was continued that, "composition can significantly modify the texture. Micro-alloying with

rare earth elements can weaken the extrusion texture, and can also change the orientation of the highest intensity peak of texture" (Stanford and Barnett, 2008, p.399). The texture evolution of deformed magnesium alloys containing rare earth additions exhibits identical behaviour of magnesium alloys without rare earth additions (Senn and Agnew, 2008). The deformed structure, as shown as the dashed lines in Figure 1.8, shows a tilt from the normal direction of 20° (Senn and Agnew, 2008). With subsequent annealing cycles, the intensity of the basal pole decreases, and orientation specific intensity also decreases.
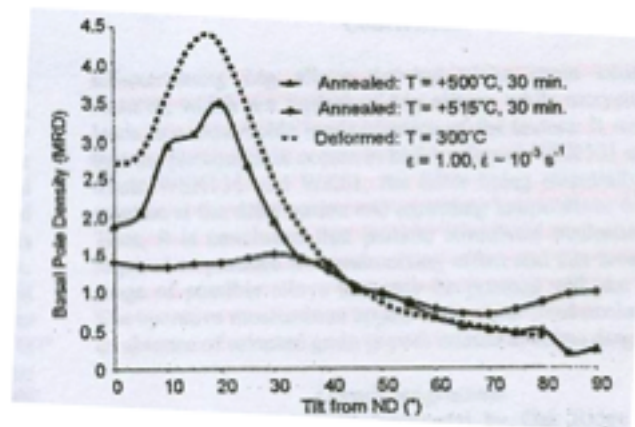
Figure 1.8: Basal texture evolution during annealing of WEK111. (Senn and Agnew, 2008, p.157)

This texture randomization phenomenon has been coined "rare earth texture" by Stanford and Barnett (2008, p.403). The differences in the textures between the magnesium alloys with and without rare earth additions is attributed to the recrystallization behaviour. Figure 1.9 depicts the warm rolling behaviour of a magnesium alloy without rare earth elements (ZM21, a and b), and a magnesium alloy containing rare earth elements (ZEK100, c and d) at two different rolling temperatures (Hantzsche *et al.*, 2009, p.40). The (0002)

calculated pole represents the basal plane, and the (10-10) calculated pole represents the prismatic plane (Hantzsche *et al.*, 2009). Typical texture evolution is seen in the ZM21 alloy, with the greatest intensity occurring in the normal plane direction in the basal pole (Hantzsche *et al.*, 2009). The increased temperature of rolling (Figure 1.9 b) compared to the lower temperature (Figure 1.9 a) slightly decreases the intensity in the basal plane, however the orientations are not changed. Significant changes are observed in the rare earth containing magnesium alloy, ZEK100. In comparison to ZM21, there is a greater spread towards the transverse direction, and a broader spread towards the rolling direction (Hantzsche *et al.*, 2009). At increased rolling temperature (Figure 1.9 d), there is a dramatic difference in both orientation and intensity in both the basal and prismatic plane. The spread in the basal plane is now parallel to the transverse direction, with decreased maximum intensity, whereas the texture in the prismatic plane has been randomized (Hantzsche *et al.*, 2009).
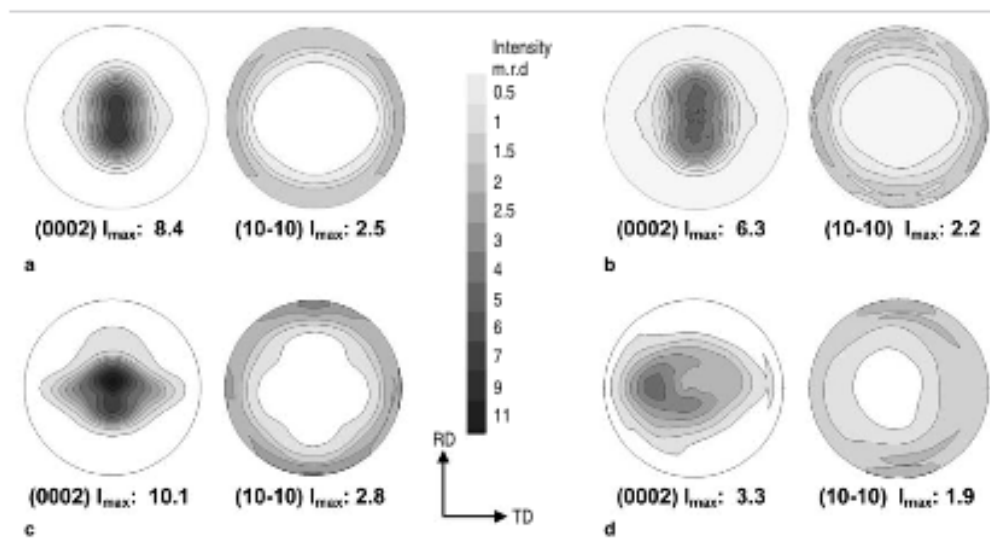
(a) ZM21 sheet rolled at 300°C, (b) ZM21 sheet rolled at 450°C, (c) ZEK100 sheet rolled at 300°C, (d) ZEK100 sheet rolled at 450°C.

Figure 1.9: Recalculated pole figures of the basal (0002) and prismatic (10-10) planes of the rolled and heat treated sheets. Maximum intensities are given in [m.r.d.]. (Hantzsche *et al.*, 2009, p.40)

Comparing the calculated pole figures in Figure 1.9, with the subsequent microstructures in Figure 1.10(a), it can be seen that all the micrographs except for c are fully recrystallized. Thus the recrystallization behaviour in magnesium alloys with rare elements is temperature dependant, and fully recrystallized structures result in a random texture evolution, with significantly decreased intensity, with the basal planes aligned parallel to the transverse direction (Hantzsche *et al.*, 2009).

The exact cause of the recrystallization behaviour in magnesium alloys in rare earth alloys has yet to be determined, however, many have hypothesized potential causes. Ball
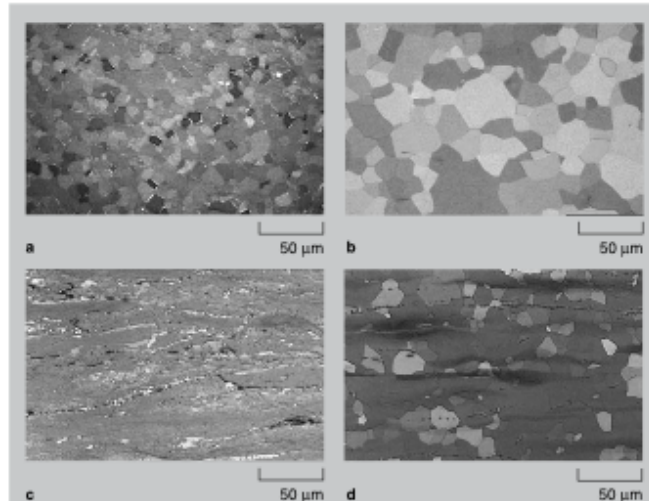
Figure 1.10: Micrographs representing the calculated pole figures for Figure 1.9 (Hantzsche *et al.*, 2009, p.40). Micrographs (a) and (b) are of ZM21 alloy, and micrographs (c) and (d) are of ZEK100 alloy.

and Prangnell (1994) attributed the texture randomization to Particle Simulated Nucleation (PSN), in which hard second phase particles rotate the plastically deforming matrix such that grain growth will be re-oriented during recrystallization. However, Stanford and Barnett (2008), investigated this hypothesis, and countered that magnesium alloys containing hard second phase particles, like AZ31, should exhibit similar texture weakening if PSN is operative, which they do not. Bohlen *et al.* (2007), hypothesize that the texture modification effect is closely related to the "solid solution alloy matrix"(p.2109). In addition, it has been observed that the texture of magnesium rare earth alloys continues to randomize with grain growth (Senn and Agnew, 2008). Senn and Agnew (2008, p.158), add in that "at this time it is speculated that the grain boundary mobilities are altered by the presence of the RE/Y elements (likely through solute drag) which prevents the texture

development observed in conventional Mg alloys." Bohlen *et al.* (2007), add the following to the recrystallization debate:

> Further study will be required to determine the exact connections between RE/Y additions and the texture-randomizing phenomenon. However, it is speculated that the reason RE elements strongly influence the recrystallization behaviour of magnesium alloys is the same reason they affect the creep behaviour, i.e. they are large atoms that diffuse slowly. Solute drag is known to influence strongly both the grain boundary mobility of different grain boundary orientations, specifically, and the recrystallization kinetics, in general. (Bohlen *et al.*, 2007, p.2109)

1.4   Deformation Behaviour.

Deformation of magnesium at room temperature occurs by crystallographic slip and twinning. The interactions between these two mechanisms dictate the mechanical properties of magnesium (Czerwinski, 2008). The three slip systems for magnesium, basal $\{0001\}\langle11\bar{2}0\rangle$, prismatic $\{10\bar{1}0\}\langle11\bar{2}0\rangle$, and pyramidal $\{10\bar{1}1\}\langle11\bar{2}0\rangle$, are displayed in Figure 1.11. Basal slip is the dominant slip mode in magnesium. Barnett (2007a) states, "magnesium's poor ductility is most commonly rationalized in terms of its possession of only one closed packed plane, the basal plane"[p.1]. The non-basal slip systems, prismatic and pyramidal slip, have critical resolved shear stress (CRSS) being 100-fold greater than that of basal slip, thus these slip mechanisms do not occur until much larger stresses are generated within misoriented grain boundary regions (Czerwinski, 2008, p.40).

(a) Basal Slip

(b) Prismatic Slip

(c) 1st Order Pyramidal Slip

(d) 2nd Order Pyramidal Slip
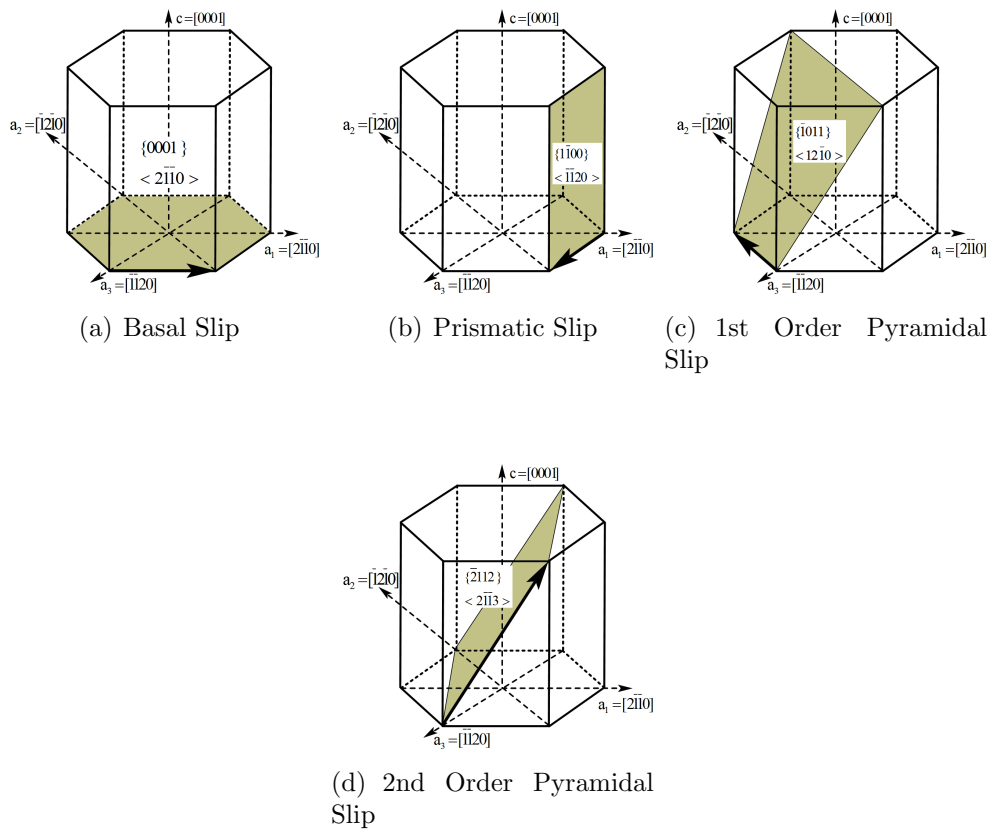
Figure 1.11: The slip systems in hexagonal close packed system of magnesium. Images provided by Dr. Niewczas

Twinning occurs in magnesium due to the inability to accomodate deformation outside of the basal plane. Any deformation that occurs perpendicular to the basal plane is likely to be accomodated by mechanical twinning. There are no crystal structure changes that occur during twinning, only a change in orientation of the crystal lattice (Czerwinski, 2008). Deformation twinning is driven by simple shear, and is accompanied by a shape change (Czerwinski, 2008). Twins are divided into two types: $\{10\bar{1}1\}$ type, and $\{10\bar{1}2\}$. The $\{10\bar{1}0\}$ are termed "Contraction twins", as they are responsible for accomodating strain when there is a contraction along the c-axis (Barnett, 2007b). The $\{10\bar{1}2\}$ are termed "Tension twins", as they are responsible for accomodating strain in which there is an extension along the c-axis(Barnett, 2007a). Compiled by Hiura (2010), the CRSS of the various slip and twinning modes in magnesium is presented with regards to temperature in Figure 1.13. It can be seen that at room temperature, the difference between the CRSS of $\{10\bar{1}1\}$ "Contraction" twins is much less favourable than the $\{10\bar{1}2\}$ "Tension" twins. However, this favourability is dependent on the texture of the material. For commercial magnesium sheet, the basal planes are parallel to the rolling direction. Any deformation perpendicular to the rolling direction (i.e parallel with the sheet plane) would be initially accomodated by $\{10\bar{1}1\}$ "Contraction" twinning, as the applied load would compress the c-axis.

(a) "Contraction" Twinning

(b) "Tension" Twinning
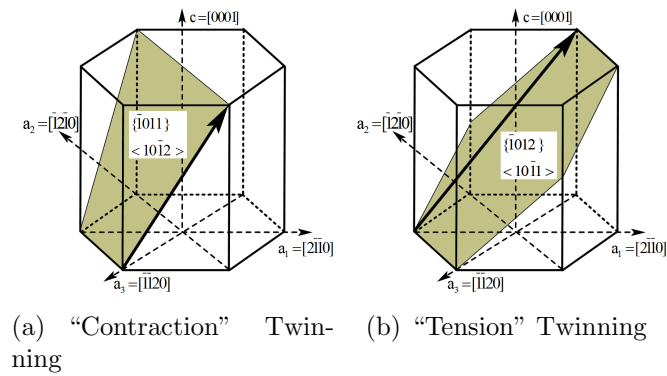
Figure 1.12: The twinning systems in hexagonal close packed system of magnesium. Images provided by Dr. Niewczas
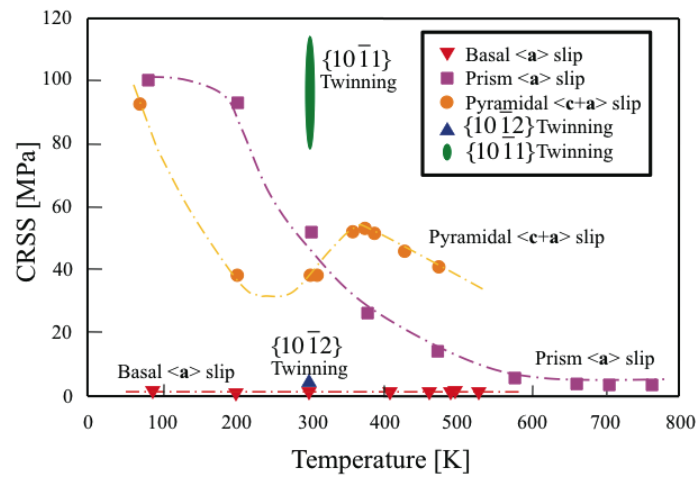
Figure 1.13: CRSS for Slip and Twinning Systems in Magnesium. Image provided by Fumiaki Hiura

1.4.1 Tensile Deformation of Magnesium-Rare Earth Alloys.

Stanford *et al.* (2008), summarize the differences in texture between RE containing magnesium alloys and non-RE containing magnesium alloys with regards to tensile deformation:

> The principle deformation mechanism in magnesium is basal slip. The extrusion texture developed in magnesium alloys is such that the basal poles are aligned perpendicular to the extrusion direction. This texture results in a majority of the grains being poorly aligned for basal slip during tensile deformation in the extrusion direction. However, in the case of those alloys with RE addition, the strength of the texture is weaker. The broader spread in orientation results in there being more grains better aligned for basal slip in that case. (Stanford *et al.*, 2008, 773)

Bohlen *et al.* (2007) modeled the tensile deformation behaviour of a rare earth containing magnesium alloy, ZW41, using the polycrystal plasticity approach. The free parameters in the model are "the critical resolved shear stresses (CRSSs) and the hardening behaviour of the individual slip and twinning mechanisms (Bohlen *et al.*, 2007, p.2109)." The results of the model are shown in Figure 1.14, with the graph on the left depicting the tensile behaviour applied in the rolling and transverse direction, and the graph on the right displaying the relative activity of the deformation mechanisms in rare earth containing ZW41 magnesium alloy (Bohlen *et al.*, 2007). Comparing the texture to the deformation process, it can be concluded that the linear hardening seen in the left graph for the transverse direction, is achieved primarily through a combination of basal slip and tensile twinning (Bohlen *et al.*, 2007). Bohlen *et al.* (2007, p.2110), claim the observed linear hardening is intermediate to the parabolic hardening of slip-dominated deformation and the sigmodial hardening observed for twin dominated deformation. Prismatic and pyramidal $< c + a >$

slip increase in activity later in the deformation process, as shown in the right graph of Figure 1.14, prompting the hardening to become parabolic in nature. The reason for this change in deformation mode is the crystallographic re-orientation that occurs during tensile twinning generally places grains in a more difficult orientation with respect to continued slip or twinning (Bohlen *et al.*, 2007, p.2110).

(a)   (b)
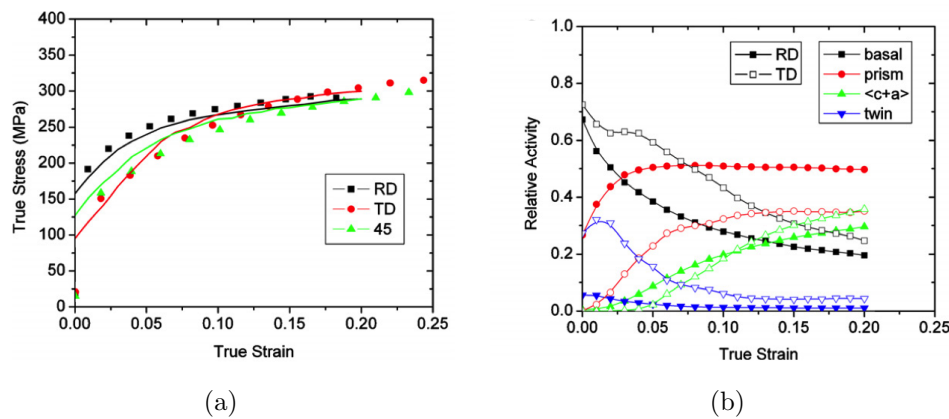
Figure 1.14: Comparison of experimental and simulated (a) flow curves and (b) the simulated activities of the deformation mechanisms during rolling and transverse direction tensile tests for magnesium alloy ZW41(Bohlen *et al.*, 2007, p.2110).

The tensile deformation along the rolling direction shows slight linear hardening at the beginning of deformation, and then becomes parabolic in nature with the prismatic and pyramidal slip dominating the deformation activity (Bohlen *et al.*, 2007). With the basal planes perpendicular to the rolling direction, minimal basal slip is achieved, and thus it is more difficult to deform, resulting in a higher flow stress than the tensile deformation in the transverse direction.

Knowing the texture orientations, as well as the resulting deformation sequence, comparison between the tensile deformation of pure magnesium and a nominal magnesium

gadolinium alloy can be made, as shown in Figure 1.15 (Stanford and Barnett, 2008). With the basal planes laying perpendicular to the extrusion axis, it is expected that parabolic hardening should be caused by slip-dominated deformation, specifically prismatic and pyramidal slip. The linear hardening behaviour seen in the rare earth alloy is expected due to the randomized texture, and a more favourable crystallographic orientation to accommodate basal slip. The linear hardening seen in the Mg-Gd alloy improves the resistance to plastic instability (Bohlen *et al.*, 2007) and leads to an almost two fold improvement in ductility (Stanford and Barnett, 2008). It is important to note that the mechanical testing performed by Stanford and Barnett (2008) was on extruded material with a grain size of 17 μm, and a strain rate of 1.4×10^{-3}. The strain rate is an order of magnitude greater than the strain rate performed in the experimental work of this thesis. Additionally the grain size is almost an order magnitude smaller than the grain sizes of the materials used in the experimental work of this thesis.
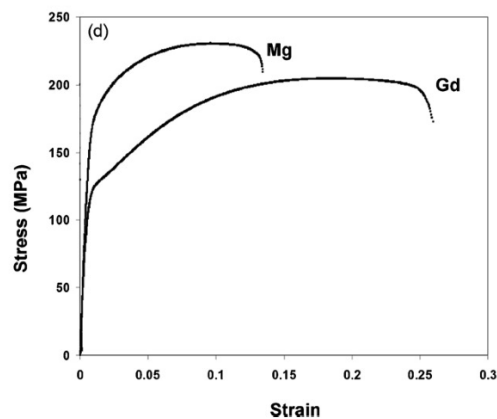
Figure 1.15: Stress-strain curves for alloys Mg and Mg-0.24 at% Gd with grain sizes of 17 μm. (Stanford and Barnett, 2008, p.402)

1.4.2 Anisotropy of the Yield Stress in Rare Earth Containing Magnesium Alloys.

Safi-Naqvi *et al.* (2008) investigated the mechanical anisotropy of magnesium alloys containing rare earth additions to create yield loci using an approach that would allow for a "good approximation to the plane stress locus for sheet material that can be obtained from a small number of well chosen tests involving tension, compression, and plane strain deformation"(Safi-Naqvi *et al.*, 2008, p. 1284). The yield loci are presented in Figure 1.16.(Safi-Naqvi *et al.*, 2008, p.1288)

Results from the yield loci produced by Safi-Naqvi *et al.* (2008) display mechanical behaviour indicative of the developed crystallographic texture discussed in earlier sections of this report. The magnesium alloy without rare earth additions (ZM61) has greater strength in the extrusion direction due to the basal poles being poorly aligned for slip, and thus the flow stresses generated are higher than in the transverse direction, where the basal poles are more favourably aligned for slip. Conversely, the Mg-3Y alloy shows near isotropic behaviour (Safi-Naqvi *et al.*, 2008). The authors concluded that the "directionality of strength in the plane of the Mg-3Y cannot be rationalized on either slip or twinning according to any simple model."(Safi-Naqvi *et al.*, 2008, p.1291) It is assumed that the simple model the authors are refering to is the viscoplastic self-consistent (VPSC) model, that has been developed for face-centered cubic (FCC) materials. The application of this model to the hexagonal close-packed (HCP) lattice is currently ongoing with many international researchers. It was also added "the incidence of twinning is greatly reduced by yttrium but an adequate explanation of the anisotropic behaviour is still lacking."(Safi-Naqvi *et al.*, 2008, p.1292)
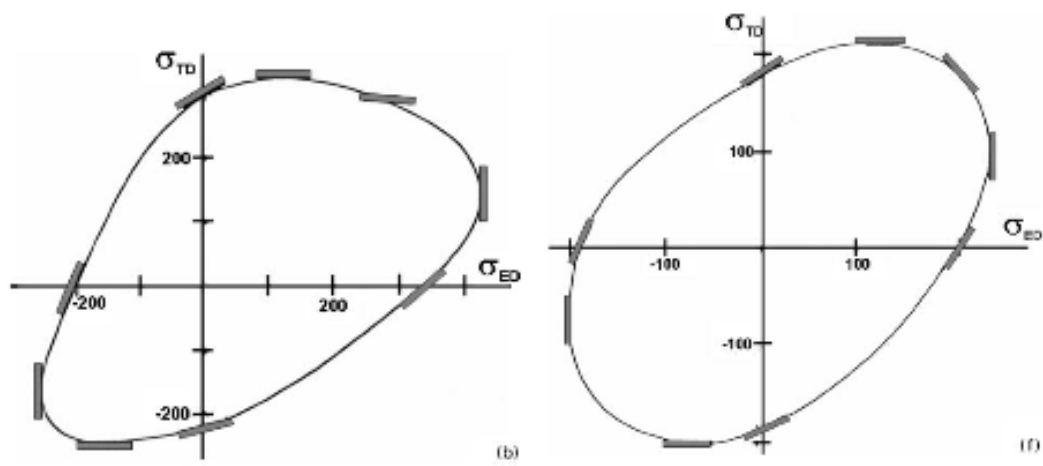
Figure 1.16: Yield Loci for alloys (b) ZM61, and (f) Mg-3Y. All alloys are in the aged condition. (Safi-Naqvi *et al.*, 2008, p.1288)

1.5   Previous Work

Gadolinium additions to magnesium have been studied extensively by researchers, specifically regarding its effects on texture modification. Some research has been performed on the mechanical properties of binary Mg-Gd alloys, which will be explored in the following sections.

1.5.1   Solid Solution Strengthening

Stanford *et al.* (2010b) examined the mechanical properties of the Mg-Gd binary alloy class, and compared it to results for pure magnesium and Mg-Al systems. The research focused on examining the relationship between solute strengthening, elongation, and texture. In regards to the solid solution strengthening of gadolinium in magnesium, they found marginal increases in the yield point in tension of normalized alloys with increasing solute, after a strong increase at low concentrations (Stanford *et al.*, 2010b). The results are displayed in Figure 1.17.

Additionally, Gao *et al.* (2009) examined the solid solution strenghtening effect of binary Mg-Gd and Mg-Y alloys, as depicted in Figure 1.18. These results appear to conflict with those of Stanford *et al.* (2010b), in which Gao *et al.* (2009) observed strong solid solution strenghtening increases with increasing solute content. However the condition of the samples were as-cast. The point of interest was the comparison of the solid solution strenghtening parameter, k_{ss}, against other common alloying additions. Comparing Gd to Al and Zn, it was found that Gd offers far greater solid solution strengthening compared to the Mg-Al and Mg-Zn. This observation, goes against the classical solid solution model, in which the "atomic size and shear modulus misfits are considered as parameters controlling SSS (Gao *et al.*, 2009, p.383)." This difference from the classical solid solution model left
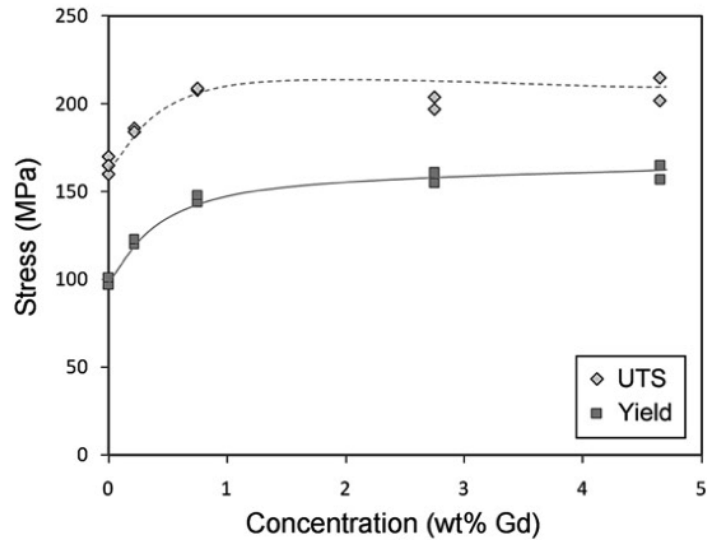
Figure 1.17: Solid Solution Strengthening of Mg-Gd Alloys. (Stanford *et al.*, 2010b, p.6779)

Gao *et al.* (2009) to conclude that there is a possible valency effect that could be partially responsible for the enhanced solid solution strengthening.

Stanford *et al.* (2010b) continued to investigate further into the differences in the solid solution strengthening of Mg-Gd relative to other elements, and noted from neutron diffraction studies by Clausen *et al.* (2008) and Muránsky *et al.* (2010) on extruded magnesium bars, that the yield point can be related to the CRSS for prismatic slip (Stanford *et al.*, 2010b, p.6781). Since all the different alloying additions produce different textures, and texture intensities, Stanford *et al.* (2010b) correlated the increase in texture strength to that of pure magnesium to present the yield strength normalized to texture. These results are displayed in Figure 1.19, which displays the strengthening of the prismatic slip system. It is apparent that gadolinium provides significant hardening of the prismatic slip system with low levels of solute, above which, there is marginal impact on yield strength. Stanford *et al.* (2010b) concluded the non-rare earth additions (Al, Li, Zn) decrease the CRSS of
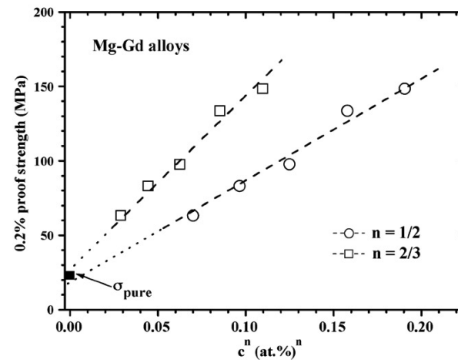
Figure 1.18: Solid Solution Strengthing of Mg-Gd Alloys (Gao *et al.*, 2009, p.382)

prismatic slip, whereas rare-earth additions (Gd, Th) provide an increase in the CRSS of prismatic slip (Stanford *et al.*, 2010b, p.6781).
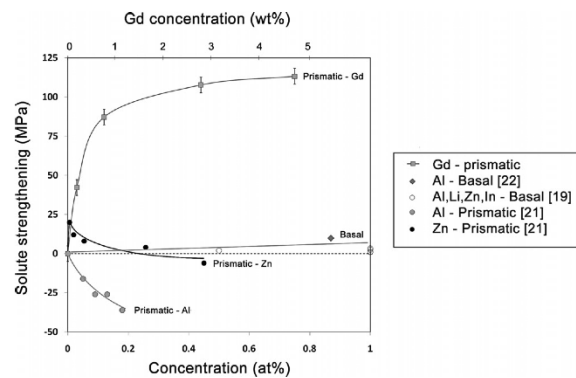
Figure 1.19: Comparision of Solid Solution Strengthening with Other Alloying Additions. (Stanford *et al.*, 2010b, p.6781)

1.5.2   Strain Rate Sensitivity

Chun and Davies (2011) reported that for magnesium, the effect of deformation on strain rate sensitivity (SRS) seems straightforward: increasing temperature increases the SRS of the material, which than leads to improved ductility (Chun and Davies, 2011). This improved ductility is the result of increased post-uniform deformation (Chun and Davies, 2011). Chun and Davies (2011) also noted that the SRS of materials is affected by other factors such as texture and applied strain. However, given that Chun and Davies (2011) evaluated AZ31, which has vastly different mechanical and texture properties than Mg-RE alloys, it would be expected that completely different SRS results would be observed. Looking specifically at rare earth additions, and factoring in testing at room temperature, as shown in Figure 1.20 it would be expected that texture and applied strain would be the most prominent factors. Stanford *et al.* (2010a) evaluated the differences between Mg-1.4 wt% Gd and Mg-1.4 wt% Al, at elevated temperatures, and noted that "it appears that for magnesium alloys, information currently available suggests that the addition of RE elements can reduce the SRS, but that does not necessarily have a detrimental impact on elongation" (Stanford *et al.*, 2010a, p.742). Figures 1.21(a)-1.21(b) depict Stanford *et al.* (2010a) results, and it can be seen that although SRS is decreasing in the 150-250°C range, the elongation is increasing, which goes against the conventional notion that decreasing SRS should result in decreasing elongation. The AZ31 SRS research conducted by Chun and Davies (2011) concluded that the decreasing SRS corresponded to unfavourable conditions for tension twinning, whereas increasing SRS corresponded to favourable conditions for tension twinning. Additionally, they suggested that there are links between contraction twinning activity and decreasing SRS. It appears that explanation of SRS in Mg-RE alloys, and its connection to elongation, lies within deeper investigation of deformation behaviour.

Stanford *et al.* (2010a) summarized this link best:

> The lack of influence of SRS on elongation in magnesium alloys is well ex-
> plained by microstructural development during the tensile test. At low temper-
> atures, all the specimens deform primarily by slip, but deformation twinning
> also takes place. Regions where multiple twinning events have taken place are
> known to form voids during subsequent deformation. These double twinned
> regions are often accused of leading to early failure of extruded material after
> room-temperature deformation, and this could be one of the reasons that SRS
> does not influence ductility in these (Mg-RE) alloys. (2010a, p.742)
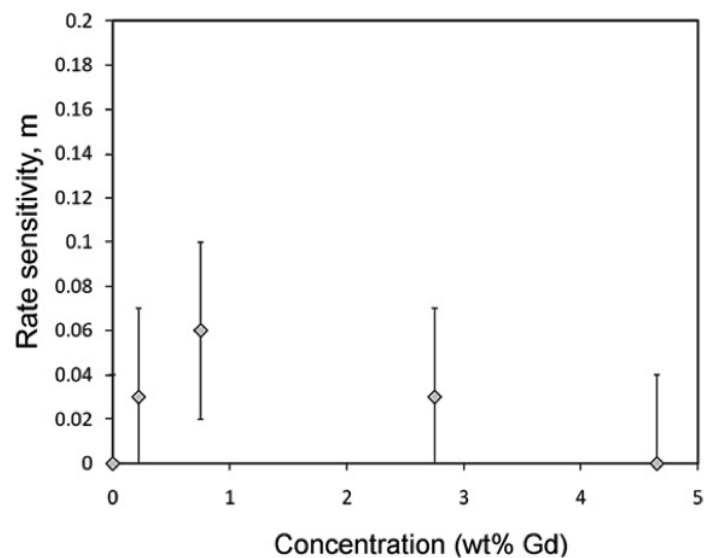
Figure 1.20: Strain Rate Sensitivity of Mg-Gd Alloys. (Stanford *et al.*, 2010b, p.6779)
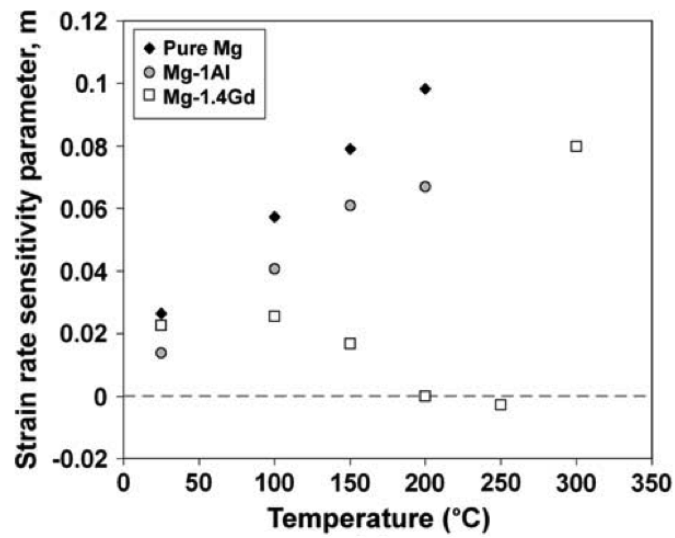
(a) SRS vs Temperature
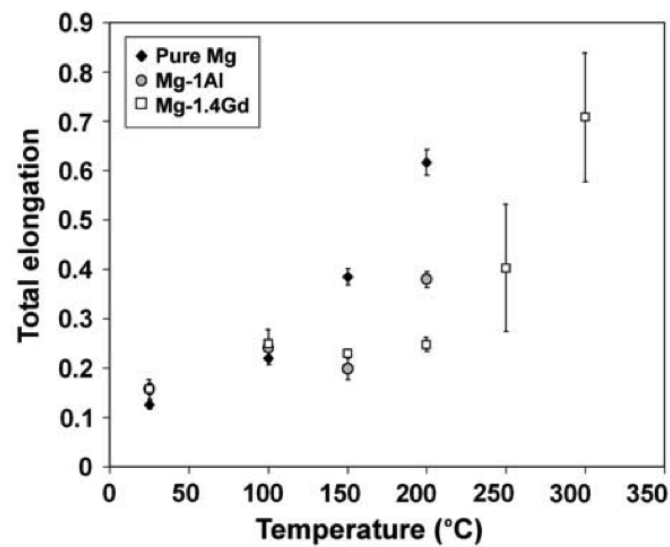
(b) Elongation vs Temperature

Figure 1.21: Strain Rate Sensitivity Results for Mg, Mg-1.4Al, and Mg-1.4 Gd with Increasing Temperature (Stanford *et al.*, 2010a, p.738)

Chapter 2

Experimental Procedure

2.1 Alloy development and thermo-mechanical processing.

Binary Mg-Gd, Mg-Sc and Mg-Sm alloys were produced in laboratory by mixing appropriate amount of pure Rare Earth elements (Gd, Sc, Sm) purchased from Alfa Aesar Company with 99.99% purity Mg. High purity magnesium, as well as alloying elements were added to the graphite crucible with a stainless steel mould covered with boron nitride placed beneath. The chamber was evacuated with a vacuum pump and then flowing argon gas was used during heating. Using the induction furnace, the melt was heated to approximately 750°C and held for 5 minutes at this temperature. The melt was then cast and allowed to cool under argon atmosphere until the temperature had reached a safe handling temperature. The cast ingots of approximate dimension 30mm x 70mm x 150mm were homogenized at 550°C for 72 hours for the Mg-Gd alloys. In the case of the Mg-Sm and Mg-Sc, the alloys were homogenized at 550°C for 8 hours, to reduce oxidation of alloys.

Homogenized ingots were annealed at 400°C for 30 minutes in air, then subjected to a 20% reduction by rolling, and then annealed again 400°C for 30 minutes. This process was repeated until the desired thickness of 5 mm was achieved. The sample was then sectioned to save material to create compression samples, and then further processed to a final thickness of 3 mm. The rolling procedure was also completed using high purity Mg for comparison. At the completion of the rolling process, compostional analysis was performed by Doug Culley at the two ends of the rolled sheet using inductively coupled plasma mass spectrometry (ICP-MS). The composition of all Mg-RE alloys which have been developed is presented in Tables 2.1, 2.2 and 2.3.

Table 2.1: Composition of Mg-Gd Alloys

Mg-Gd wt%	at%	Grain size (μm)
1.40	0.22	90
1.80	0.28	87
2.90	0.46	43
4.60	0.74	28

Atomic Mass: Gd 157.25

Mg 24.30

Table 2.2: Composition of Mg-Sc Alloys

Mg-Sc wt%	at%	Grain size (μm)
0.036	0.019	33
0.087	0.05	81
0.18	0.10	68
0.29	0.16	90
0.68	0.31	120

Atomic Mass: Sc 44.96

Mg 24.3

Table 2.3: Composition of Mg-Sm Alloys

Mg-Sm wt%	at%	Grain size (μm)
1.76	0.29	75
2.18	0.36	87
2.38	0.38	59
4.60	0.77	65

Atomic Mass: Sm 150.36

Mg 24.30

2.2   Deformation procedure.

Tensile test samples with gauge dimensions 2 x 3 x 35 mm, with heads for griping purpose, and the compression test samples with the diameter 5 mm and height 10 mm were machined from the cold rolled sheets. Before deformation, the samples were annealed to produce recrystallized material. The samples were annealed in a protective argon atmosphere, at 400°C for 25 minutes, followed by air cooling. The average grain size of annealed samples are reported in Tables 2.1- 2.3, and were calculated using the ASTM Linear Intercept method. The specimens were deformed at room temperature, at a constant cross-head velocity corresponding to an initial strain rate of $2.8 \times 10^{-4} \ s^{-1}$ under tension and compression using the hydraulic MTS 858 system with TestStar IIm controller. The sample orientation is displayed in Figure 2.22. The flow curves, and work hardening behavior were then calculated from the test data.
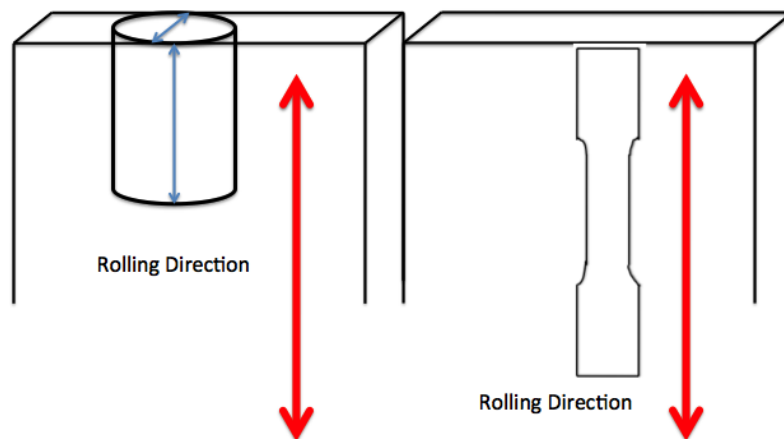
Figure 2.22: Tension and Compression Sample Orientation

2.3   Strain Rate Sensitivity.

The strain rate sensitivity jumps were carried out by repeating the instantaneous rate change between 2.8×10^{-4} s^{-1} and 2.8×10^{-5} s^{-1} during deformation. This instantaneous rate change was carried out under both tension and compression. From this data the instantaneous stress drop associated with strain rate change was evaluated by Basinski's method. The evolution of stress drops and stress jumps during strain rate change as a function of true strain together with the Haasen plots.

2.4   Texture.

The recrystallization texture of all the selected compositions, as well as the deformation texture of the compressive samples were evaluated using a Bruker diffractometer, collected at an 8 cm distance using an area detector. The texture was obtained by scanning the top face of the cylindrical samples, in which the normal to the top face is parallel to the rolling direction. Raw diffraction data was then used to create pole figures using the GADDS software package. Pole figures for $\{10\bar{1}0\}$, $\{0002\}$, $\{10\bar{1}1\}$, $\{10\bar{1}2\}$ and $\{11\bar{2}0\}$ were evaluated. These pole figures then were inputted into the popLA software package to perform corrections and normalize the pole figure, and then finally the Orientation Distrbution Function (ODF) was calculated with the MTex 3.1 software package used with MATLAB. With the generated ODF, recalculated pole figures were created and then plotted using the MTex software.

Chapter 3

Results

3.1 Mechanical Tensile Testing

3.1.1 Flow Stress

The True Stress-True Strain results of tensile testing for each alloy class is depicted in the following figures (Mg-Gd in Figure 3.23, Mg-Sm in Figure 3.24, Mg-Sc in Figure 3.25). In Figure 3.23, with increasing solute content, there is an increase in both yield strength, and flow stress. Additionally, there is an increase in the true strain to failure with increasing solute content. Finally, with increasing solute content, there is an increase in the maximum true stress, which is also depicted in Figure 3.27.

In Figure 3.24, with increasing solute content, there is an increase in both yield strength, and flow stress. Additionally, there is an increase in the true strain to failure with increasing solute content up to 0.38 at%, at which point there is a decrease in true strain to failure. There is a peculiar behaviour with Mg-0.29at%Sm, as it mimics the tensile behaviour of pure magnesium. This would suggest that the solute content up to this level does not
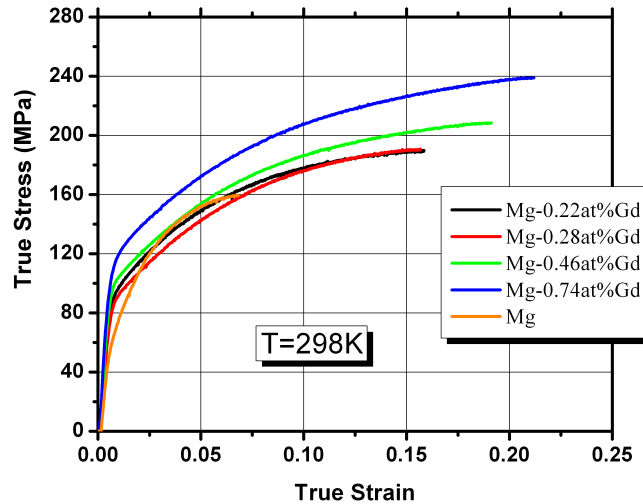
Figure 3.23: Tensile Flow Stress Results for Mg-Gd

impact the mechanical properties of pure magnesium from a true stress- true strain point of view.

In Figure 3.25, with increasing solute content, there is an increase in yield strength. However there is peculiar behavior in regards to flow stress with increasing solute content. As seen, the Mg-Sm alloys with low levels of solute content (0.019 at% and 0.05 at%) have lower yield strength than magnesium, and similar maximum true stress and true strain to failure. Additionally, up to 0.16 at% Sc, there is an increase in maximum true stress with increasing solute content. However for increases beyond 0.16 at%, the maximum true stress decreases. Lastly, it is interesting to note the shape of the true stress - true strain graph with increasing solute content. At low levels of solute content, it appears the shape of the pure magnesium curve has been compressed vertically while retaining similar true strain to failure. At 0.10 at% Sc, it appears the shape of the pure magnesium curve
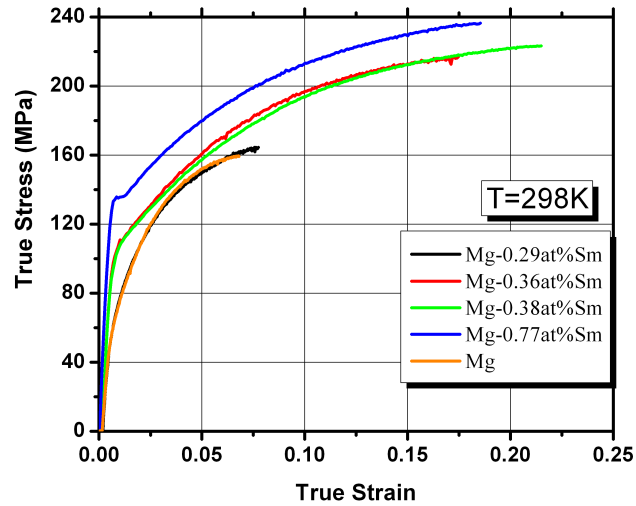
Figure 3.24: Tensile Flow Stress Results for Mg-Sm

has been stretched vertically, while again retaining the similar true strain to failure. At solute content levels above 0.10 at% Sc, the curves of these alloys appear to be stretched diagonally in comparison to pure magnesium, obtaining an increase in both maximum true stress, and true strain to failure.
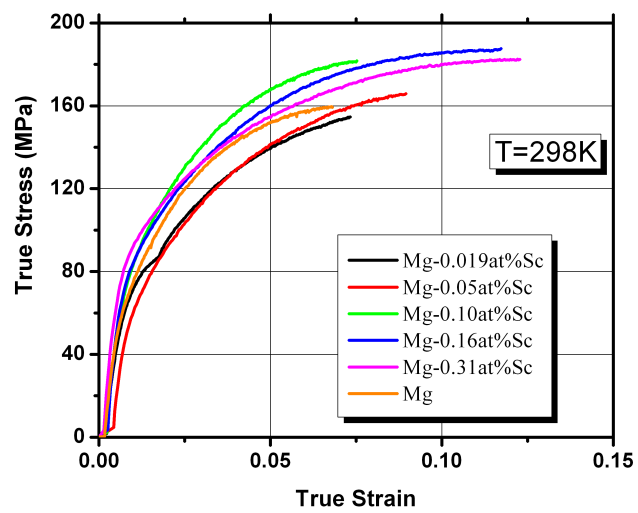
Figure 3.25: Tensile Flow Stress Results for Mg-Sc

Comparing the yield strengths of all the alloys relative to their solute content, as shown in Figure 3.26, at the highest solute content, samarium addition provides the greatest yield strength compared to the other alloying additions. At lower solute contents (approximately 0.3 at%), gadolinium addition provides the greatest yield strength compared to the other alloying additions. With the exception of the 0.36 at% Sm, gadolinium offers the greatest yield strengthening in comparison to the other alloying additions up to approximately 0.5 at%.

Comparing the maximum tensile true stress of all the alloys relative to their solute content,
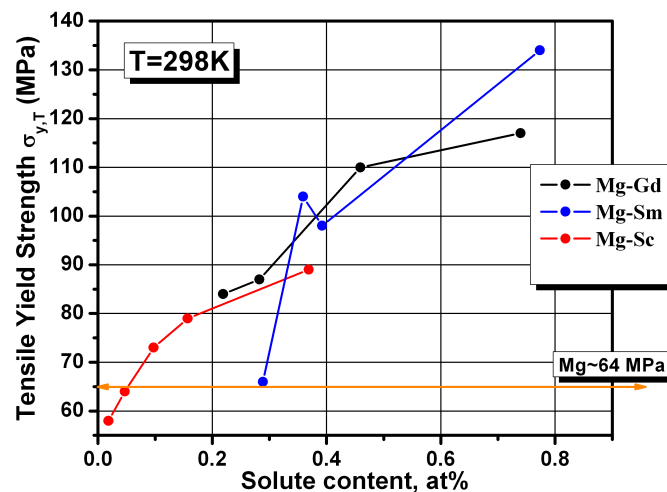
Figure 3.26: Tensile Yield Strength vs Concentration for Alloys Tested

as shown in Figure 3.27, at the highest solute content, gadolinium addition provides the greatest maximum tensile true stress compared to the other alloying additions. Looking at trends within the alloying additions, gadolinium has a continual increase in maximum true stress with increasing solute content, that appears constant. Samarium retains a continual increase in the maximum true stress with increasing solute content. The rate

at which this increase proceeds reduces at higher solute content relative to lower solute content. Alloying with scandium from low solute levels to approximately 0.175 at% results in increasing maximum true stress, beyond this point further alloying results in diminishing returns. Comparing the true strain to failure of all the alloys relative to their solute content,
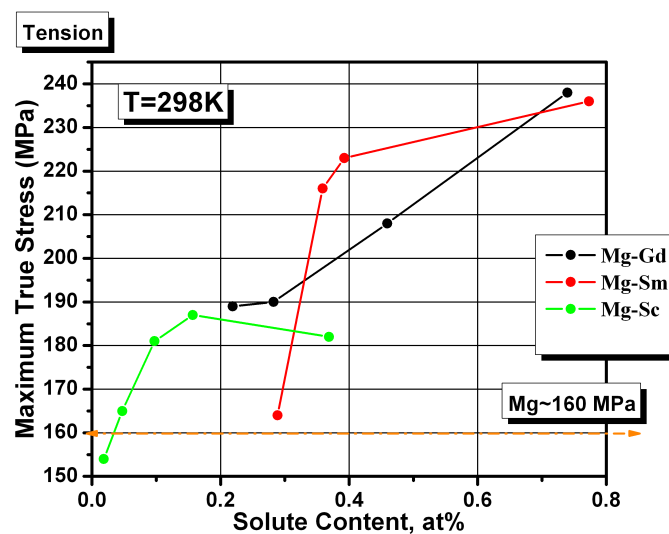
Figure 3.27: Maximum Tensile True Stress vs Concentration for Alloys Tested

as shown in Figure 4.68, at the highest solute content, gadolinium addition provide the greatest strain to failure. Looking at trends within the alloying additions, the true strain to failure initially decreases, and then rises continually with increasing solute. Samarium exhibits a steep rise in the true strain to failure up to a maximum at approximately 0.4 at%, and then decreases. Except for the varying nature at the very low solute levels in scandium, increasing solute increases the true strain to failure for Mg-Sc.
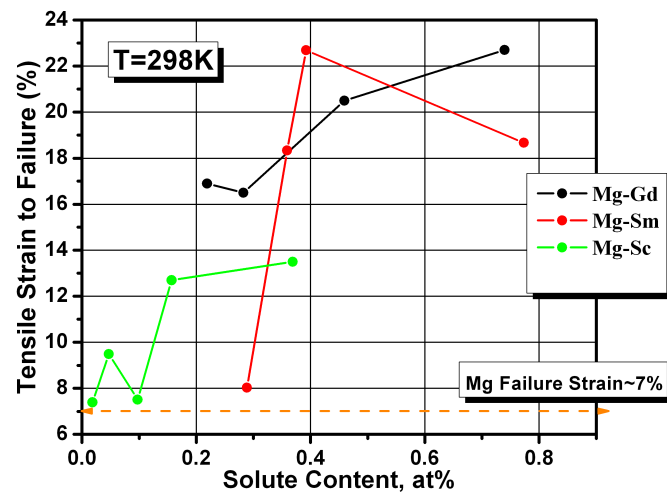
Figure 3.28: True Strain at Tensile Fracture vs Concentration for all Alloys

3.1.2   Work Hardening Behaviour in Tension

The Work Hardening results of tensile testing plotted against True Strain, and Effective Stress for each alloy class are depicted in the following figures: Mg-Gd in Figure 3.29, Mg-Sm in Figure 3.30 and Mg-Sc in Figure 3.31. All alloys show Stage III of continuous decrease of work-hardening rate from the beginning of deformation up to the fracture. In Figure 3.29(a), with increasing solute content, the extent of the work hardening extends to larger true strains. When plotted against effective stress (Figure 3.29(b)), we can see that all alloys exhibit a much more gradular exhaustion of work hardening capacity compared to pure magnesium. Work hardening capacity increases with increasing solute content, with the 0.74 at% Gd alloy exhibiting the greatest work hardening capacity.
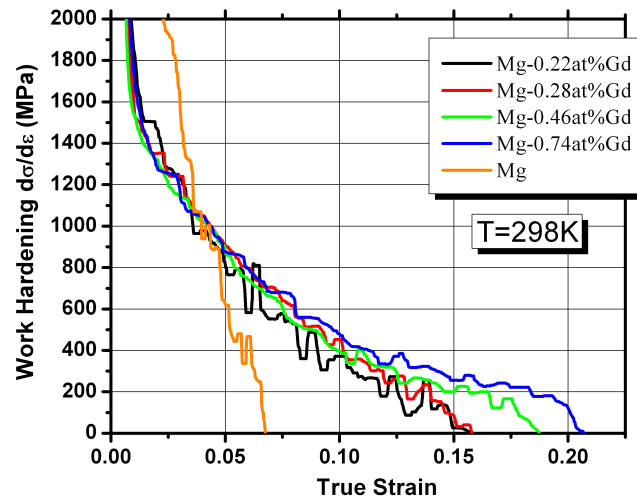
(a) Work Hardening vs Strain in Tension Mg-Gd
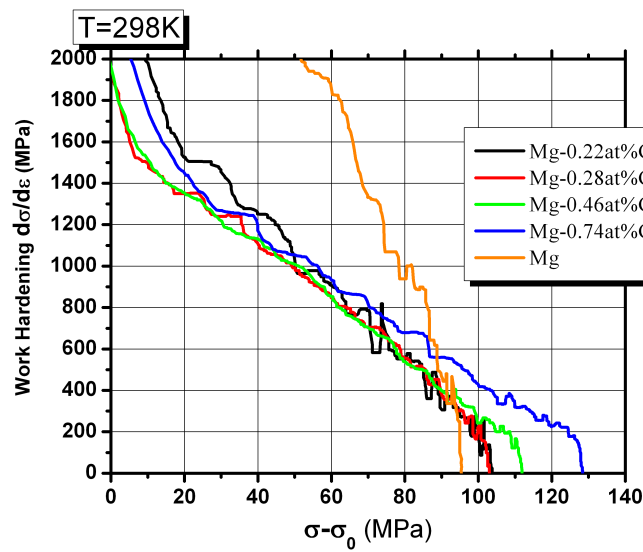
(b) Work Hardening vs Stress in Tension Mg-Gd

Figure 3.29: Tensile Work Hardening Results for Mg-Gd

Table 3.4: Initial Hardening Rate Θ_0 for Mg-Gd Alloys in Tension

Composition (at%)	Θ_0 (GPa)
Mg	4.3
0.22	1.8
0.28	1.6
0.46	1.6
0.74	1.65

If we extrapolate the hardening curve back to the y-axis, since we have a decreasing hardening rate associated typically with Stage III of work hardening, we can obtain the initial hardening term, Θ_0, and compare its behaviour for the increasing solute. These results are presented in Table 3.4. With increasing solute, Θ_0 decreases and remains relatively unchanged for larger solute content.

All Mg-Sm alloys show, from the beginning of deformation Stage III, a continuous decrease of work-hardening rate up to fracture, as shown in Figure 3.30(a). However, samarium, compared to gadolinium, shows quantitatively different work hardening behavior. In Figure 3.30(a), the lowest solute content alloy, 0.29 at% Sm has similar work hardening behaviour to that of pure magnesium. With increasing solute content above 0.29 at% Sm, a more gradual exhaustion of work hardening capacity is observed. In Figure 3.30(b), plotted against effective stress, we can see that the alloy with the highest solute content (0.77 at% Sm), has the lowest work hardening capacity. The 0.38 at% Sm alloy has the greatest work hardening capacity in comparison to all the other alloys. It is seen also that the rate of work hardening decrease with strain or stress is similar for pure Mg and Mg-0.29 at% Sm alloy and similar for Mg-0.36 at% Sm, Mg-0.38 at% Sm and Mg-0.77 at% Sm alloys.

(a) Work Hardening vs Strain in Tension Mg-Sm
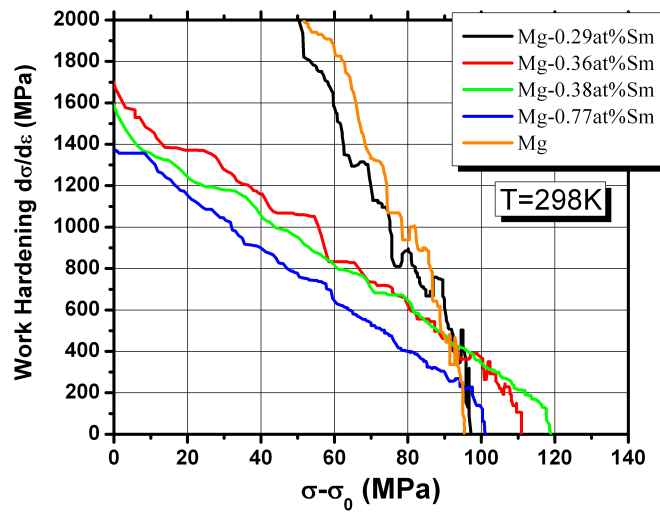
(b) Work Hardening vs Stress in Tension Mg-Sm

Figure 3.30: Tensile Work Hardening Results for Mg-Sm

The results of the initial hardening rate, Θ_0, for Mg-Sm alloys are presented in Table 3.5. With increasing solute, Θ_0 decreases, and remains relatively unchanged for higher solute content Mg-Sm alloys. Mg-0.29 at% Sm has a similar initial hardening term to magnesium, where all other compositions are three times lower than that of magnesium.

Table 3.5: Initial Hardening Rate Θ_0 for Mg-Sm Alloys in Tension

Composition (at%)	Θ_0 (GPa)
Mg	4.3
0.29	3.8
0.36	1.37
0.38	1.5
0.77	1.35

Figure 3.31 shows work-hardening behaviour of Mg-Sc alloys. Similar to previously discussed Mg-Gd and Mg-Sm alloys, all Mg-Sc alloys exhibit Stage III of continuous work hardening decrease from the beginning of plastic flow. In Figure 3.31(a), with increasing solute content, the extent of the work hardening decrease is shifted to larger true strains. Additionally, with increasing solute content, the slope of the hardening decrease (exhaustion of work hardening) is decreased. When plotted against effective stress (Figure 3.31(b)), we can see that all alloys with the exception of 0.10 at% Sc, have a lower work hardening capacity then pure magnesium. Examining the trend within the alloys, it would suggest that initially, alloying decreases the work hardening capacity (as shown in the drop with 0.019 at% Sc and 0.05 at% Sc), then further alloying increases the capacity above that of pure magnesium, at which point further alloying provides diminishing returns in regards to work hardening capacity.

(a) Work Hardening vs Strain in Tension Mg-Sc
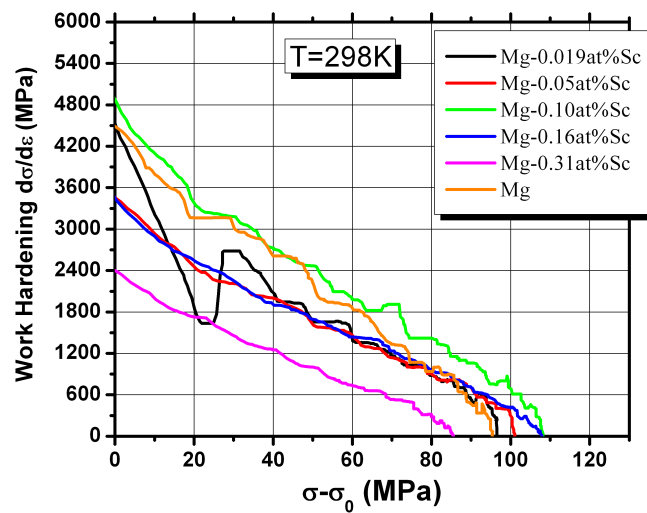
(b) Work Hardening vs Stress in Tension Mg-Sc

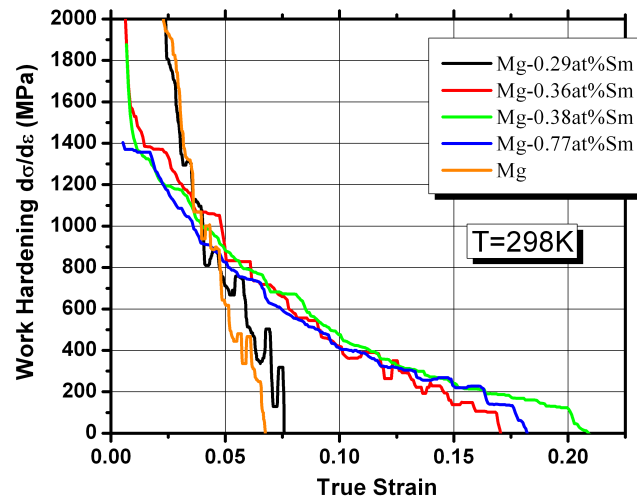Figure 3.31: Tensile Work Hardening Results for Mg-Sc

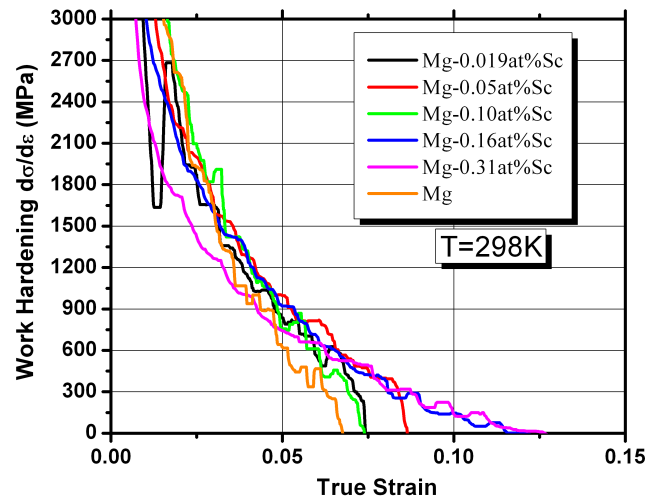The results of the initial hardening rate, Θ_0, for Mg-Sc alloys are presented in Table 3.6. The lowest initial hardening is seen at the highest concentration alloy (0.31 at% Sc), and the highest initial hardening, equal to that of magnesium, is seen in the 0.10 at% Sc alloy. All other compositions retain the same initial Θ_0 level.

Table 3.6: Initial Hardening Rate Θ_0 for Mg-Sc Alloys in Tension

Composition (at%)	Θ_0 (GPa)
Mg	4.3
0.019	3.5
0.05	3.5
0.10	4.3
0.16	3.5
0.31	2.4

3.2   Mechanical Compression Testing

3.2.1   Flow Stress

The True Stress -True Strain results of compressive testing for each alloy class are depicted in the following figures: Mg-Gd in Figure 3.32, Mg-Sm in Figure 3.33, Mg-Sc in Figure 3.34. For Mg-Gd alloys shown in Figure 3.32, one observes with increasing solute content an increase in both yield stress and flow stress. Additionally, there is an increase in the true strain to failure with increasing solute content. Finally, all Mg-Gd alloys exhibit a higher maximum true stress and yield strength compared to pure magnesium.
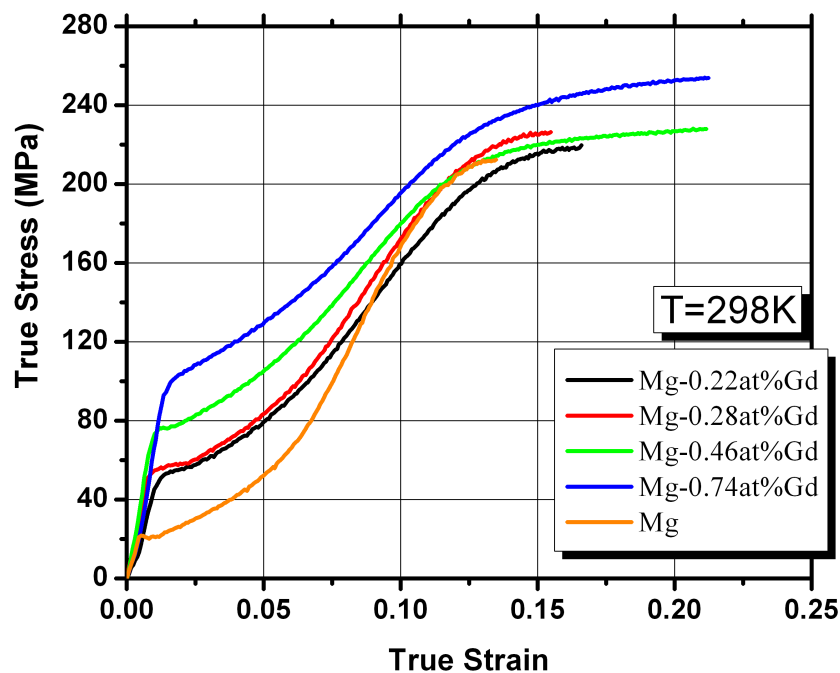
Figure 3.32: Compressive Flow Stress Results for Mg-Gd

Figure 3.33 shows strain-stress characteristics of Mg-Sm alloys in compression. In Figure 3.33, with increasing solute content one observes an increase in both yield strength and the flow stress. As seen in tension, there is a peculiar behaviour with Mg-0.29 at% Sm, as it mimics the compressive behaviour of pure magnesium. This would suggest that the solute content up to this level does not impact the mechanical properties of pure magnesium from a true stress- true strain point of view.
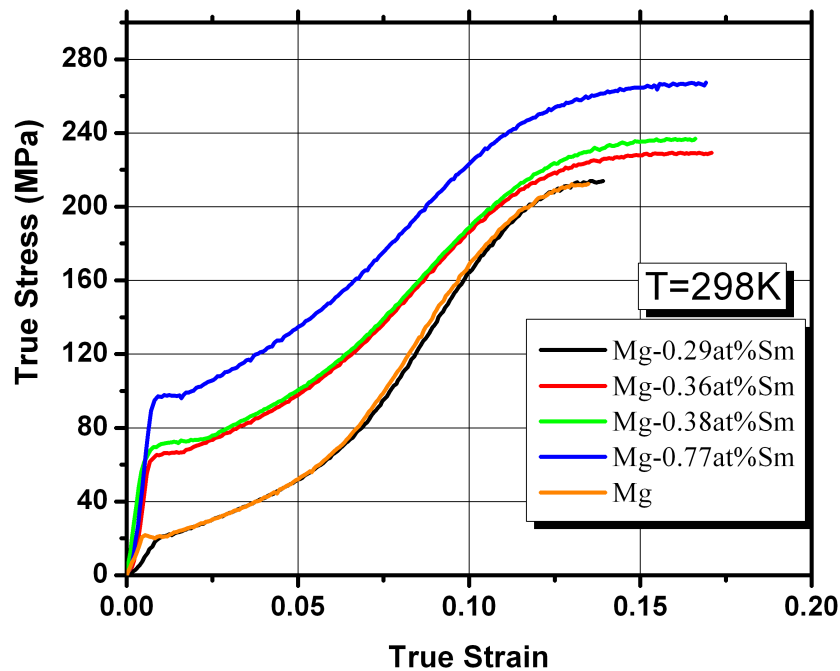
Figure 3.33: Compressive Flow Stress Results for Mg-Sm

Figure 3.34 shows strain-stress characteristics of Mg-Sc alloys deformed in compression. Qualitatively, Mg-Sc alloys show similar behaviour as observed previously. In Figure 3.34, with increasing solute content, there is an increase in both yield strength, and flow stress;

however the increases are fairly marginal. At the highest solute content (0.31 at% Sc), we have a two fold increase in yield strength relative to pure magnesium, far less than seen with gadolinium and samarium (as depicted in Figure 3.35). Additionally, with greater solute content, the maximum true stress increases, but it begins to plateau and barely exceeds the maximum true stress of pure magnesium. Overall, it would suggest that the addition of scandium results in an increase in yield strength relative to pure magnesium; however the maximum attainable true stress compared to pure magnesium is un-effected (or decreased in the case of the low solute level alloys, 0.019 at% Sc and 0.05 at% Sc).
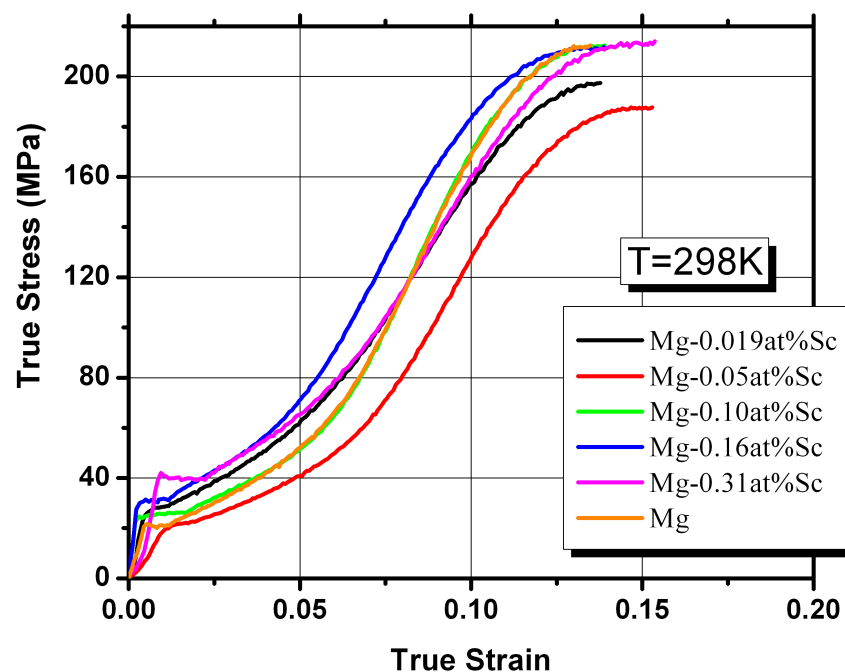
Figure 3.34: Compressive Flow Stress Results for Mg-Sc

Comparing the compressive yield strengths of all the alloys relative to their solute

content, as shown in Figure 3.35, one observes that at the highest solute content, Mg-Gd alloys show the greatest yield strength. This would suggest that gadolinium addition provide higher strengthening effect compared to the other alloying additions. Additionally, it appears that for all alloying levels, gadolinium offers the greatest compressive yield strength with respect to solute content.
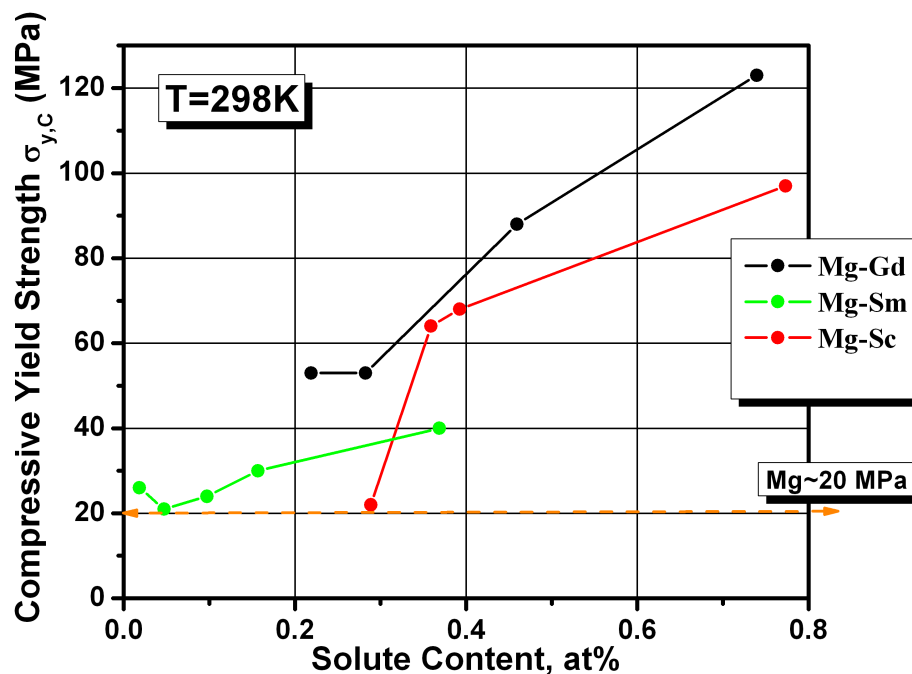
Figure 3.35: Compressive Yield Strength vs Concentration for Alloys Tested

Comparing the maximum compressive true stress of all the alloys relative to their solute content, as shown in Figure 3.36, at the highest solute content, samarium addition provide the greatest maximum compressive true stress compared to the other alloying additions.

Looking at trends within the alloying additions, samarium has a continual increase in maximum true stress with increasing solute content, that appears constant up to approximately 0.4 at%, at which point further increases are seen, but at a reduced rate. Gadolinium has very marginal gains (if not stagnant) in maximum compressive true stress with increased solute content, up until 0.4 at% at which point significantly greater slope is seen. As alluded to previously, scandium initially has a lower maximum compressive true stress than magnesium, but plateaus quickly to roughly the same value as magnesium.
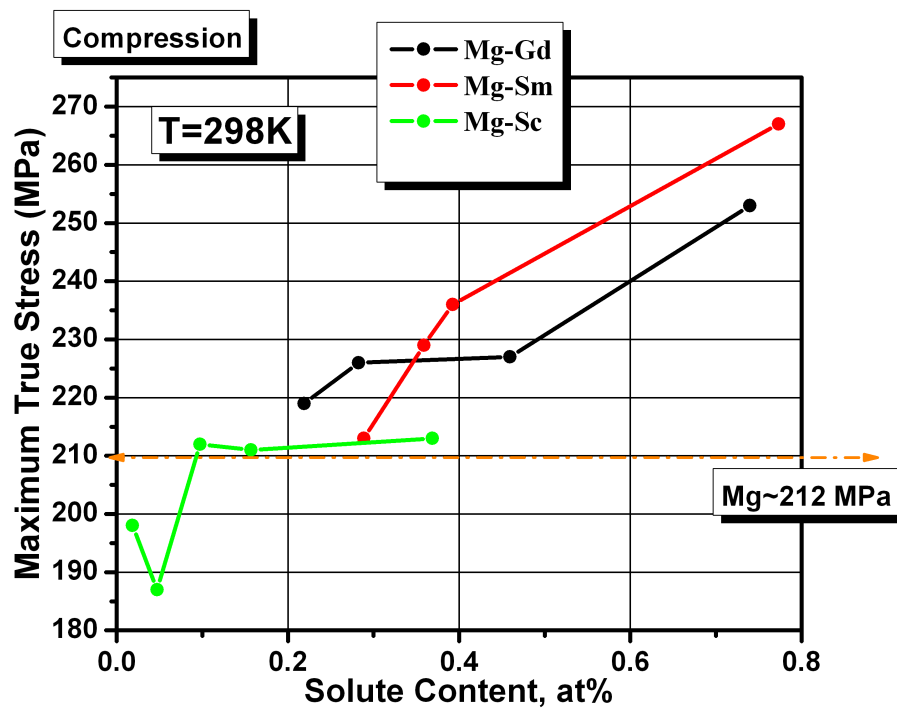
Figure 3.36: Maximum Compressive True Stress vs Concentration for Alloys Tested

3.2.2 Work Hardening Behaviour in Compression

The work hardening results of compressive testing plotted against true strain and effective stress for each alloy class are depicted in the following figures: Mg-Gd in Figure 3.37, Mg-Sm in Figure 3.39 and Mg-Sc in Figure 3.41. For Mg-Gd alloys shown in Figure 3.37(a), with increasing solute content, the extent of the work hardening extends to larger true strains. When plotted against effective stress (Figure 3.37(b)), the hardening of all Mg-Gd alloys is lower than the work hardening capacity of pure magnesium in compression. From 0.22 at% Gd to 0.28 at% Gd, the increase in solute increases the work hardening capacity. Further increases in solute content decrease the work hardening capacity (as seen in 0.46 at% Gd and 0.74 at% Gd). Additionally, if the plateau of constant work hardening is examined, we can see that the extent of that plateau increases from 0.22 at% Gd to 0.28 at%, but then decreases with further solute content additions. Finally, the upward inflection of the curve, characteristic of twinning, decreases in slope with increased solute content.
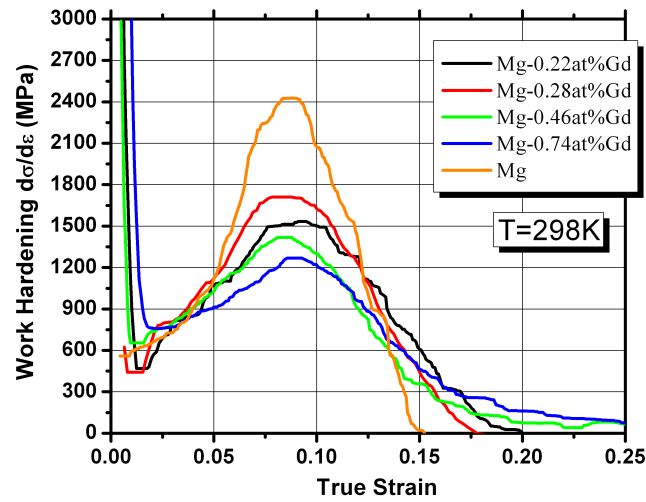
(a) Work Hardening vs Strain in Compression for Mg-Gd alloys
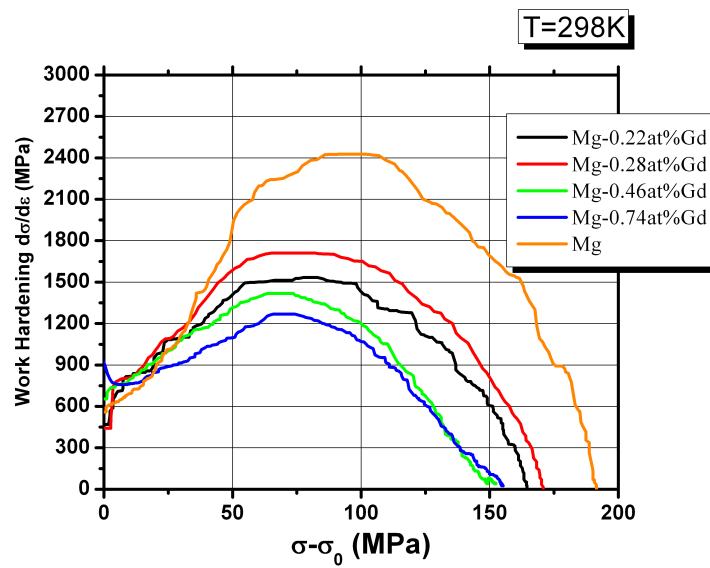
(b) Work Hardening vs Stress in Compression Mg-Gd aloys

Figure 3.37: Compressive Work Hardening Results for Mg-Gd alloys

In compression, there are two unique stages seen within the work hardening behaviour. Initially, at low effective stress, there is a region of constant work hardening, and then at higher effective stress a plateau region is observed. After the plateau of constant work hardening, the decrease of work hardening is observed corresponding to tensile Stage III of work hardening. Figure 3.38 highlights these two regions in the Mg-Gd alloys. The initial hardening rates for these two regions of constant work hardening are displayed in Table 3.7, in which the first plateau is coined "Stage A", and the second plateau is coined "Stage B". Considering "Stage A", Θ_0 increases with increasing solute, at which point 0.46 at% and 0.74 at% Gd have a higher initial rate than magnesium. Considering "Stage B", Θ_0 initially increases to 0.28 at% Gd, but then decreases with increasing solute. None of the compositions exceed the initial hardening value of magnesium in "Stage B".

(a) 'Stage A' Work Hardening Behaviour in Mg-Gd Compression Testing

(b) 'Stage B' Work Hardening Behaviour in Mg-Gd Compression Testing

Figure 3.38: 'Stage A' and 'Stage B' Work Hardening Behaviour for Mg-Gd in Compression

As seen with the tensile work hardening behaviour, the compressive work hardening behaviour is greatly varied from that of gadolinium. In Figure 3.39(a), the lowest solute

Table 3.7: Initial Hardening Rate for Mg-Gd Alloys in Compression

Composition (at%)	'Stage A'Θ_0 (GPa)	'Stage B'Θ_0 (GPa)
Mg	0.6	2.4
0.22	0.48	1.5
0.28	0.52	1.7
0.46	0.65	1.4
0.74	0.77	1.3

content alloy (0.22 at% Sm) has an identical work hardening behavior to pure magnesium, at which point further alloying decreases the height of the constant work hardening plateau, but extends to larger true strains. When plotted against effective stress (Figure 3.39(b)), all of the Mg-Sm have similar or lower work hardening capacity compared to that of magnesium in compression. From 0.36 at% Sm to 0.77 at% Sm, the increase in solute has minimal impact on the work hardening capacity; however, with increasing solute content, the upward inflection of the curve, characteristic of twinning, decreases in slope.

Figure 3.40 highlights "Stage A" and "Stage B" in the Mg-Sm alloys. The initial hardening values for these two areas on constant work hardening are displayed in Table 3.8. Considering "Stage A", Θ_0 increases with increasing solute, with all alloys having a higher initial rate than magnesium. Considering "Stage B", 0.22 at% Sm has a Θ_0 value equal to that of magnesium. However, increasing solute above 0.22 at% Sm decreases the Θ_0 value from 2.4 GPa to 1.7 GPa, which is then constant with increasing solute.
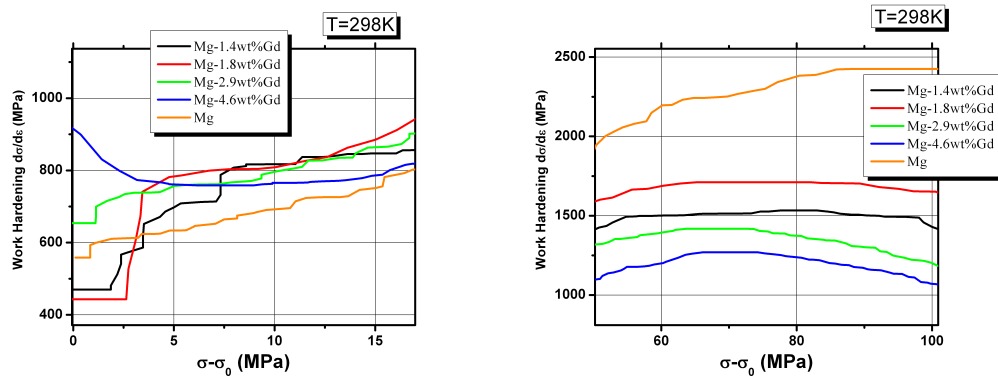
(a) Work Hardening vs Strain in Compression for Mg-Sm alloys
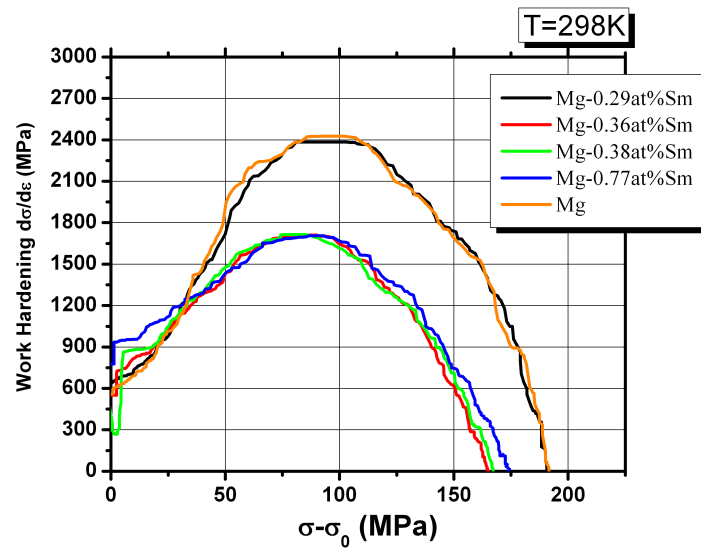
(b) Work Hardening vs Stress in Compression Mg-Sm alloys

Figure 3.39: Compressive Work Hardening Results for Mg-Sm alloys

(a) 'Stage A' Work Hardening Behaviour in Mg-Sm Compression Testing

(b) 'Stage B' Work Hardening Behaviour in Mg-Sm Compression Testing

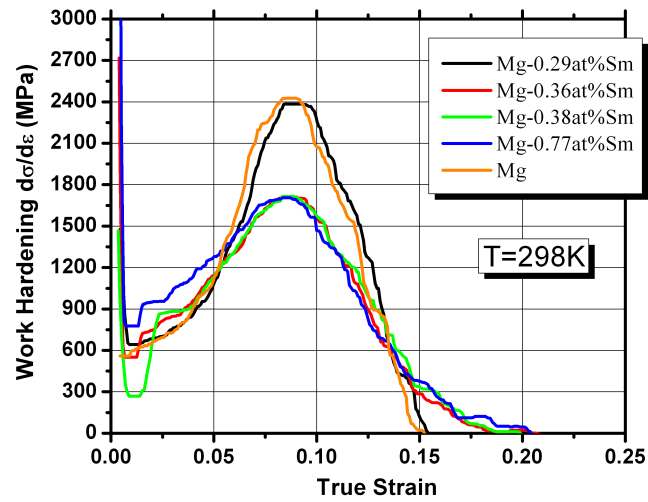Figure 3.40: 'Stage A' and 'Stage B' Work Hardening Behaviour for Mg-Sm in Compression

Table 3.8: Initial Hardening Rate for Mg-Sm Alloys in Compression

Composition (at%)	'Stage A'Θ_0 (GPa)	'Stage B'Θ_0 (GPa)
Mg	0.6	2.4
0.29	0.65	2.4
0.36	0.7	1.7
0.38	0.8	1.7
0.77	0.9	1.7

Mg-Sc alloys show interesting work-hardening behaviour, as seen in Figure 3.41(a). In the case of tensile deformation, it was discussed previously that the work hardening behaviour of 0.10 at% Sc mimics that of pure magnesium. Under compression on the other hand, two alloys with lower concentration of scandium (0.019 at% Sc and 0.05 at% Sc), exhibit a decrease in both the work hardening capacity, and the slope of the upward inflection of the work hardening curve (Figure 3.41(b)). Above 0.10 at% Sc, further alloying reduces the work hardening capacity, and again decreases the slope of the upward inflection of the work hardening curve. The largest constant work hardening plateau is seen in the 0.16 at% Sc alloy.
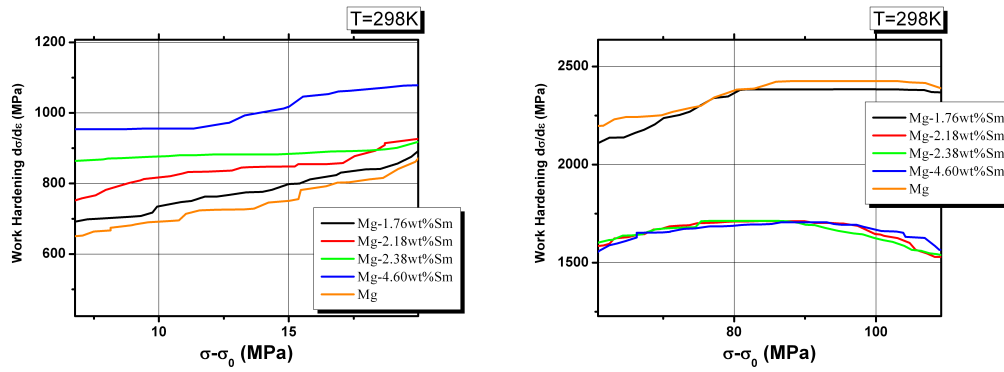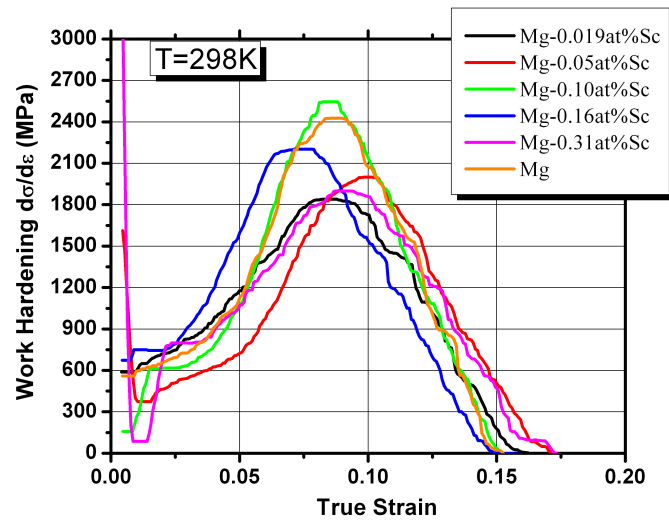
(a) Work Hardening vs Strain in Compression for Mg-Sc alloys
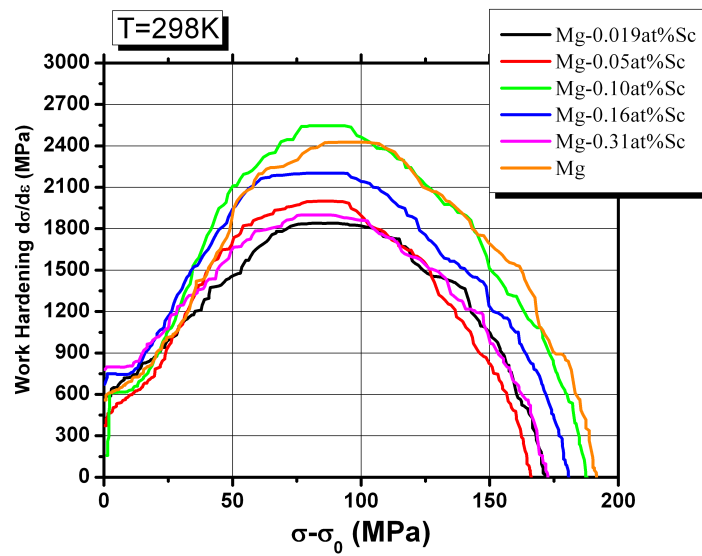
(b) Work Hardening vs Stress in Compression for Mg-Sc alloys

Figure 3.41: Compressive Work Hardening Results for Mg-Sc alloys

Table 3.9: Initial Hardening Rate for Mg-Sc Alloys in Compression

Composition (at%)	'Stage A' Θ_0 (GPa)	'Stage B' Θ_0 (GPa)
Mg	0.6	2.4
0.019	0.65	1.8
0.05	0.46	2.0
0.10	0.62	2.5
0.16	0.75	2.2
0.31	0.8	1.9

Figure 3.42 highlights "Stage A" and "Stage B" in the Mg-Sc alloys. The initial hardening values for these two regions of constant work hardening are displayed in Table 3.9. Considering "Stage A", Θ_0 increases with increasing solute, with all alloys except for 0.05 at% Sc, having a higher initial rate than pure magnesium. For "Stage B", 0.10 at% Sc has a Θ_0 value exceeding that of pure magnesium. Below this solute level, the initial hardening value is increasing, whereas above this solute level the initial hardening value is decreasing.
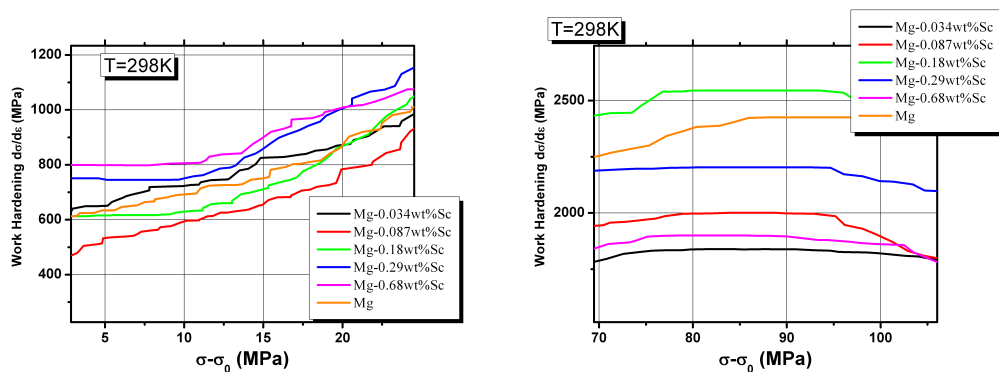

(a) 'Stage A' Work Hardening Behaviour in Mg-Sc Compression Testing

(b) 'Stage B' Work Hardening Behaviour in Mg-Sc Compression Testing

Figure 3.42: 'Stage A' and 'Stage B' Work Hardening Behaviour for Mg-Sc in Compression

3.3   Strain Rate Sensitivity

Haasen plots permit the evaluation of the impact of increasing solute content on the strain rate sensitivity parameter. As discussed before, strain rate sensitivity experiments have been conducted in both tension and compression. The data is represented as the strain state sensitivity characteristics obtained from stress rise and stress drop. When the strain rate was decreased from 2.8×10^{-4} s^{-1} to 2.8×10^{-5} s^{-1}, this is considered a stress drop, whereas returning to a strain rate of 2.8×10^{-4} s^{-1} from 2.8×10^{-5} s^{-1} represents a stress rise.

In Figure 3.43 and Figure 3.44, increasing solute content decreases the slope of the Haasen plot, to the point of having a negative slope with the highest solute content, 0.74 at% Gd. Additionally, the y-intercept for all Mg-Gd alloys is positive, suggesting that solute - dislocation interactions greatly affect the work hardening behaviour. The intercept value is relatively unchanged with increasing solute content. The strain rate sensitivity figures in tension are very similar to the figures obtained in compression experiments.

The strain rate sensitivity in tension and compression for all Mg-Gd is summarized in Table 3.10, and the variance of these values in regards to stress drop and stress rise is depicted in Figure 3.45.
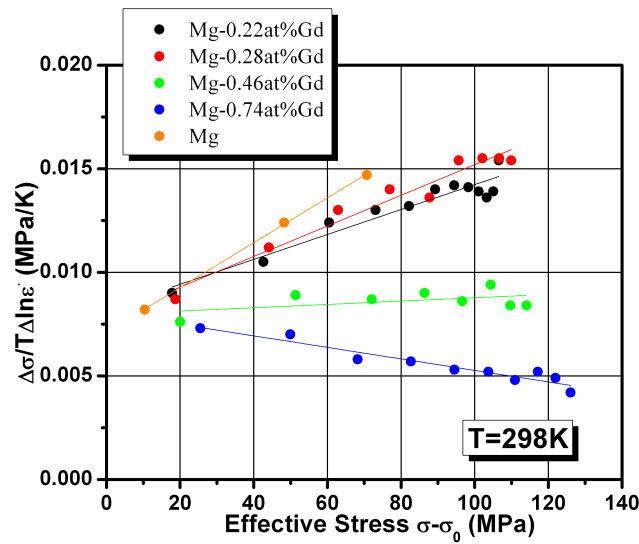
(a) Tension Haasen Plot for Mg-Gd determined from Stress Jump Down
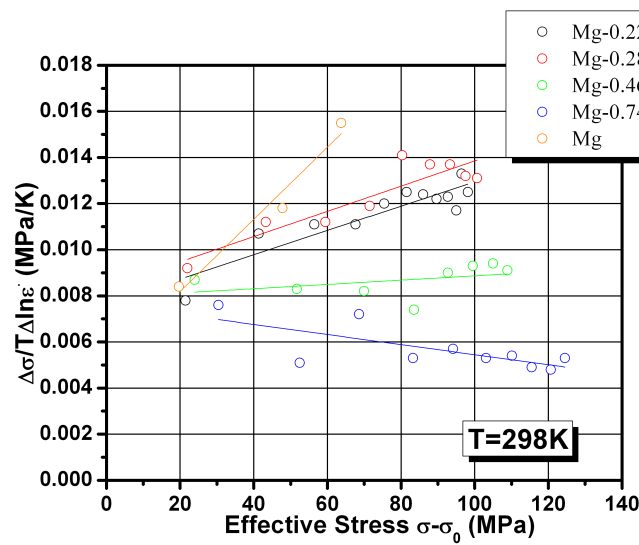
(b) Tension Haasen Plot for Mg-Gd determined from Stress Jump Up

Figure 3.43: Tension Haasen Plot for Mg-Gd alloys

(a) Compression Haasen Plot for Mg-Gd determined from Stress Jump Down

(b) Compression Haasen Plot for Mg-Gd determined from Stress Jump Up

Figure 3.44: Compression Haasen Plot for Mg-Gd alloys
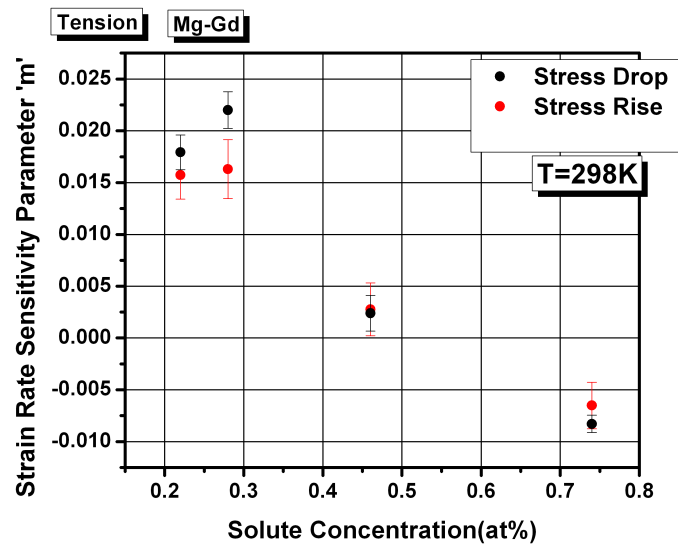
(a) Tension Strain Rate Sensitivity Measurements for Mg-Gd alloys
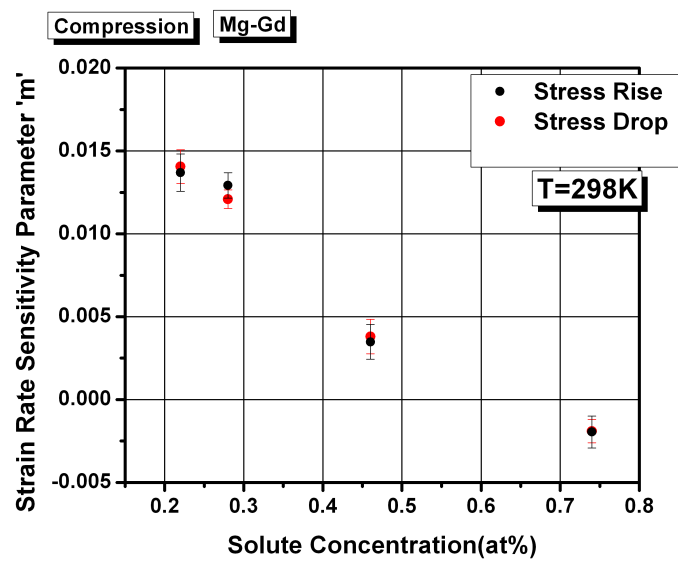
(b) Compression Strain Rate Sensitivity Measurements for Mg-Gd alloys

Figure 3.45: Changes in Strain Rate Sensitivity with Solute Concentration for Mg-Gd alloys

Table 3.10: Strain Rate Sensitivity of Mg-Gd Alloys

Mg-Gd Composition (at%)	Tensile SRS 'm'	Compressive SRS 'm'
0.22	1.63×10^{-2}	1.38×10^{-2}
0.28	1.77×10^{-2}	1.26×10^{-2}
0.46	2.75×10^{-3}	3.64×10^{-3}
0.74	-5.16×10^{-3}	-1.95×10^{-3}

In Figure 3.46, for tension, increasing solute content decreases the slope of the Haasen plot, to the point of having a negative slope with the highest solute content, 0.77 at% Sm. Contrary to the results observed in tension, with increasing solute content for Mg-Sm there is a slight decrease in the slope, however the slope is always positive, as depicted in Figure 3.47. Additionally, the y-intercept for all Mg-Sm alloys is positive, suggesting that solute - dislocation interactions greatly affect the work hardening behaviour. In tension, increasing the solute content increases the value of the y-intercept, thus it can be suggested that the solute - dislocation interactions become greater as the solute content increases. Conversely, in compression, increasing solute does not impact the y-intercept value, which remains relatively stable.

The strain rate sensitivity in tension and compression for all Mg-Sm is summarized in Table 3.11, and the variance of these values in regards to stress drop and stress rise is depicted in Figure 3.48.
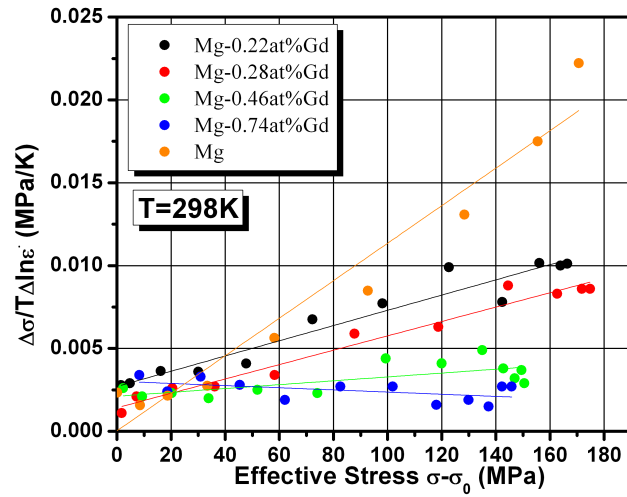
(a) Tension Haasen Plot for Mg-Sm Stress Jump Down

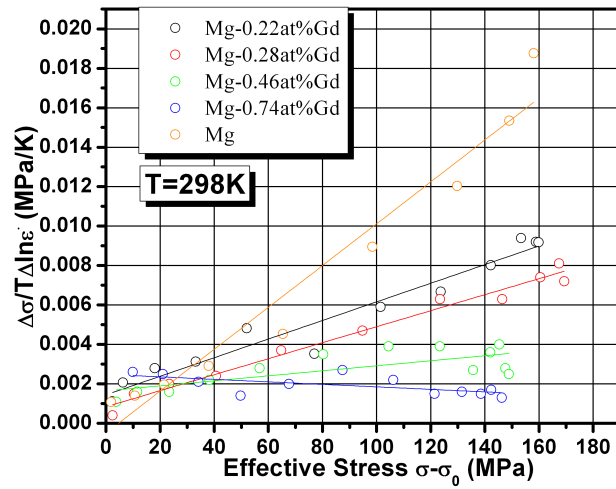(b) Tension Haasen Plot for Mg-Sm Stress Jump Up

Figure 3.46: Tension Haasen Plot for Mg-Sm

(a) Compression Haasen Plot for Mg-Sm Stress Jump Down


(b) Compression Haasen Plot for Mg-Sm Stress Jump Up

Figure 3.47: Compression Haasen Plot for Mg-Sm
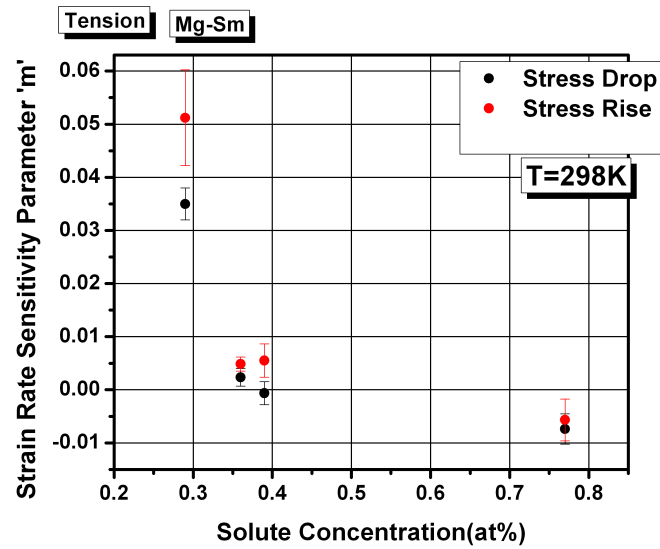
(a) Tension Strain Rate Sensitivity Measurements Mg-Sm
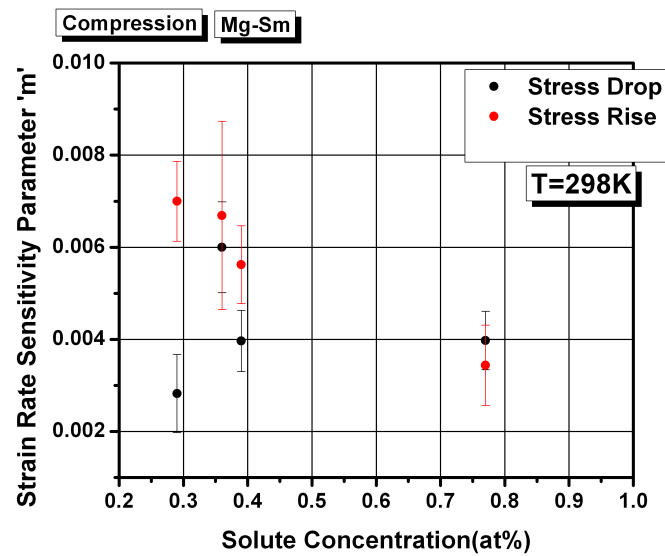
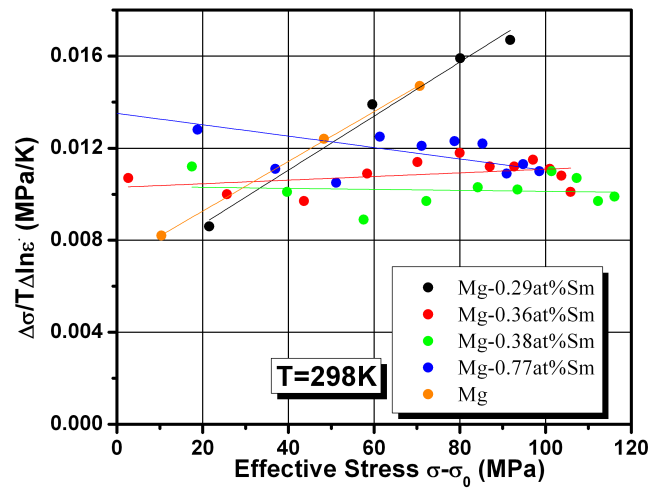

(b) Compression Strain Rate Sensitivity Measurements Mg-Sm

Figure 3.48: Changes in Strain Rate Sensitivity with Solute Concentration for Mg-Sm
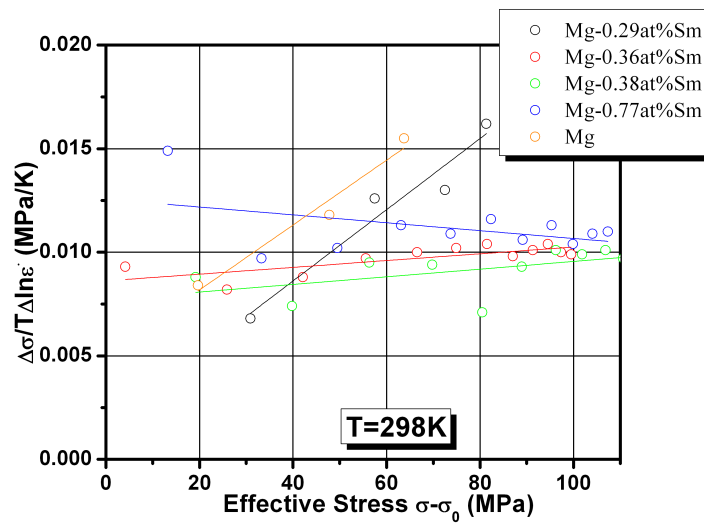
Table 3.11: Strain Rate Sensitivity of Mg-Sm Alloys

Mg-Sm Composition (at%)	Tensile SRS 'm'	Compressive SRS 'm'
0.29	4.61×10^{-2}	4.92×10^{-3}
0.36	3.45×10^{-3}	6.69×10^{-3}
0.38	2.92×10^{-3}	4.88×10^{-3}
0.77	-5.98×10^{-3}	3.59×10^{-3}

The Haasen plot of Mg-Sc for the tensile SRS is depicted in Figure 3.49. It is seen that increasing solute content results in minimal changes to the slope of the curves. This trend was also observed in the compressive SRS experiments, shown in Figure 3.50. Additionally, the y-intercept for all Mg-Sc alloys tested in tension are positive, suggesting that solute - dislocation interactions greatly affect the work hardening behaviour. Conversely, in compression, the y-intercept is close to the origin, suggesting that dislocation-dislocation interactions dominates the work hardening behaviour, even with increasing solute content.

The strain rate sensitivity in tension and compression for all Mg-Sc is summarized in Table 3.12, and the variance of these values in regards to stress drop and stress rise is depicted in Figure 3.51.
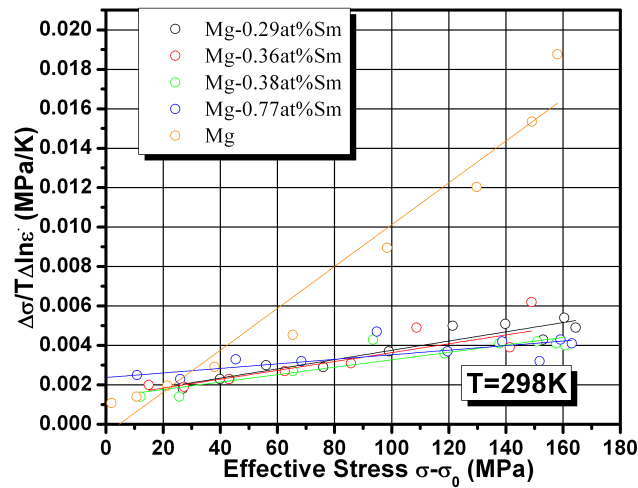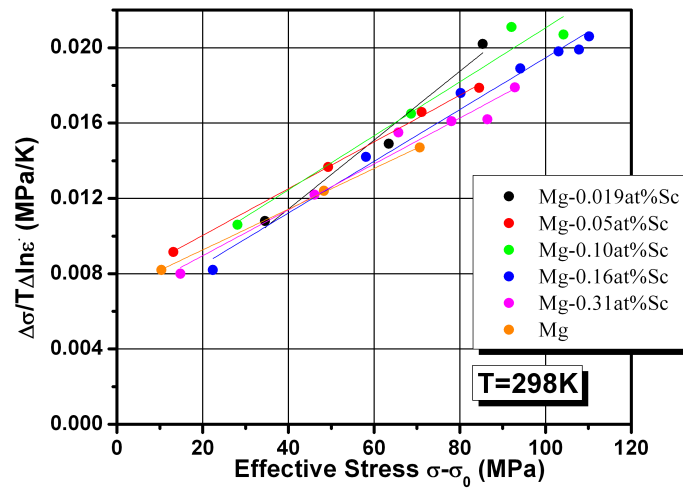
(a) Tension Haasen Plot for Mg-Sc Stress Jump Down
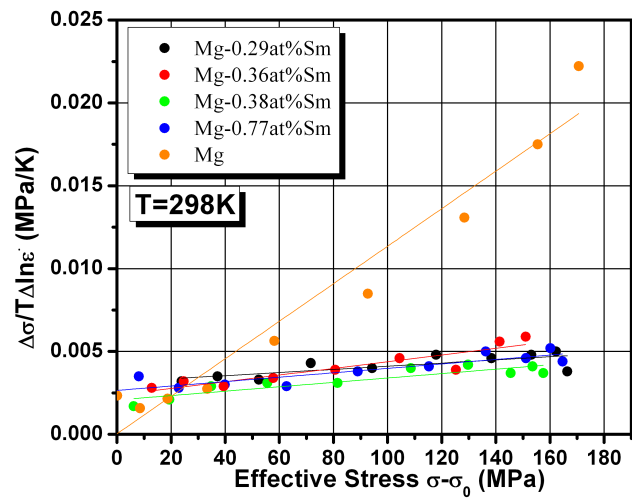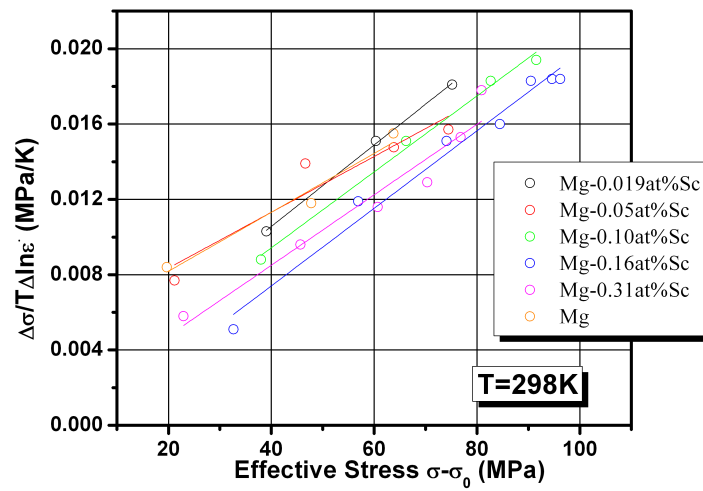

(b) Tension Haasen Plot for Mg-Sc Stress Jump Up

Figure 3.49: Tension Haasen Plot for Mg-Sc
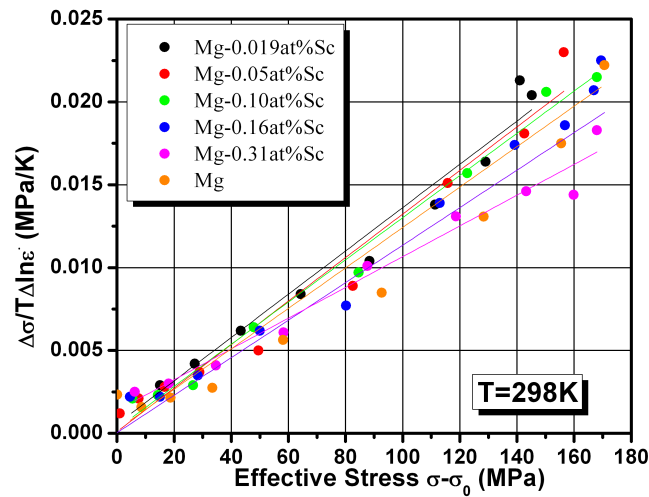
(a) Compression Haasen Plot for Mg-Sc Stress Jump Down
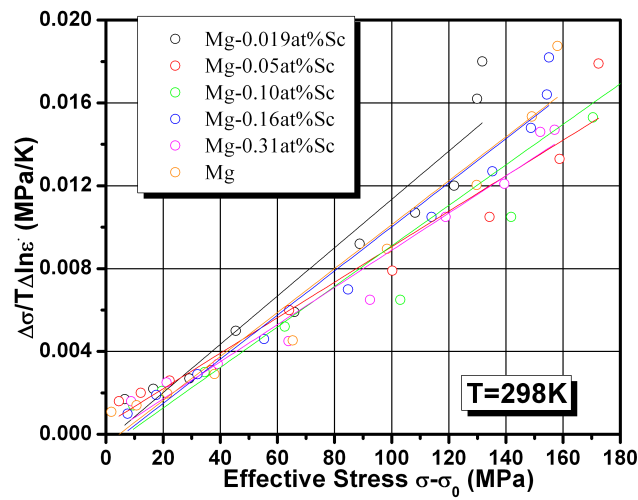
(b) Compression Haasen Plot for Mg-Sc Stress Jump Up

Figure 3.50: Compression Haasen Plot for Mg-Sc
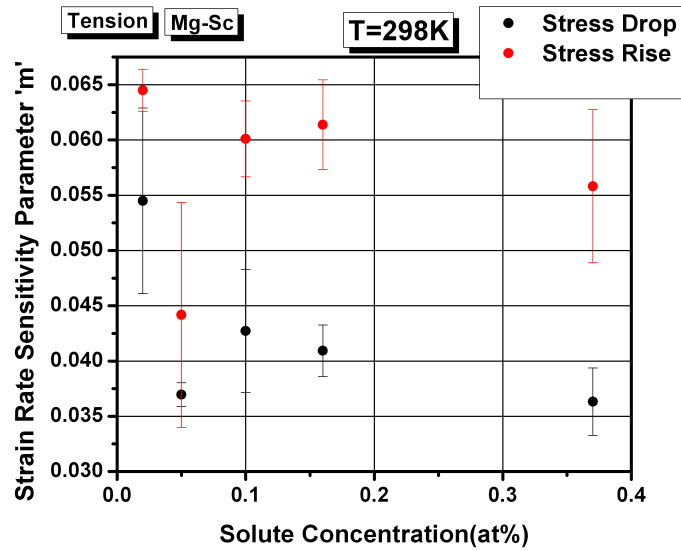
(a) Tension Strain Rate Sensitivity Measurements Mg-Sc
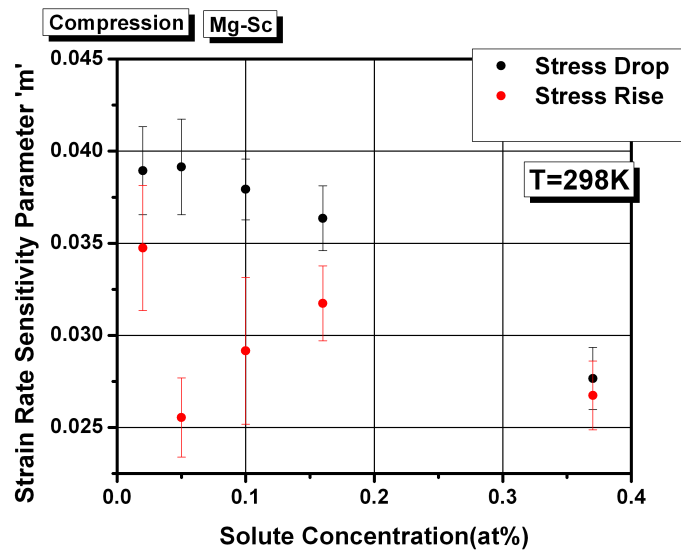
(b) Compression Strain Rate Sensitivity Measurements Mg-Sc

Figure 3.51: Changes in Strain Rate Sensitivity with Solute Concentration for Mg-Sc

Table 3.12: Strain Rate Sensitivity of Mg-Sc Alloys

Mg-Sc Composition (at%)	Tensile SRS 'm'	Compressive SRS 'm'
0.019	5.45×10^{-2}	3.89×10^{-2}
0.05	5.11×10^{-2}	3.65×10^{-2}
0.10	4.42×10^{-2}	3.15×10^{-2}
0.16	5.11×10^{-2}	3.16×10^{-2}
0.31	4.94×10^{-2}	2.99×10^{-2}

3.4   Texture

Following the method outline in Section 2.4, the recalculated pole figure for the basal plane has been re-created in Figures 3.52 - 3.58. The normal of the pole figure corresponds to the rolling direction. During machining of the samples, the orientation of the samples relative to the sheet plane were not tracked and there is no obvious correlation between directions of the sample with relation to the transverse direction and normal direction of the sheet. For each set of pole figures, the colouring is normalized to the highest intensity sample, so that the comparison across different compositions can be made.

The texture measurements of the annealed Mg-Gd samples are presented in Figure 3.52, whereas texture measurements for compressed samples and samples deformed in tension are shown in Figure 3.53 and Figure 3.54. The basal planes of the annealed samples show an increase in intensity normal to the pole figure (along Normal Direction (ND)) with increasing solute up to 0.46 at%, after which random basal texture is observed. Mg-0.46 at% shows the strongest selective texture of all four samples, where the lower compositions of gadolinium have strong features in the normal direction of the pole figure, but also have intensity radially away from the normal direction that is equal in intensity to the concentrated area at the normal direction. Evaluating the texture of the compressed samples, one observes that regardless of the composition, the intensity is focused around the normal of the pole figure (i.e., ND direction). This would denote that the basal poles would be preferentially aligned parallel to the compression axis, i.e. basal (0001) planes perpendicular to the compression axis. In tension, the intensity is spread towards the edge of pole figure, in which the highest intensity is seen in the 0.28 at% sample. There is slight intensity spread towards the centre of the pole figure, however this texture strength decreases with increasing solute.

(a) Mg-0.22at%Gd

(b) Mg-0.28at%Gd

(c) Mg-0.46at%Gd

(d) Mg-0.74at%Gd
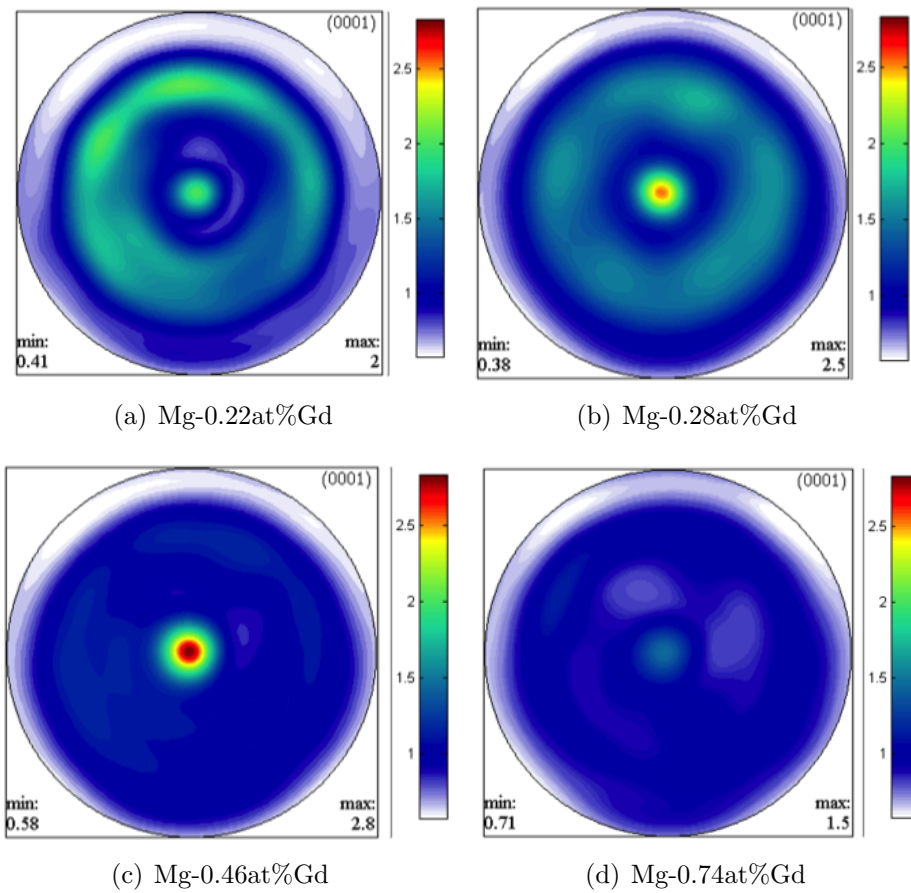
Figure 3.52: Basal Pole Figures for Annealed Mg-Gd Specimens.

(a) Mg-0.22at%Gd

(b) Mg-0.28at%Gd

(c) Mg-0.46at%Gd

(d) Mg-0.74at%Gd
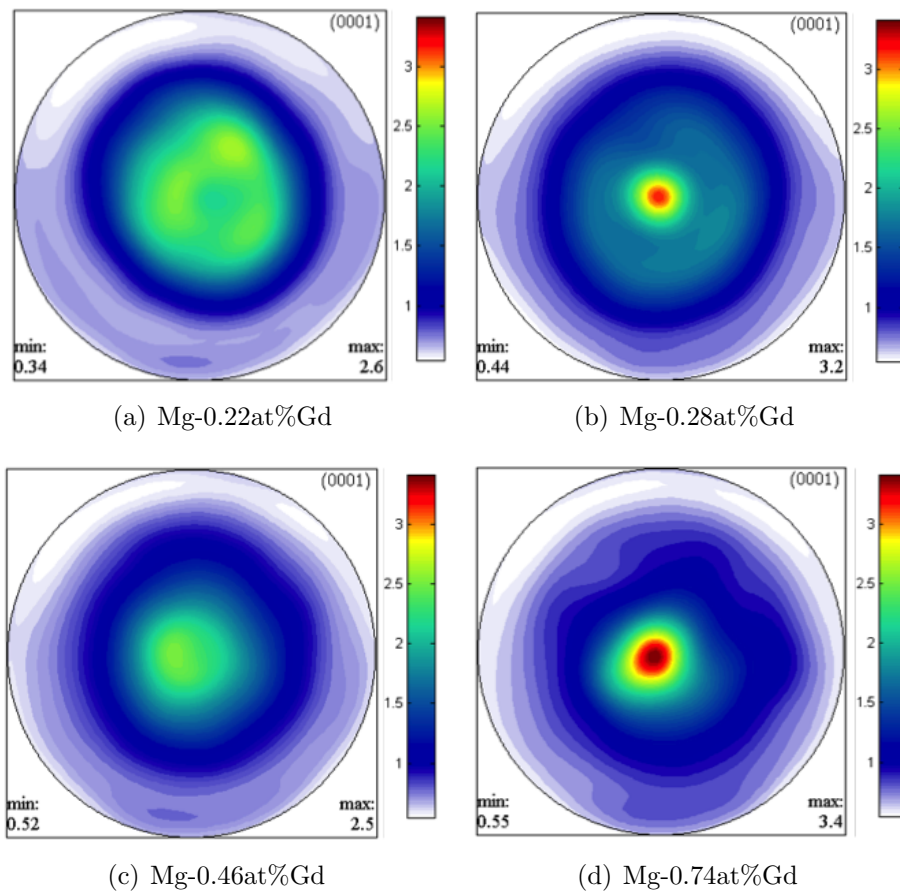
Figure 3.53: Basal Pole Figures for Compression Mg-Gd Specimens.

(a) Mg-0.22at%Gd   (b) Mg-0.28at%Gd

(c) Mg-0.46at%Gd   (d) Mg-0.74at%Gd

Figure 3.54: Basal Pole Figures for Tension Mg-Gd Specimens.

The texture measurements of the annealed Mg-Sm samples are presented in Figure 3.55. Figure 3.56 and 3.57 show the texture measurements of compression and tensile deformed samples. Looking at the (0002) pole figure, the annealed samples at the lowest solute content have miminal intensity in the centre of the pole figure, thus the c-axis of the unit cell is not parallel with the rolling direction. As the solute content increases, the texture randomizes and eventually a strong basal texture is seen with the highest solute content, 0.77 at% Sm, in which the c-axis of the unit cell is preferentially aligned parallel to the rolling direction. Evaluating the compression pole figures, above 0.29 at% Sm, the intensity is centred around the normal direction of the pole figure. Additionally, one observes splitting of the basal pole intensities at 0.36 at%. In the highest solute content Mg-0.77 at% Sm alloy, the intensity is centred in the middle of the pole figure, and decreases out radially. In tension, the intensity is spread towards the edge of pole figure, in which the highest intensity of basal poles is seen in the 0.29 at% sample. Above 0.36 at%, the intensity in the centre of the pole figure diminishes, thus the basal planes are predominately rotated close to the orientation perpendicular to the tensile axis.

(a) Mg-0.29at%Sm

(b) Mg-0.36at%Sm

(c) Mg-0.38at%Sm

(d) Mg-0.77at%Sm
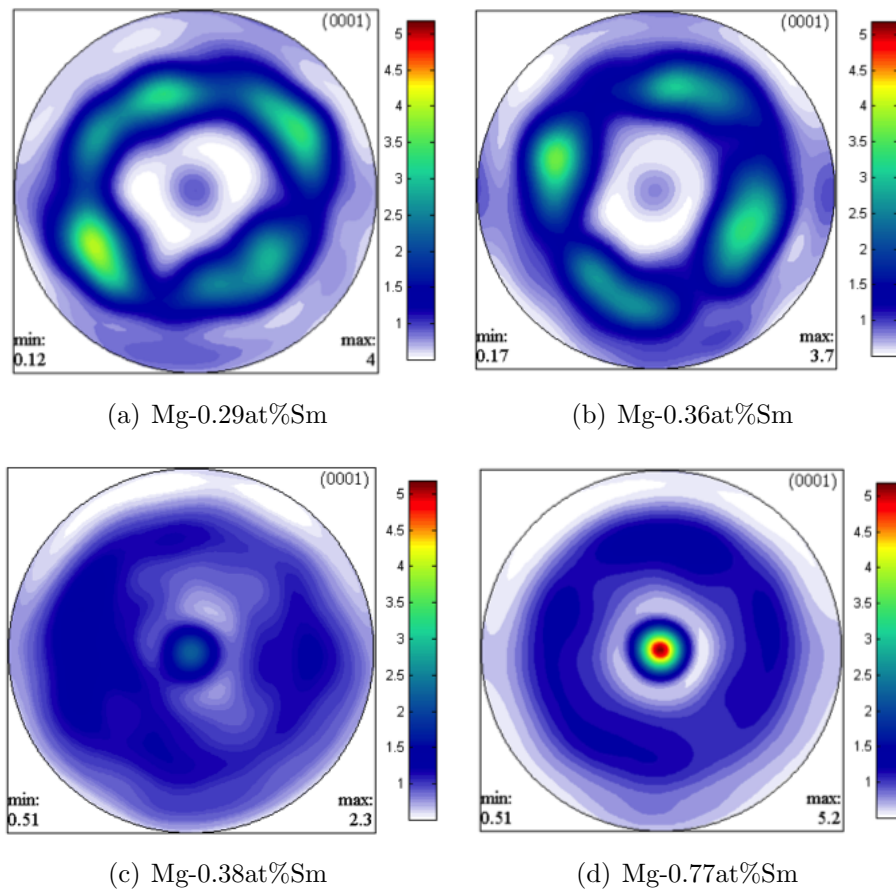
Figure 3.55: Basal Pole Figures for Annealed Mg-Sm Specimens.

(a) Mg-0.29at%Sm

(b) Mg-0.36at%Sm

(c) Mg-0.38at%Sm

(d) Mg-0.77at%Sm
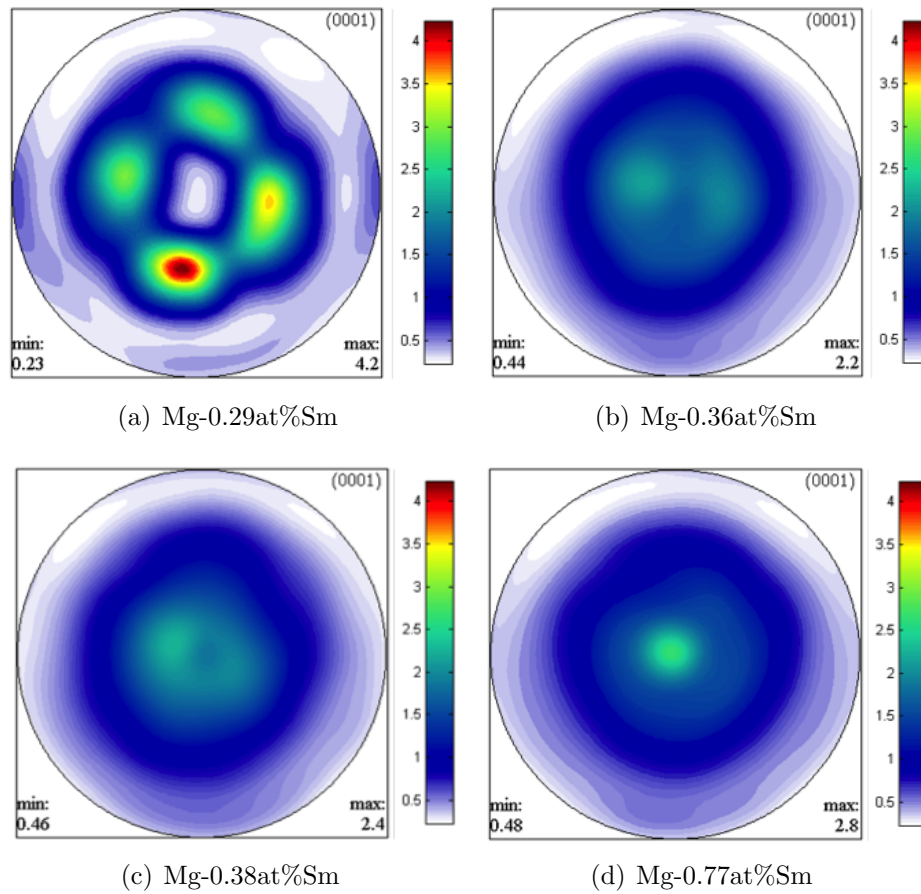
Figure 3.56: Basal Pole Figures for Compression Mg-Sm Specimens.

(a) Mg-0.29at%Sm

(b) Mg-0.36at%Sm

(c) Mg-0.38at%Sm

(d) Mg-0.77at%Sm
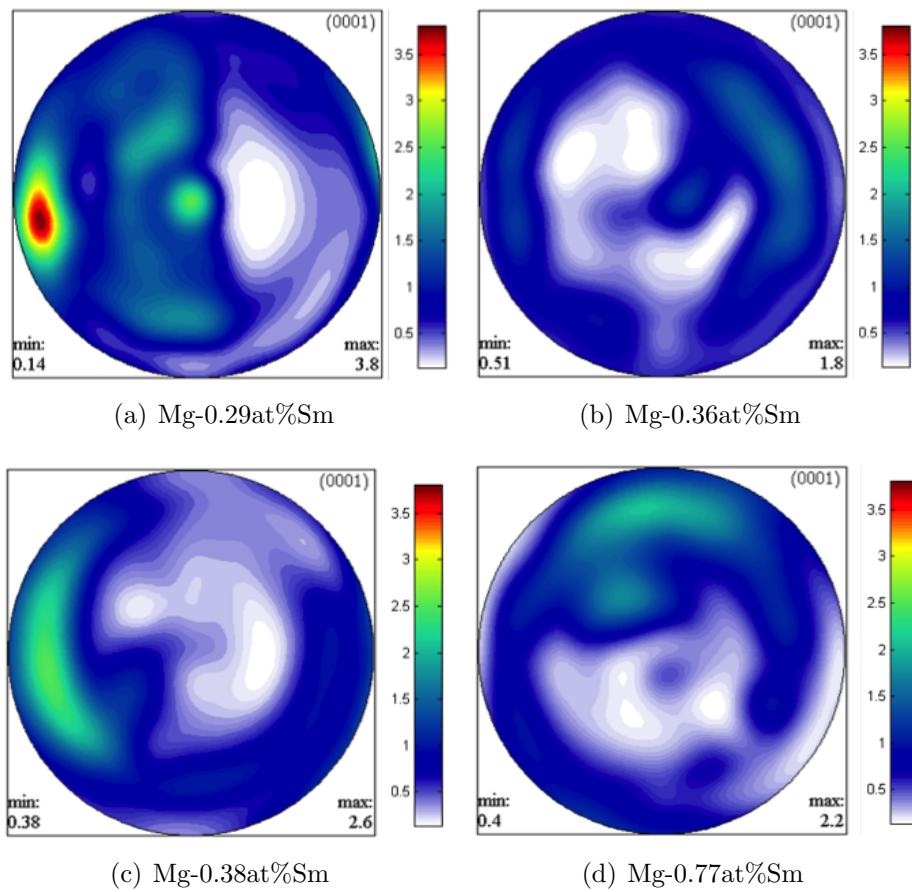
Figure 3.57: Basal Pole Figures for Tension Mg-Sm Specimens.
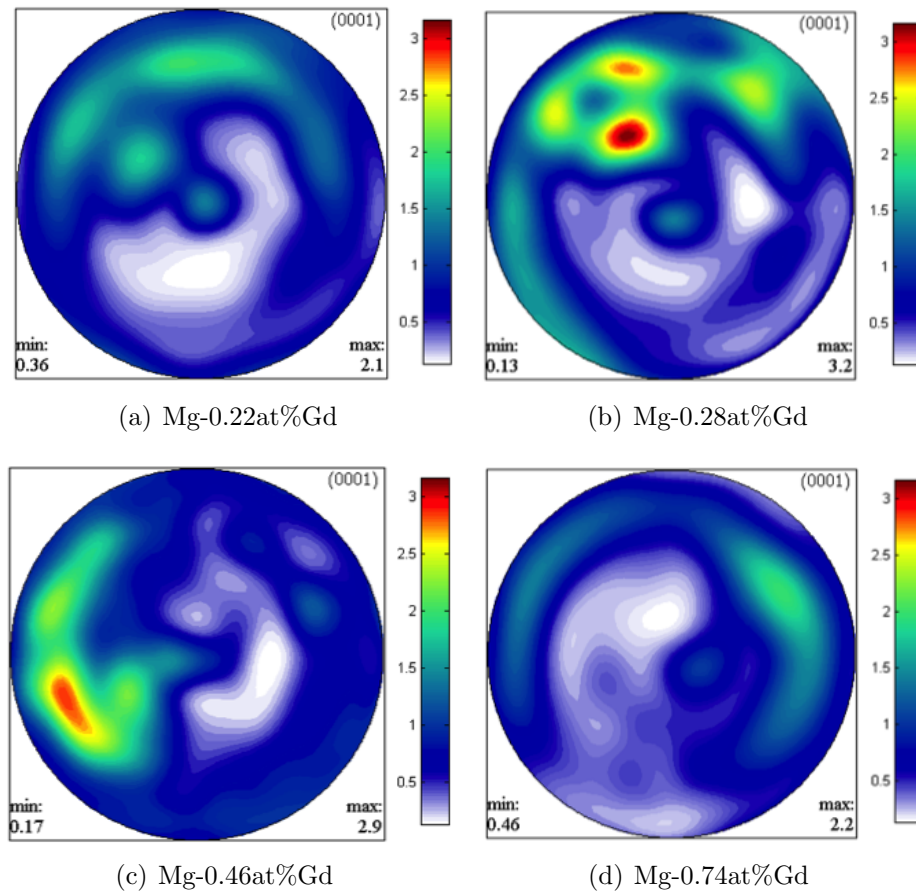
The texture measurement of the annealed Mg-Sc samples are presented in Figure 3.58. The textures of compressed and tensile deformed specimens are presented in Figure 3.59 and Figure 3.60. The basal planes of the annealed samples show an increase in intensity normal to the pole figure with increasing solute. Initially there is no intensity normal to the pole figure at the lowest composition (0.019 at%), and then maximum intensity is seen at 0.16 at%, followed by very random texture at the highest solute content of 0.31 at%. Evaluating the compression pole figures, it is interesting to note that the orientation does not change significantly relative to the annealed texture. There is a significant weakening of texture strength seen for Mg-0.16 at% Sc compared to the annealed sample, but no other scandium alloy exhibit that significant difference in texture strength from anneal to compressed. In tension, the highest intensity is realized in the 0.019 at% sample. The intensity is spread towards the outer edges on the pole figure, however unlike the other binary systems, with increasing solute content there is increasing intensity in the middle of the pole figure. This would lead to a random orientation in which there are basal pole figures aligned parallel and perpendicular to the tensile axis.

(a) Mg-0.019at%Sc

(b) Mg-0.05at%Sc

(c) Mg-0.10at%Sc

(d) Mg-0.16at%Sc

(e) Mg-0.31at%Sc
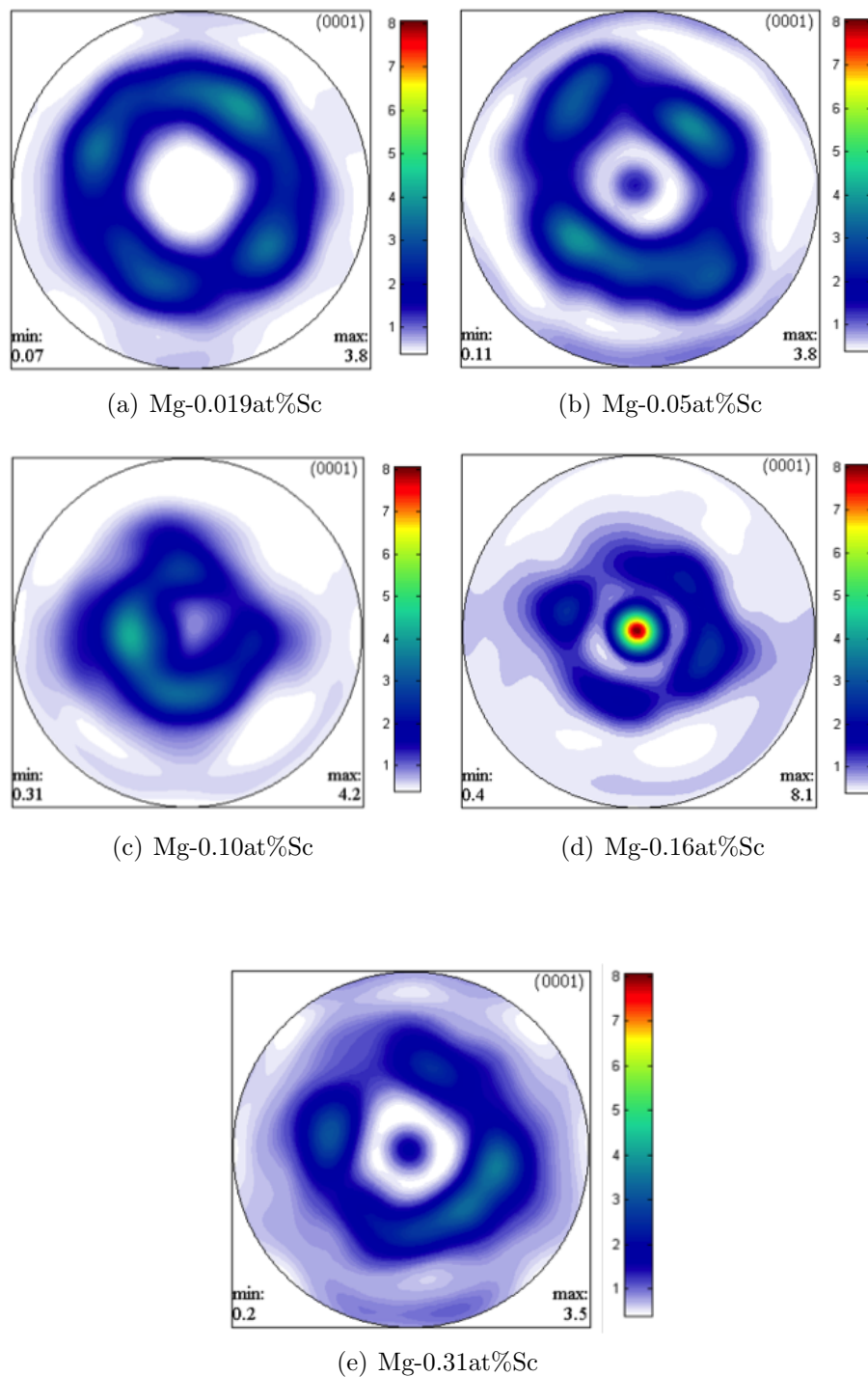
Figure 3.58: Basal Pole Figures for Annealed Mg-Sc Specimens.

(a) Mg-0.019at%Sc

(b) Mg-0.05at%Sc

(c) Mg-0.10at%Sc

(d) Mg-0.16at%Sc

(e) Mg-0.31at%Sc
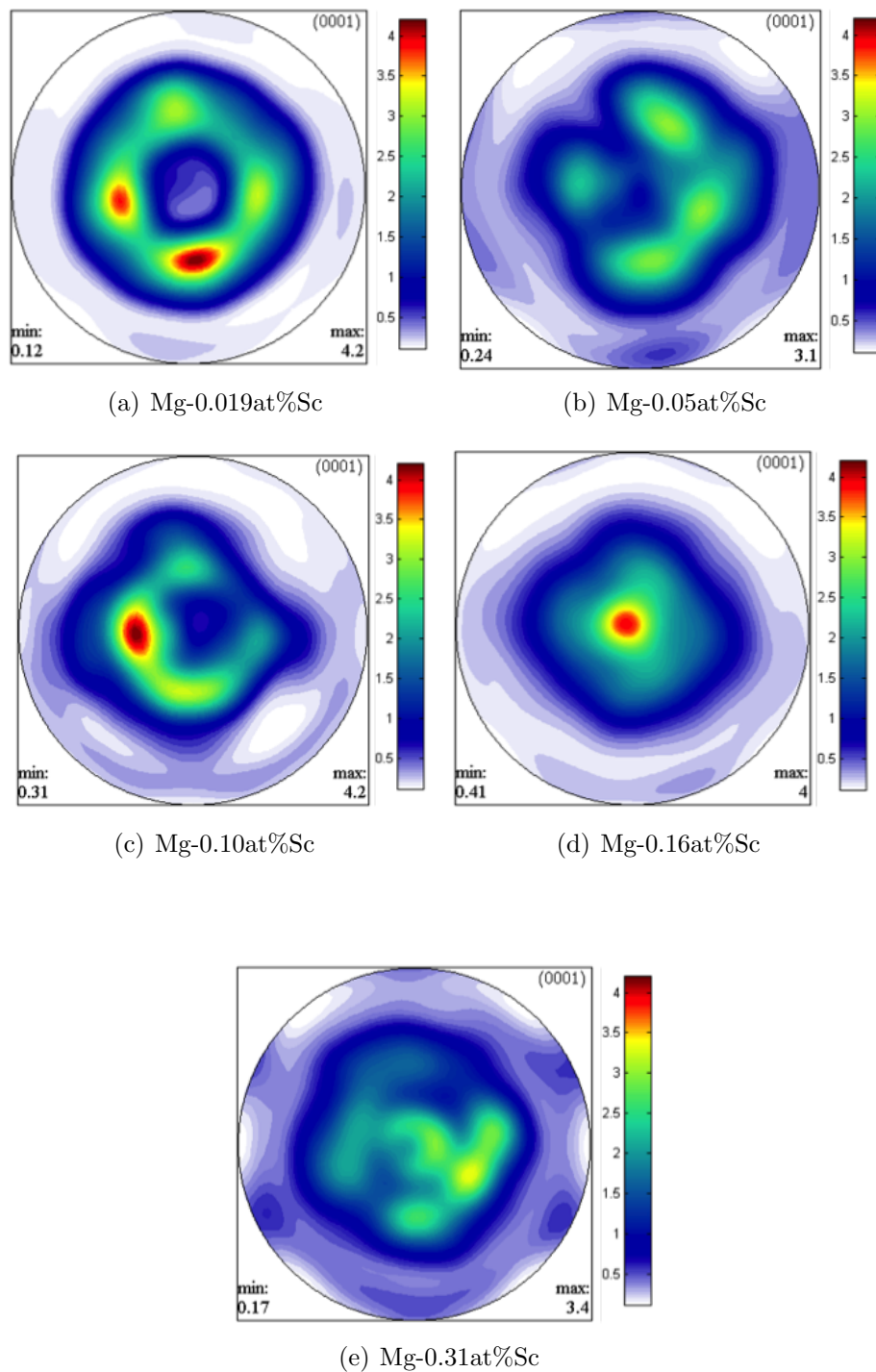
Figure 3.59: Basal Pole Figures for Compression Mg-Sc Specimens.

(a) Mg-0.019at%Sc   (b) Mg-0.05at%Sc

(c) Mg-0.10at%Sc   (d) Mg-0.16at%Sc

(e) Mg-0.31at%Sc
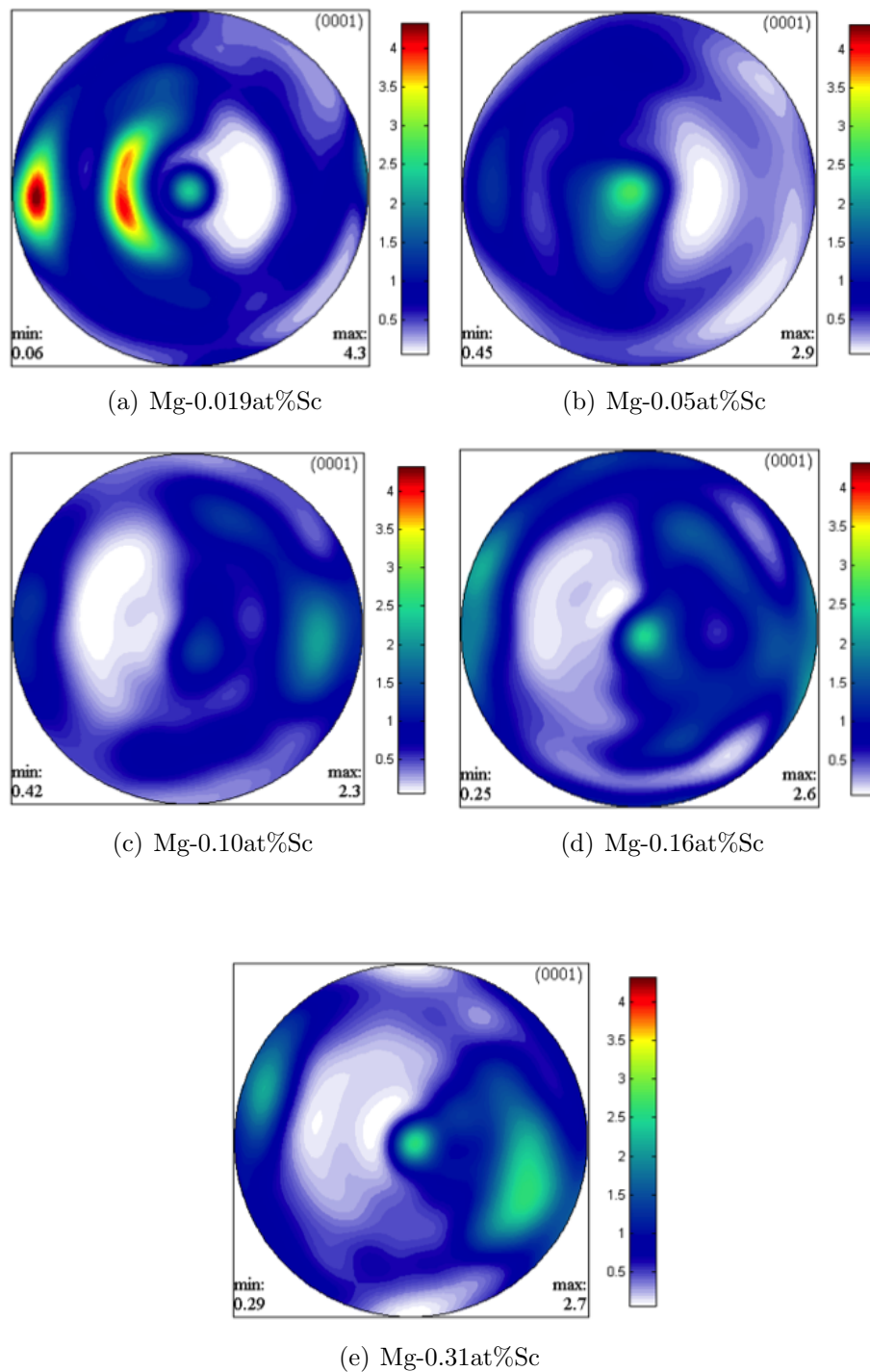
Figure 3.60: Basal Pole Figures for Tension Mg-Sc Specimens.

Finally, magnesium basal pole figures are plotted in Figure 3.61. The annealed samples show stronger intensity of the diffraction peaks towards the edges of the pole figure, suggesting that the basal poles are close to a perpendicular alignment to the compression direction. In the compression sample, the orientation suggests that the basal poles initially perpendicular to the compression axis, rotate towards the compression axis during deformation. The texture of the tensile deformed Mg sample is different from the texture of annealed and compression deformed samples, in which higher intensity of the basal poles is located towards the edge of the pole figure. This suggests that, as expected, rotation of the basal poles occurs in opposite direction than in compression samples.

(a) Mg-Annealed　　　　　　　(b) Mg-Compressed

(c) Mg-Tensile
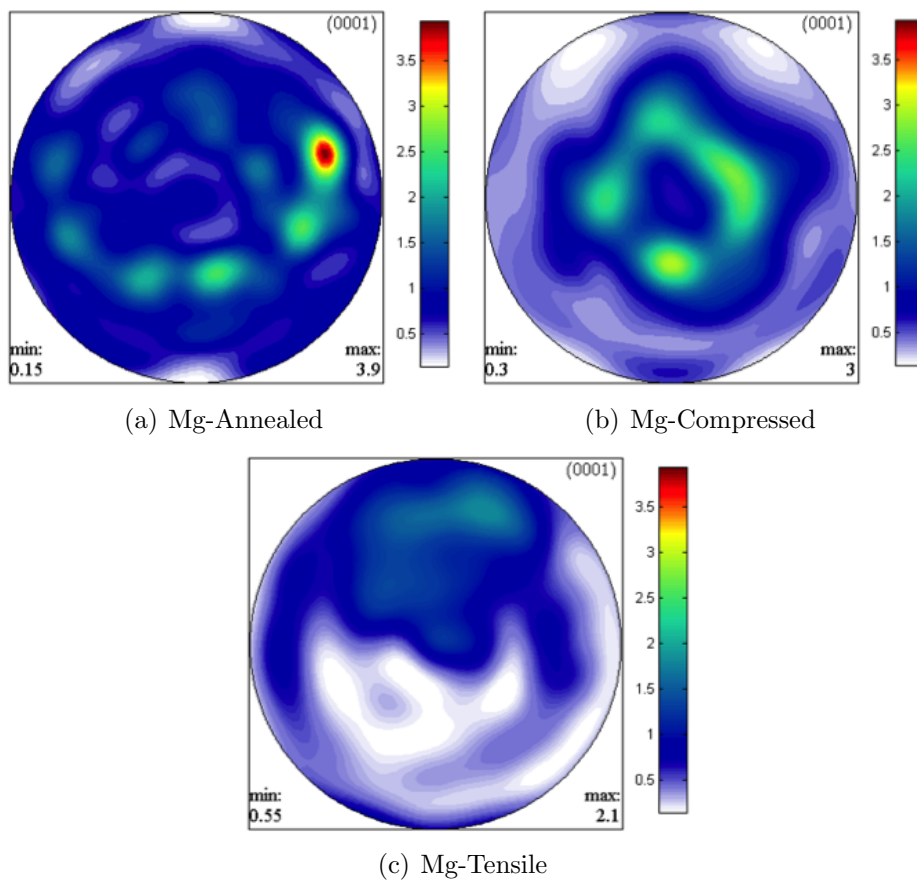
Figure 3.61: Basal Pole Figures for Annealed, Compression, and Tension Mg Specimens.

Chapter 4

Discussion

4.1 Mechanical Properties

The flow stress of a material is defined as the contribution of the yield strength of the material and the work hardening after yielding (Mecking and Kocks, 1981) :

$$\sigma = \sigma_{ys} + \alpha\mu b\sqrt{\rho} \qquad (4.1)$$

The alloying additions to magnesium had a marked impact on both the yield strength, reported in 4.1.1, and work hardening, reported in 4.1.2.

4.1.1 Yield Strength

The factors impacting the yield strength of the material are outlined in the following formula (Wang *et al.*, 2005):

$$\sigma_{ys} = \Delta\sigma_{gs} + M[\Delta\tau_o + \Delta\tau_{ss} + (\Delta\tau_D^2 + \Delta\tau_{ppt}^2)^{1/2}] \qquad (4.2)$$

With the alloys examined, the contributions of grain size, $\Delta\sigma_{gs}$, and solid solution harden-ing, $\Delta\tau_{ss}$ would be the only applicable variables in the experiment. The influence of grain size, known as the Hall-Petch relation, as well as the influence of solid solution hardening, are defined in the following formulas:

$$\Delta\sigma_{gs} = k_{gb}\frac{1}{\sqrt{d}} \tag{4.3}$$

$$\tau_{ss} = k_{ss}C^n \tag{4.4}$$

where d in the Hall Petch relationship represents the grain size of the material; C^n is the concentration of the solute atoms, in atomic percent, and n is equal to 1/2 (Fleischer) or 2/3 (Labusch).

Using the method outlined by Blake and Cáceres (2008), that was performed on other magnesium alloys, the grain size measurements were used to normalize the yield strength across the different solute levels within an alloy class. The Hall Petch relationship used by Blake and Cáceres (2008) was first detailed by Hauser *et al.* (1956) :

$$\sigma_{ys} = 11.8 + \frac{220}{\sqrt{d_{\mu m}}}(\text{MPa}) \tag{4.5}$$

In this regard, we can assume that the increase in yield strength is solely from the increasing solute level. Unfortunately, not enough time was spent on recrystalization studies to achieve a homogenous grain size due to the lack of material, caused by casting contraints and difficulties in producing the alloys. Gadolinium is a significant grain refiner, with a 3 fold difference in grain size from the lowest solute content alloy, 0.22 at%, to the highest, 0.74 at%, introducing potential error in the calculation of solute strengthening. In the other alloy classes, this difference in the grain size across the compositions is much less

pronounced, so the error introduced by the method outlined by Blake and Cáceres (2008) would be expected to be minimal.

The contribution of solid solution strengthening on the yield strength for both tension and compression for all alloys is presented in Figure 4.62 - 4.63.

Table 4.13: Fleischer Solid Solution Strengthing Parameter, k_{ss} (MPA/$\sqrt{at\%}$)

Alloy Class	Tension	Compression
Mg-Gd	138	746
Mg-Sm	1266	1092
Mg-Sc	863	665

Table 4.14: Labusch Solid Solution Strengthing Parameter, k_{ss} (MPA/$at\%^{2/3}$)

Alloy Class	Tension	Compression
Mg-Gd	258	1390
Mg-Sm	2258	1946
Mg-Sc	1883	1494
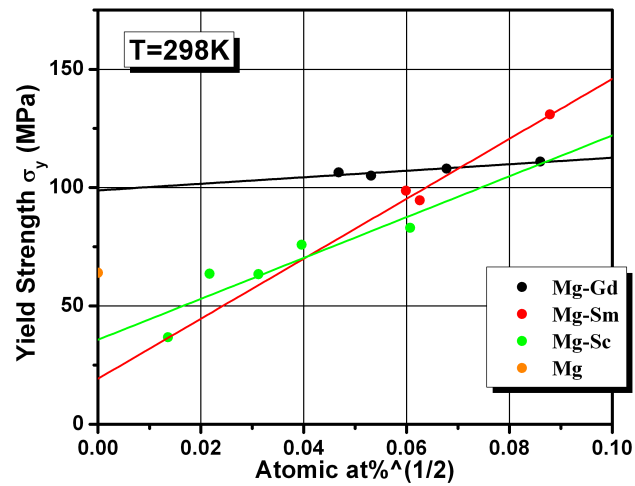
(a) Tension
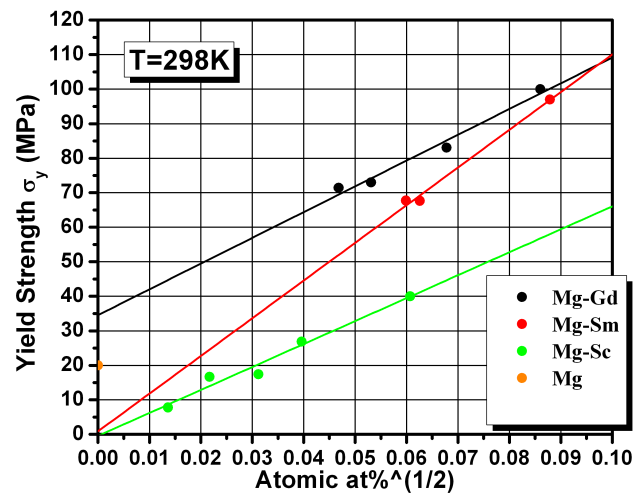
(b) Compression

Figure 4.62: Solid Solution Strengthing of Mg-RE Alloys (Fleischer)
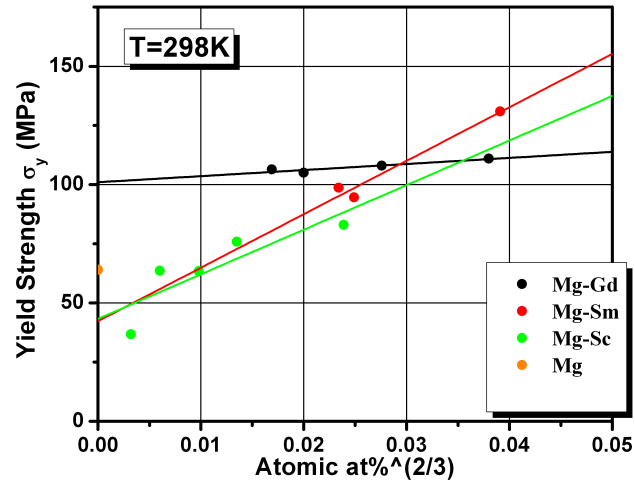
(a) Tension
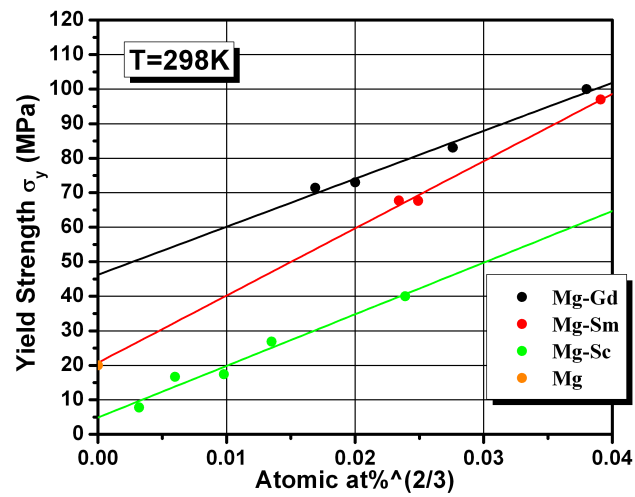
(b) Compression

Figure 4.63: Solid Solution Strengthing of Mg-RE Alloys (Labusch)

Samarium offers the greatest solid solution strengthening in both tension and compression relative to the other two binary systems. The greatest strengthening rate overall is seen in Mg-Sm in compression. Gadolinium in tension provides minimal additional strengthening with increasing solute, similar to what has been previously observed by Stanford *et al.* (2010b). Although increasing solute content in the Mg-Gd class is largely ineffective compared to the other binary systems, it has a significantly higher yield strength in tension at lower concentrations compared to Mg-Sc and Mg-Sm. In compression, the same is observed, with the yield strength in compression of Mg-Gd is larger than the other binary systems, however the strengthening rate in compression is not deficient compared to the strengthening rate of the other alloys.

Table 4.15: Corrected yield strength of magnesium relative to grain size

| Alloy Class	Reference Grain Size (μm)	Corrected $\sigma_{y,t}$(MPa)	Corrected $\sigma_{y,c}$(MPa)
Mg-Gd	28	85	41
Mg-Sm	65	71	27
Mg-Sc	120	64	20

Evaluating the experimental data fit with the Fleischer and Labusch models, it can be seen that large discrepancies exist at the y-axis of the graphs. Since the experimental data in each alloy class was normalized to a specific grain size to account for the Hall-Petch effect, the same normalization would have to be applied to pure magnesium, as shown in Table 4.15. Using this information, the validity in tension of all alloy classes to both the Fleischer and Labusch model of solid solution strengthening does not appear valid for the entire compositional range. In compression, it appears that solid solution strengthening of gadolinium is accurately predicted for the compositional range explored using both the

Fleischer and Labusch model. Additionally, the Labusch model appears to accurately pre-
dict the SSS of samarium in compression. It is to be noted that it was not the aim of this
experimental work to produce matching average grain size across all alloy classes; thus it
is expected there is error in the analysis of the solid solution strengthening.

In Figure 4.63 the yield asymmetry is examined for the three alloy classes. In the Mg-
Gd alloys, increasing solute content results in a decreasing asymetry between tension and
compression. In the highest solute content, 0.74 at% Gd, the compressive yield strength
exceeds that of tension, and results in a negative asymetry. Referencing Figure 4.62, the
slope of the Fleischer relationship for compression exceeds that of the tension relationship,
thus at a highest solute content we would expect this asymmetry to become negative.
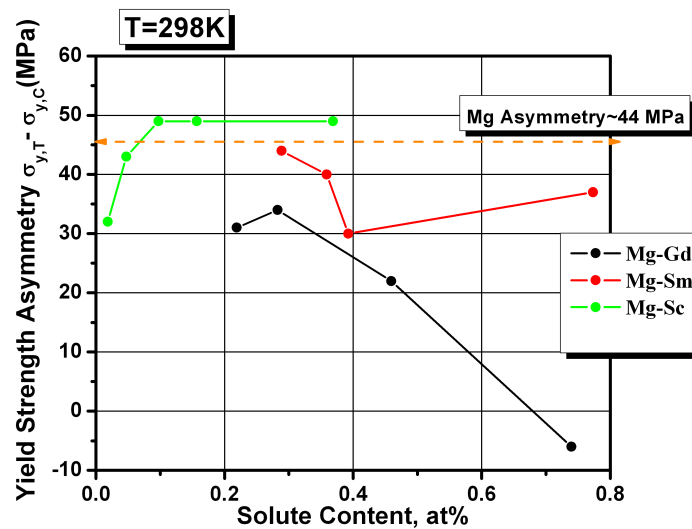

Figure 4.64: Yield Strength Asymmetry vs Concentration for all Alloys

In the Mg-Sm alloys, increasing solute content initially decreases the yield assymetry.
However the asymmetry begins to increase when 0.38 at% Sm is compared to 0.77 at% Sm.

Comparing the slopes of the Hall Petch relationship between tension and compression, the slope is greater in tension, thus with increasing solute content, it would be expected that the asymmetry would get larger. Lastly, in the Mg-Sc system, a rather flat asymmetry is seen, with similar values of strengthening in tension and compression.

4.1.2 Work Hardening

From the work hardening results, Kocks Mecking plots (1981) can be generated to investigate the work hardening trends further. These plots are generated by examing the following relationship:

$$(\sigma - Y)\frac{d\sigma}{d\varepsilon} = (\sigma - Y)[\Theta_h - \Theta_r(\sigma, \dot{\varepsilon}, T)] \tag{4.6}$$

To complete this analysis, $\frac{d\sigma}{d\varepsilon}$ generated in the Results section, is multiplied by effective stress, $(\sigma - Y)$, to represent the plastic portion of the flow stress. Plotting $(\sigma - Y)\frac{d\sigma}{d\varepsilon}$ versus $(\sigma - Y)$, will allow us to evaluate the slope, which will uncover information regarding the dislocation storage, Θ_h, and the point at which dynamic recovery, Θ_r, dominates. In the Kocks - Mecking plots, linear regions correspond to areas in which constant work hardening is observed. Cáceres and Lukáč (2008) completed this analysis for pure magnesium, and we can use the same approach to analyze the work-hardening behaviour of Mg-RE alloys obtained here. For polycrystals of magnesium, Θ_h average values of 1.4 GPa, 2.8 GPa and 3.6 GPa represent basal-basal, basal-prismatic, and basal-pyramidal dislocation interactions respectively(Cáceres and Lukáč, 2008, p.984). Following the same conventions as reported in the Results section, in compression, "Stage A" hardening represents the initial stage of the deformation, and "Stage B" represents the increase in hardening after the initial deformation. In tension, "Stage A" represents the initial stage of deformation, and "Stage

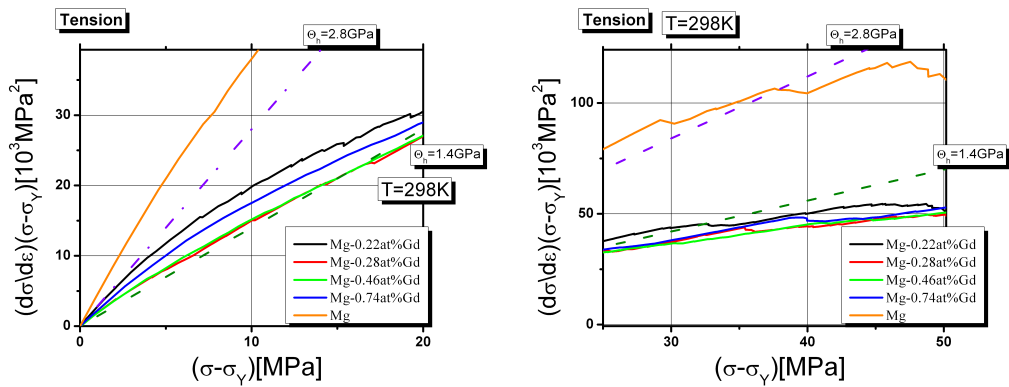B" represents the decrease in hardening after the initial deformation.

For Mg-Gd, in tension (Figure 4.65), the Kocks - Mecking plots depict much decreased work hardening capacity relative to pure magnesium. The hardening rates in tension, Θ_H, corresponding to the slope of the Kocks Mecking plots, are presented in Table 4.16. If the initial stage of deformation is examined, as shown in Figure 4.65(b), it is seen that in the "Stage A", Θ_H decreases with increasing solute to 0.46 at% Gd, and then increases with increasing solute. Referencing the annealed pole figures in Section 3.4, the highest basal intensity was seen in the 0.46 at% Gd sample, with the intensity focused at the centre of the pole figure. This would suggest that strong basal texture, with (0001) basal planes aligned perpendicular to the tensile axis, stabilizes a much softer deformation mechanism than in samples with a more random orientation. Evaluating the "Stage B" deformation, in which there is a decrease of hardening rate, it can be seen that increasing solute content decreases the hardening value, Θ_H. All hardening rates are close to the 1.4 GPa Θ_H value reported by Cáceres and Lukáč (2008), or lower, corresponding to basal-basal dislocation interactions.

Table 4.16: Hardening Rate for Mg-Gd Alloys in Tension

Composition (at%)	"Stage A" Θ_H (GPa)	"Stage B" Θ_H (GPa)
Mg	3.3	3.0
0.22	2.34	1.50
0.28	1.76	1.24
0.46	1.52	0.99
0.74	1.81	0.92
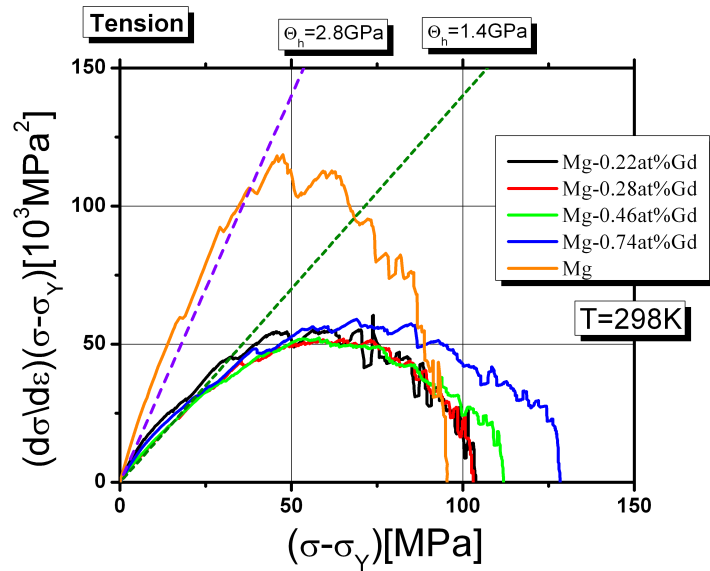
(a) Tensile Kocks Mecking Analysis for Mg-Gd

(b) "Stage A" Kocks Mecking Analysis for Mg-Gd

(c) "Stage B" Kocks Mecking Analysis for Mg-Gd

Figure 4.65: Kocks - Mecking Analysis of Mg-Gd Alloys under tension

For Mg-Gd, in compression (Figure 4.66), the Kocks - Mecking plots depict much decreased work hardening capacity relative to magnesium. The hardening rates in compression, Θ_H, corresponding to the slope of the Kocks Mecking plots, are presented in Table 4.17. If the initial stage of deformation is examined, as shown in Figure 4.66(b), with increasing solute the "Stage A" Θ_H increases with increasing solute. Referencing the annealed pole figures, Figure 3.52, the increasing hardening rate can be correlated to the increased "randomness" of the pole figures with increasing solute. Evaluating the "Stage B" deformation, in which there is an increased hardening rate compared to "Stage A", it can be seen that increasing solute content decreases the hardening value, Θ_H. The exception to this being 0.28 at% Gd, in which the strong texture away from the pole figure normal may impact the hardening rate. All hardening rates approach the 1.4 GPa Θ_H value reported by Cáceres and Lukáč (2008), or lower, corresponding to basal-basal dislocation interaction.

Table 4.17: Hardening Rate for Mg-Gd Alloys in Compression

Composition (wt%)	"Stage A" Θ_H (GPa)	"Stage B" Θ_H (GPa)
Mg	0.6	2.4
0.22	0.47	1.60
0.28	0.65	1.67
0.46	0.65	1.43
0.74	0.75	1.31

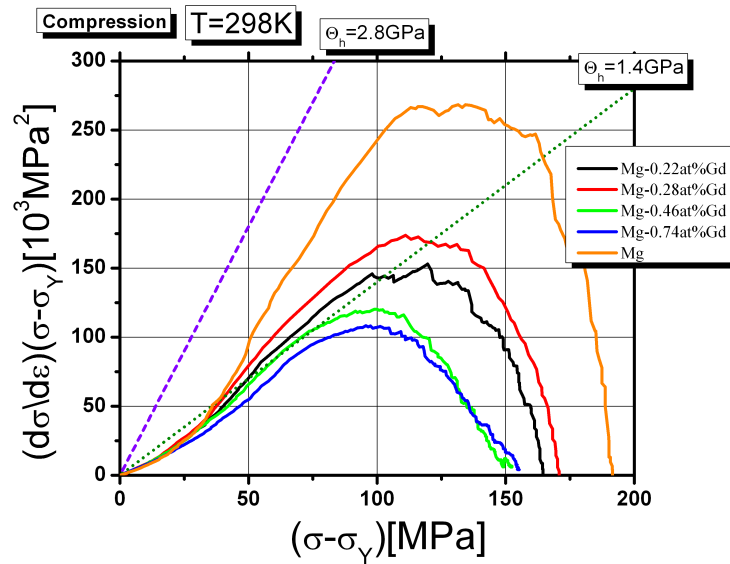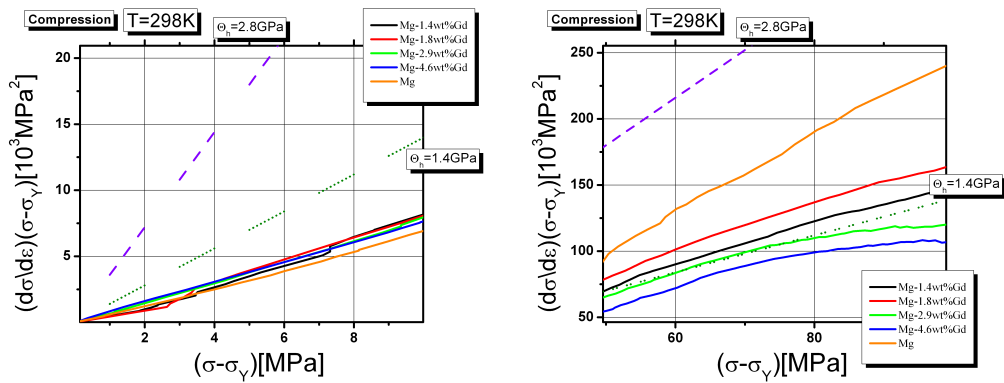(a) Compressive Kocks Mecking Analysis for Mg-Gd

(b) "Stage A" Kocks Mecking Analysis for Mg-Gd

(c) "Stage B" Kocks Mecking Analysis for Mg-Gd

Figure 4.66: Kocks - Mecking Analysis of Mg-Gd Alloys under compression

Comparing the hardening in tension and compression, the difference between the tension and compression plateau is approximately 100 GPa in the lowest concentration alloy (0.22 at%), and approximately 50 GPa in the highest concentration alloy (0.74 at%). Additionally, the effective stress level at which work hardening is zero between tension and compression decreases with increasing solute. Thus, with increasing gadolinium in magnesium, the difference in the work hardening capacity asymmetry decreases.

(a) 0.22at% Gd

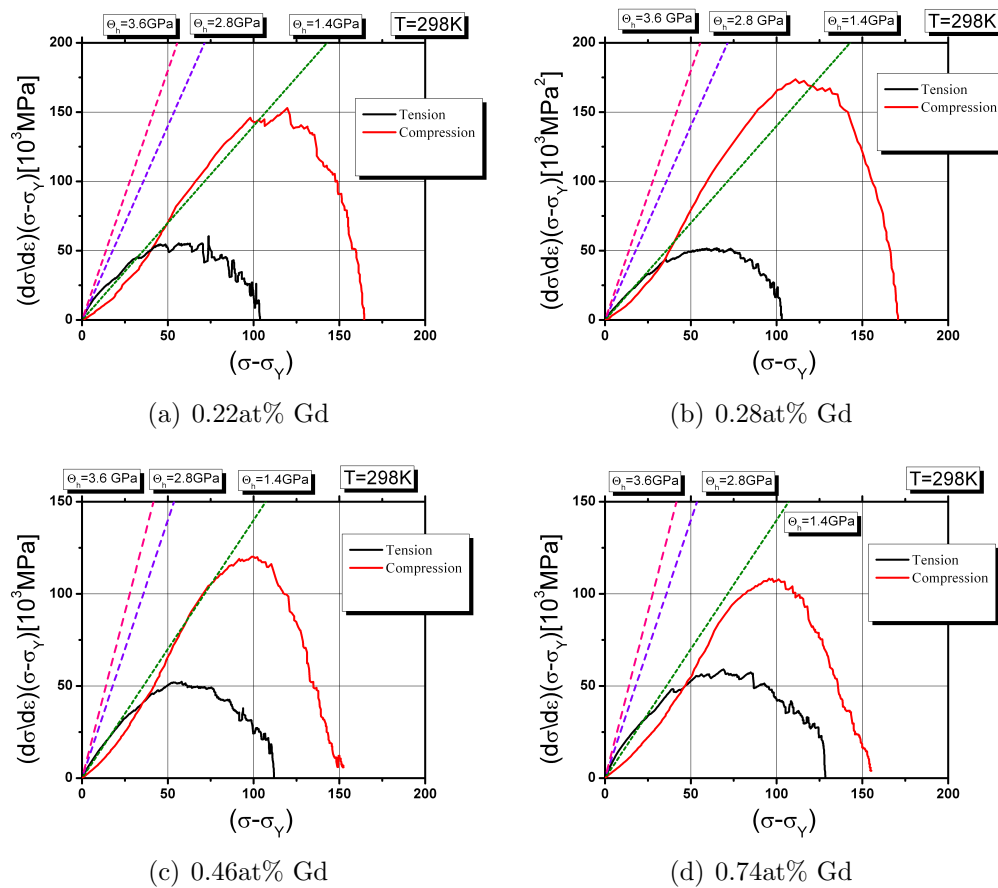(b) 0.28at% Gd

(c) 0.46at% Gd

(d) 0.74at% Gd

Figure 4.67: Comparison of Tension and Compression Work Hardening for Mg-Gd alloys
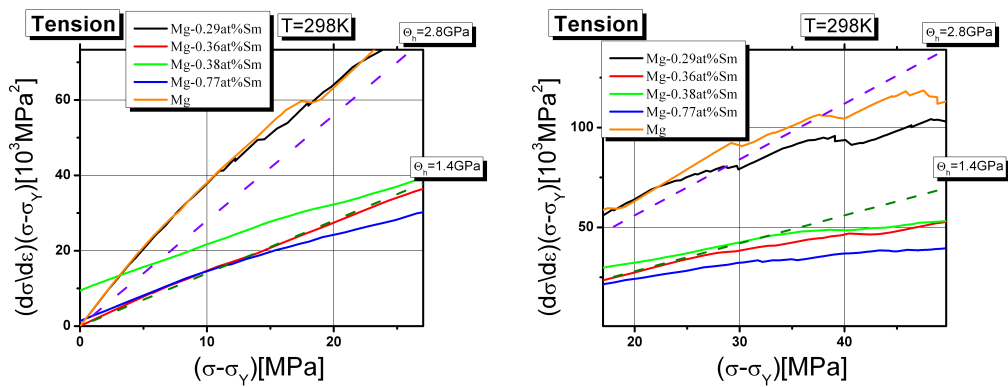
For Mg-Sm, in tension (Figure 4.68), the Kocks - Mecking plots depict much decreased work hardening capacity relative to magnesium, with the exception of 0.29 at% Sm. The hardening rates in tension, Θ_H, corresponding to the slope of the Kocks Mecking plots, are presented in Table 4.18. If the initial stage of deformation is examined, as shown in Figure 4.68(b), with increasing solute the hardening rate decreases. Referencing the annealed pole figures, Figure 3.55, it would suggest that the orientation and the strength of the intensity of diffraction peaks both impact the initial hardening rate. Mg-0.77 at% Sm has a slightly lower "Stage A" Θ_H value than Mg-0.36 at% Sm, and this could be attributed to the stronger initial basal texture in normal direction (ND), as seen in Figure 3.55(c) and Figure 3.55(d). Thus, the data suggest that basal texture along (ND), decreases the initial hardening rate. However weak random texture as seen in Mg-0.38 at% Sm in Figure 3.55(c) provides the lowest initial hardening rate. Evaluating the "Stage B" deformation, in which a decrease of hardening rate is observed, it can be seen that increasing solute content decreases the hardening value, Θ_H. All hardening rates are close to the 1.4 GPa, Θ_H value reported by Cáceres and Lukáč (2008), with the exception of Mg-0.29 at% Sm. The hardening rates of compositions above 0.29 at% Sm correspond to basal-basal dislocation interactions, whereas the hardening rate shown by Mg-0.29 at% Sm corresponds to basal-prismatic dislocation interactions.

Table 4.18: Hardening Rate for Mg-Sm Alloys in Tension

| Composition (at%)	"Stage A" Θ_H (GPa)	"Stage B" Θ_H (GPa)
Mg	3.3	3.0
0.29	3.3	2.80
0.36	1.40	1.37
0.38	1.26	0.98
0.77	1.37	0.89
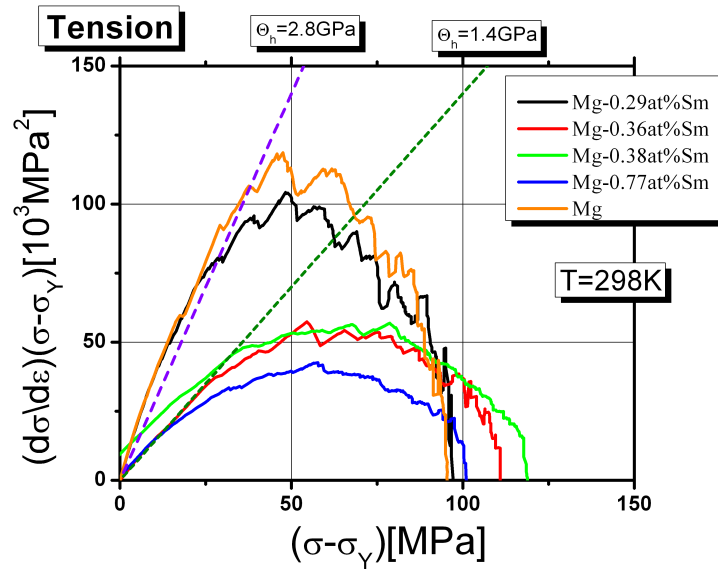
(a) Tensile Kocks Mecking Analysis for Mg-Sm

(b) "Stage A" Kocks Mecking Analysis for Mg-Sm

(c) "Stage B" Kocks Mecking Analysis for Mg-Sm

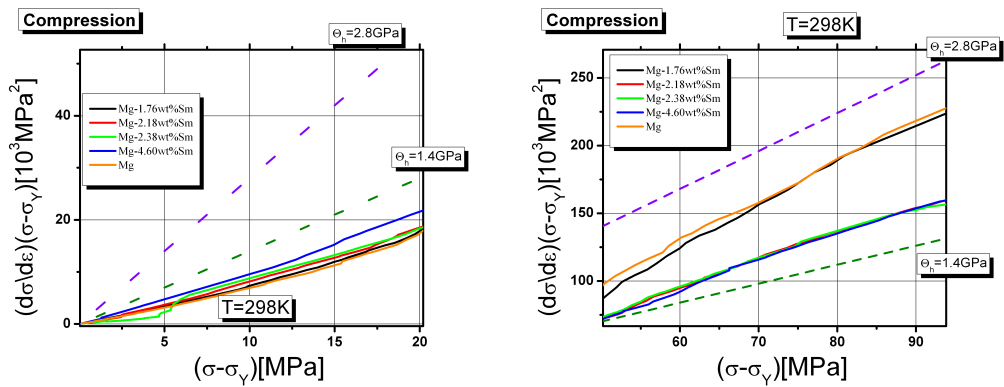Figure 4.68: Kocks - Mecking Analysis of Mg-Sm Alloys under tension

For Mg-Sm, in compression (Figure 4.69), the Kocks Mecking plots depict much decreased work hardening capacity relative to magnesium, with the exception of 0.29 at% Sm. The hardening rates in compression, Θ_H, corresponding to the slope of the Kocks - Mecking plots, are presented in Table 4.19. If the initial stage of deformation is examined, as shown in Figure 4.69(b), with increasing solute the initial hardening rate increases. Referencing the annealed pole figures, Figure 3.55, it would suggest that the increasing randomness of the texture with increasing solute, increases the initial hardening rate. Evaluating the "Stage B" deformation, in which there is an increased hardening rate compared to "Stage A", it can be seen that increasing solute content decreases the hardening value, Θ_H; however the rate decrease is minimal. The hardening value stabilizes around 1.7 GPa which is larger than the 1.4 GPa Θ_H value reported by Cáceres and Lukáč (2008), corresponding to basal-basal dislocation interactions.

Table 4.19: Hardening Rate for Mg-Sm Alloys in Compression

Composition (at%)	"Stage A" Θ_H (GPa)	"Stage B" Θ_H (GPa)
Mg	0.6	2.4
0.29	0.64	2.40
0.36	0.55	1.78
0.38	0.88	1.72
0.77	0.95	1.74
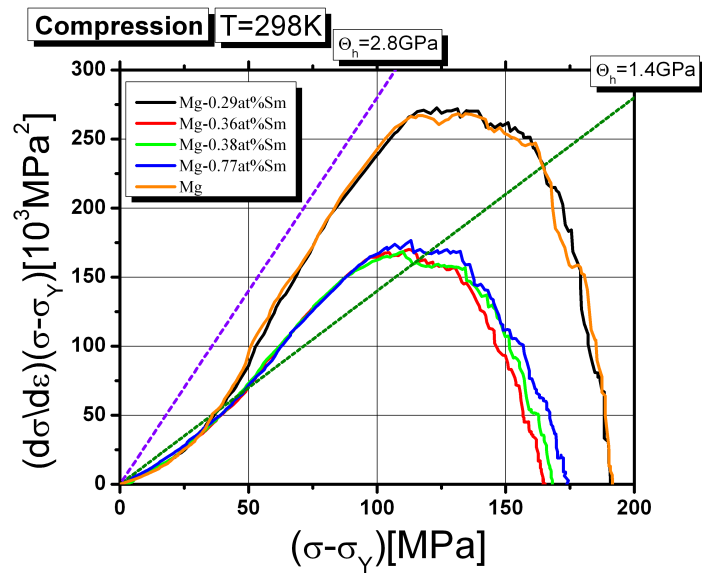
(a) Compressive Kocks Mecking Analysis for Mg-Sm

(b) "Stage A" Kocks Mecking Analysis for Mg-Sm

(c) "Stage B" Kocks Mecking Analysis for Mg-Sm

Figure 4.69: Kocks - Mecking Analysis of Mg-Sm Alloys under compression

Comparing the hardening in tension and compression for Mg-Sm alloys, the difference between the tension and compression plateau is approximately 150 GPa in the lowest concentration alloy (0.29 at%), which then stabilizes at 100 GPa for all other compositions. Additionally, the effective stress level at which work hardening is zero between tension and compression follows a similar trend, as the difference is 100 MPa for 0.29 at%, and 50 MPa for all other compositions. Thus, increasing samarium in magnesium is ineffective at reducing the work hardening asymmetry.

(a) 0.29at% Sm
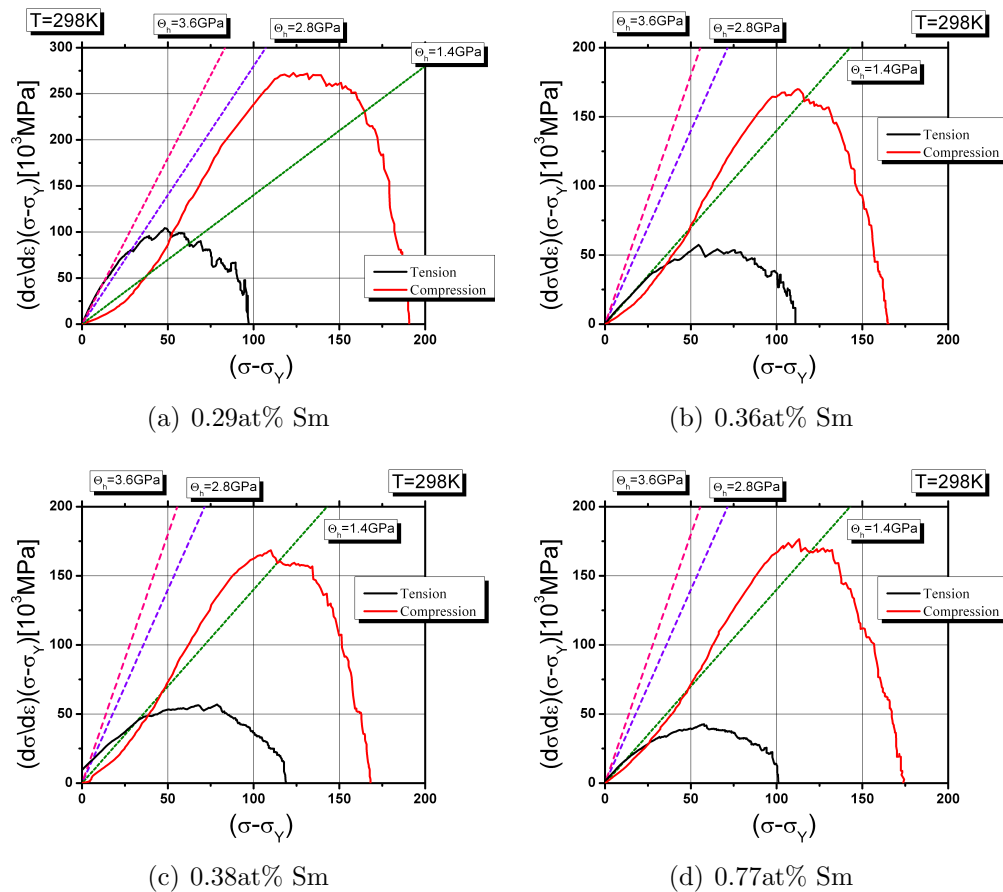
(b) 0.36at% Sm

(c) 0.38at% Sm

(d) 0.77at% Sm

Figure 4.70: Comparison of Tension and Compression Work Hardening for Mg-Sm
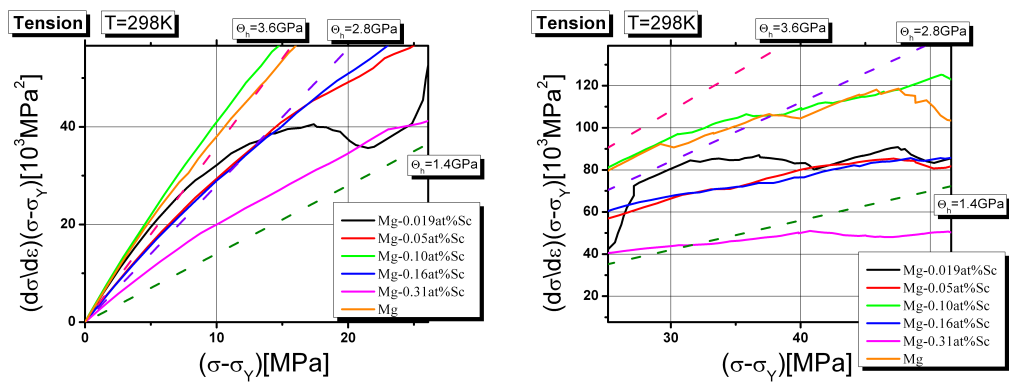
For Mg-Sc, in tension (Figure 4.71), the Kocks Mecking plots depict similar work hardening capacity to that of magnesium. The hardening rates in tension, Θ_H, corresponding to the slope of the Kocks Mecking plots, are presented in Table 4.20. If the initial stage of deformation is examined in depth, as shown in Figure 4.71(b), ignoring the low level solute alloys (0.019 at% and 0.05 at% Sc), with increasing solute one observes decreasing hardening rate. Referencing the annealed pole figures, Figure 3.58, one observes that with increasing solute the orientation spreads away from normal direction (ND) outwards. Comparing 0.10 at% Sc to 0.16 at% Sc, the annealed 0.16 at% Sc pole figure has maximum intensity along (ND), and the texture strength is much greater than in the 0.10 at% Sc alloy. As seen in the other binary classes, the basal intensity along (ND) leads to decreased "Stage A" hardening rate. Evaluating the "Stage B" deformation, it can be seen that increasing solute content decreases the hardening value, Θ_H. The hardening rates of 0.10 at% Sc and 0.16 at% Sc exceed the 1.4 GPa Θ_H value reported by Cáceres and Lukáč (2008) with the exception of 0.31 at% Sc which is at the level of 1.3 GPa.

Table 4.20: Hardening Rate for Mg-Sc Alloys in Tension

| Composition (at%)	"Stage A"Θ_H (GPa)	"Stage B"Θ_H (GPa)
Mg	3.3	3.0
0.019	4.20	1.63
0.05	2.8	1.81
0.10	3.95	2.27
0.16	2.85	2.17
0.31	2.09	1.30
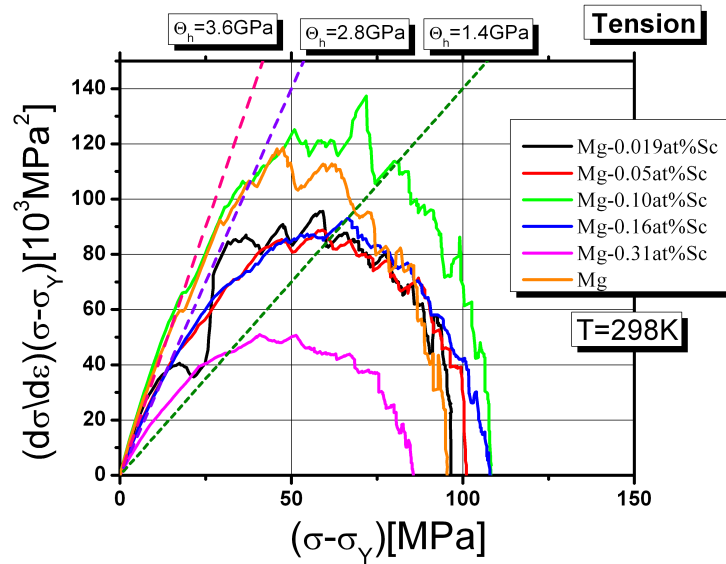
(a) Tensile Kocks Mecking Analysis for Mg-Sc

(b) "Stage A" Kocks Mecking Analysis for Mg-Sc

(c) "Stage B" Kocks Mecking Analysis for Mg-Sc

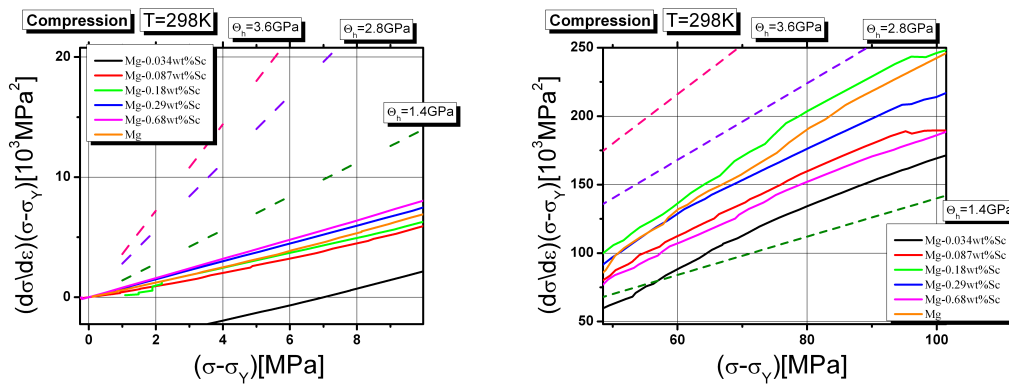Figure 4.71: Kocks - Mecking Analysis of Mg-Sc Alloys under tension

For Mg-Sc, in compression (Figure 4.72), the Kocks Mecking plots depict similar work hardening capacity to that of magnesium. The hardening rates in compression, Θ_H, corresponding to the slope of the Kocks-Mecking plots, are presented in Table 4.21. If the initial stage of deformation is examined, as shown in Figure 4.72(b), one observes that with increasing solute (ignoring 0.019 at% Sc) the initial hardening rate increases. Evaluating the "Stage B" deformation, in which one observes an increased hardening rate compared to "Stage A", it can be seen that increasing solute content decreases the hardening value, Θ_H. The hardening value falls between the 1.4 GPa Θ_H basal-basal dislocation interaction value, and the 2.8 GPa Θ_H basal-prismatic dislocation interaction values reported by Cáceres and Lukáč (2008).

Table 4.21: Hardening Rate for Mg-Sc Alloys in Compression

Composition (at%)	"Stage A" Θ_H (GPa)	"Stage B" Θ_H (GPa)
Mg	0.6	2.4
0.019	0.58	1.90
0.05	0.37	2.1
0.10	0.61	2.8
0.16	0.74	2.54
0.31	0.80	2.01
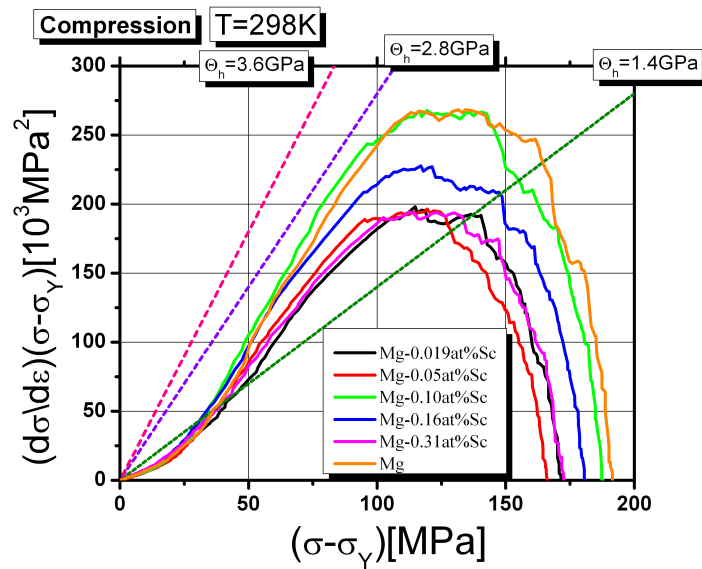
(a) Compressive Kocks Mecking Analysis for Mg-Sc

(b) "Stage A" Kocks Mecking Analysis for Mg-Sc

(c) "Stage B" Kocks Mecking Analysis for Mg-Sc

Figure 4.72: Kocks - Mecking Analysis of Mg-Sc Alloys under compression

Comparing the hardening in tension and compression, the difference between the tension and compression plateau is approximately 100 GPa in the lowest concentration alloy (Mg-0.019 at% Sc), and increases to approximately 150 GPa in the highest concentration alloy (Mg-0.31 at% Sc). Additionally, the effective stress level at which work hardening is zero between tension and compression is relatively constant at 75 MPa for all alloys. Thus, increasing scandium in magnesium increases the work hardening asymmetry between tension and compression.

(a) 0.019at% Sc

(b) 0.05at% Sc

(c) 0.10at% Sc
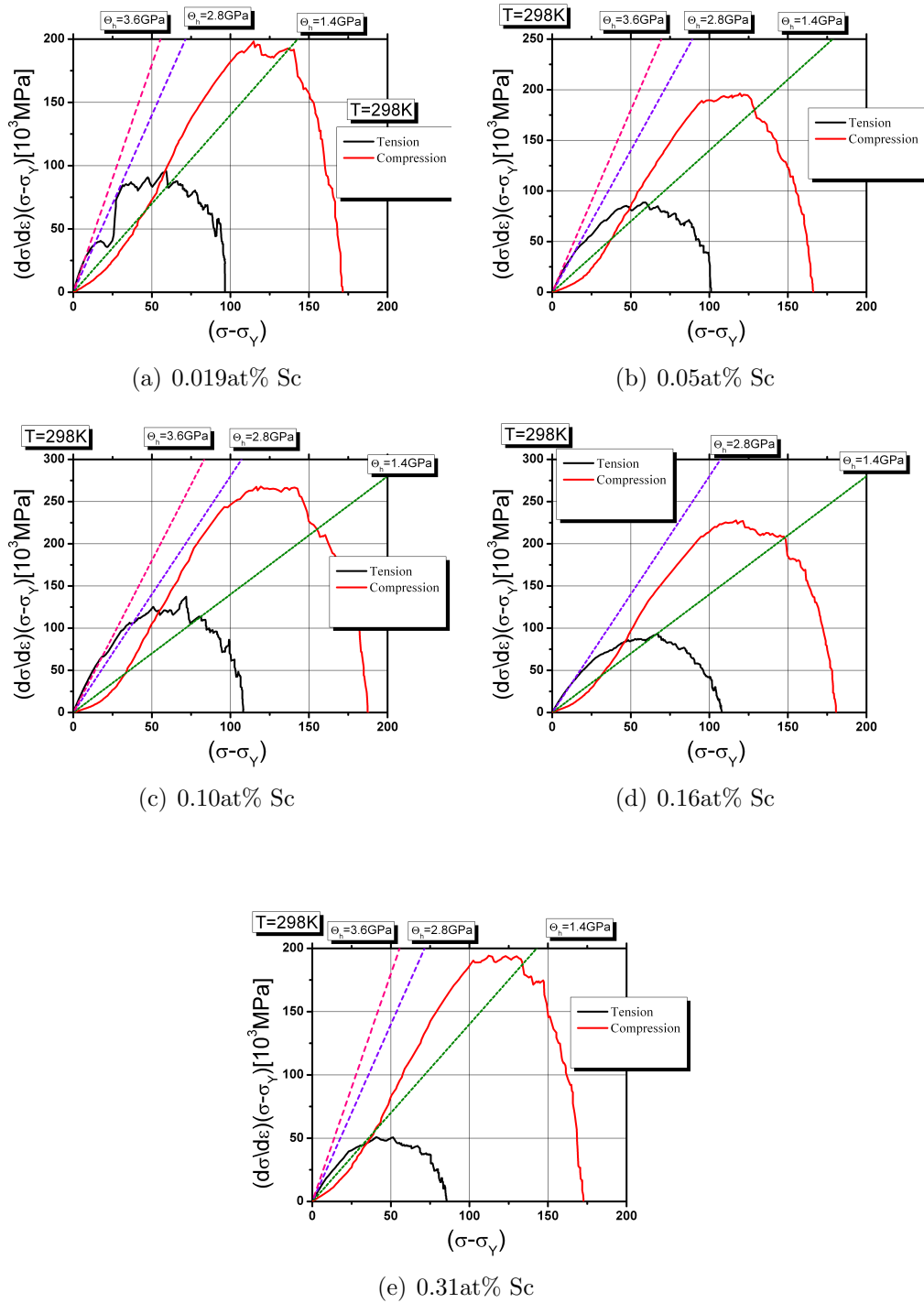
(d) 0.16at% Sc

(e) 0.31at% Sc

Figure 4.73: Comparison of Tension and Compression Work Hardening for Mg-Sm

With the three binary classes of Mg-RE alloys, one of the aims was to produce compositions at similar atomic percent for comparison. With the chaotic nature of the experimental casting, best intentions did not meet that desired objective for all compositions. However there was one composition at which there was matching atomic percent for each binary class. At 0.3 at%, which corresponds to 1.8 wt% Gd, 1.76 wt% Sm, and 0.68 wt% Sc, we can compare the initial and final textures of the samples, to the observed work hardening behaviour. The Kocks - Mecking plot is presented in Figure 4.74. Following the same analysis as in the previous section, the Kocks - Mecking plots can be compared to that of magnesium, mimicking the analysis performed by Cáceres and Lukáč (2008). The results of the hardening rates in tension and compression from Section 4.1.2 are reported in Tables 4.22- 4.23 for direct comparison.

With knowledge obtained from the Kocks - Mecking analysis of the work hardening behaviour, the annealed, tension and compression textures of the selected alloys can then be compared. The basal pole figures are presented in Figure 4.75. For the "Stage A" hardening in compression, gadolinium and samarium have close to identical hardening values, but these values are less than the 0.8 GPa for scandium. Gadolinium has a randomized texture; whereas samarium is strongly textured, with the maximum intensity of (0002) peaks close to the edges of the pole figure. With the random texture seen in gadolinium the initial deformation could proceed by basal slip, re-orienting the basal poles towards the compression axis. The higher initial "Stage A" Θ_H for scandium could be related to the initial texture and in particular the (0002) intensity of the diffracting peaks shifted towards the centre of the pole figure i.e., ND direction. After "Stage A" has completed, with basal slip re-orientating the basal poles towards the compression axis, and twinning accommodating deformation along the c-axis, there would be significant amount of obstacles placed in the path of mobile dislocations during further deformation. In a polycrystal
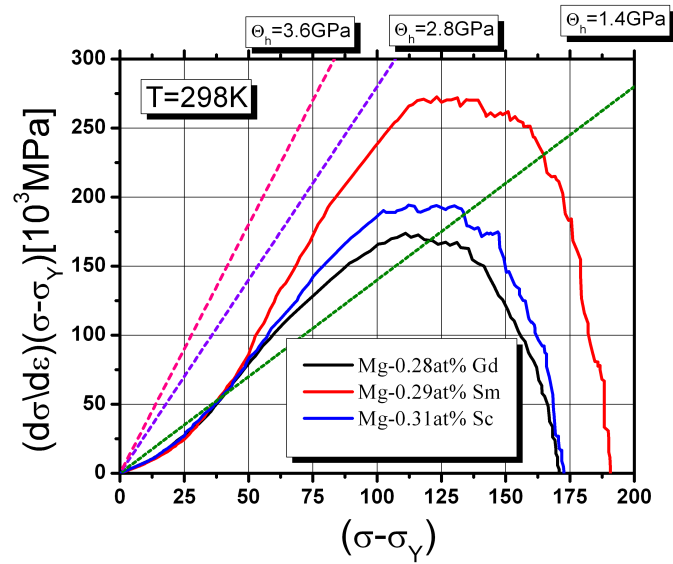
(a) Compression
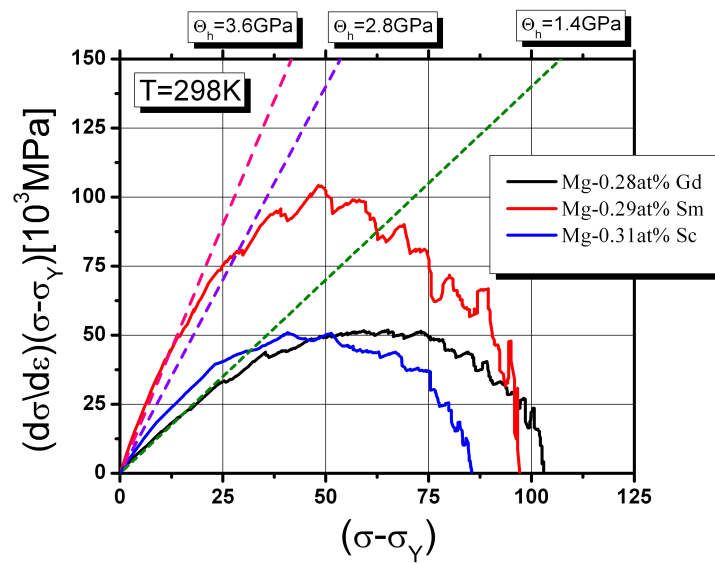
(b) Tension

Figure 4.74: Kocks - Mecking Analysis Across Three Binary Systems at 0.30 at%

with random texture, as seen in the gadolinium sample, twinning would rotate the basal planes away from the compression axis; whereas the grains favourably aligned for basal slip would rotate towards the compression axis. This could promote basal-basal dislocation interactions during initial stage of deformation and would account for the Θ_H slope of $\approx$1.6 GPa, which is very close to the 1.4 GPa value reported by Cáceres and Lukáč (2008) for basal-basal dislocation interactions. Scandium offers a slightly higher hardening rate than gadolinium, and this could be the result of the stronger texture. Finally, the samarium samples exhibits the largest hardening rate of the compared alloys, and this is expected to be a result of the strong initial texture. The strong initial texture located towards the edge of pole figure would allow for relatively easy basal slip initially (as seen with its "Stage A" hardening value), which would rotate the basal poles towards the compression axis. This rotation would lead to a decrease of the Schmid factor for the basal slip, as the basal poles would be moving towards being perpendicular to the compression axis. This incompatibility with basal slip appears to promote prismatic slip. Thus it would be expected that basal dislocations would interact with prismatic dislocations and possibly twinning boundaries. This behaviour can be reflected in the Θ_H value approaching 2.8 GPa, which correlates to prismatic-basal dislocation interactions according to Cáceres and Lukáč (2008). It appears that the deformation by prismatic slip greatly increases the work hardening capacity in compression.

In tension, the basal poles rotate away from the tensile axis; thus at the completion of deformation, we would expect the basal poles not to be aligned parallel to the tensile axis. The differences in the initial texture can be related to the initial hardening rates in tension ("Stage A" Θ_H), which are presented in Table 4.22. Referencing the Θ_H rates published by Cáceres and Lukáč (2008), initially the gadolinium and scandium samples lie between basal-basal and basal-prismatic hardening values. The random orientation in

Table 4.22: Hardening Rate in Compression of Binary Systems at 0.3at%

Binary System	"Stage A" Θ_H (GPa)	"Stage B" Θ_H (GPa)
Mg-Gd	0.65	1.67
Mg-Sm	0.64	2.40
Mg-Sc	0.80	2.01

the gadolinium sample is associated with the lower initial hardening rate than observed in scandium, and the difference could be correlated to the stronger intensity of basal texture in the annealed state. After the initial hardening, there is a significant decrease in the hardening rate, in the range of 1.4 GPa correlating to the basal-basal dislocation interactions. Finally, in samarium, with the strong intensity close the the edges of the pole figure, the basal poles would be already close to perpendicular to the tensile axis, and basal slip would be less favourable than prismatic slip. The hardening value, Θ_H, for samarium of 2.8 GPa represents the prismatic-basal dislocation interactions hardening values as reported by Cáceres and Lukáč (2008).

Table 4.23: Hardening Rate in Tension of Binary Systems at 0.3at%

Binary System	"Stage A" Θ_H (GPa)	"Stage B" Θ_H (GPa)
Mg-Gd	1.76	1.24
Mg-Sm	3.3	2.80
Mg-Sc	2.09	1.30

(a) Mg-0.28at%Gd Annealed   (b) Mg-0.29at%Sm Annealed   (c) Mg-0.31at%Sc Annealed

(d) Mg-0.28at%Gd Compression   (e) Mg-0.29at%Sm Compression   (f) Mg-0.31at%Sc Compression

(g) Mg-0.28at%Gd Tension   (h) Mg-0.29at%Sm Tension   (i) Mg-0.31at%Sc Tension
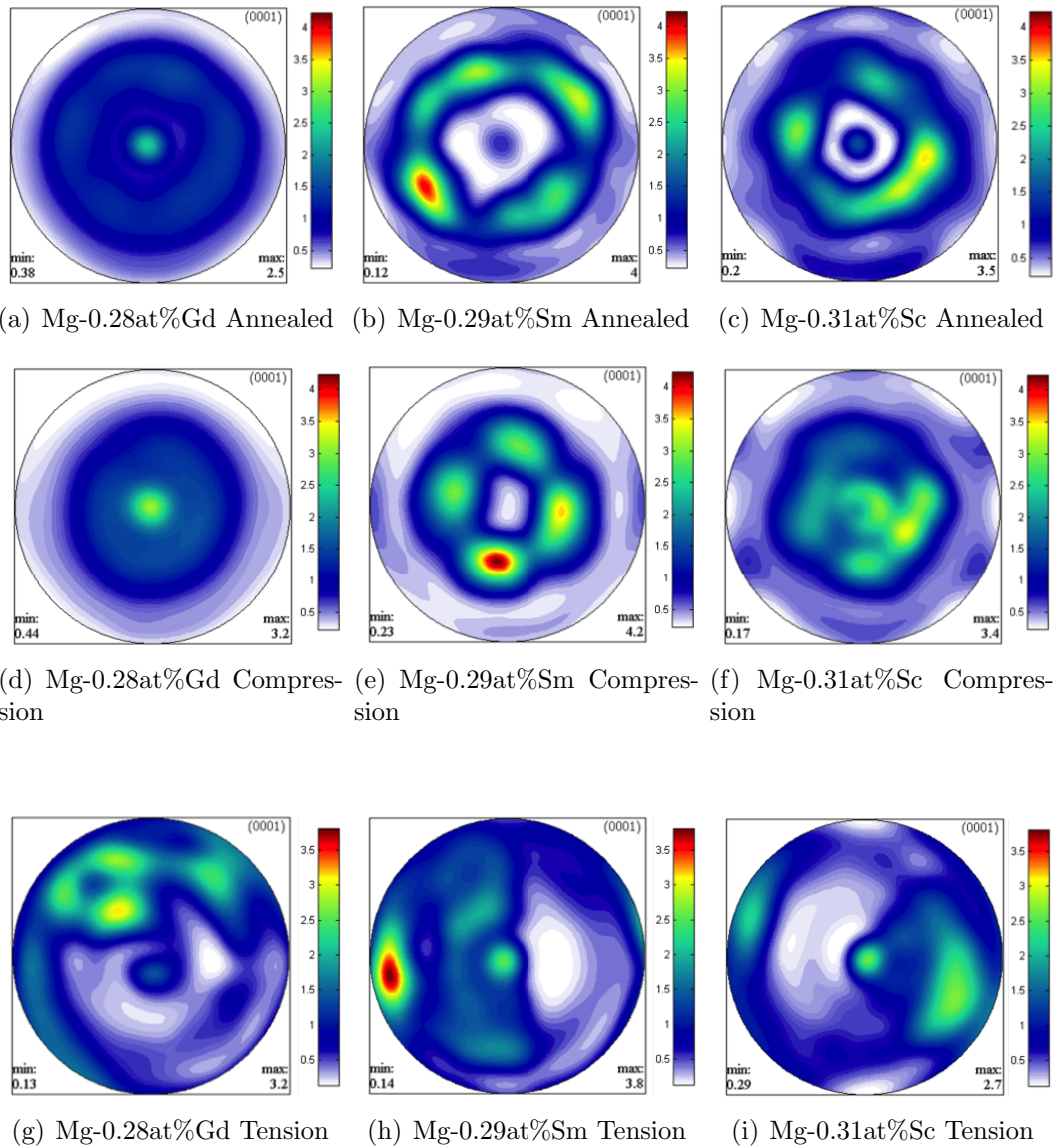
Figure 4.75: Comparison of Basal Pole Figures for Similar Composition Across the Three Binary Alloys.

4.2   Strain Rate Sensitivity

The thermodynamic strain rate sensitivity of a material can be evaluated through the following relationship (Diak *et al.*, 1998):

$$\frac{1}{T}\left(\frac{d\sigma}{d\ln\dot{\varepsilon}}\right)_{\Sigma,T} = \frac{m}{T} = S \tag{4.7}$$

Where S is the thermodynamic strain rate sensitivity. The engineering definition of strain rate sensitivity is defined as m, which can be obtained by dividing by temperature from the values obtained in the Results section. For a polycrystalline material, the following relationship was used to obtain the thermodynamic strain rate sensitivity:

$$\frac{1}{T}\left(\frac{d\sigma}{d\ln\dot{\varepsilon}}\right)_{\Sigma,T} = \frac{1}{T}\left[(\sigma - \sigma_{ys})\,m_d + \sigma_s m_s + \sigma_t m_t\right] \tag{4.8}$$

The measured slope of $\frac{1}{T}\left(\frac{d\sigma}{d\ln\dot{\varepsilon}}\right)_{\Sigma,T}$ versus $(\sigma - \sigma_{ys})$ returns $\frac{m_d}{T}$, which is the thermodynamic strain rate sensitivity S. Looking specificially at the case in which $\sigma = \sigma_{ys}$, the y-intercept greater than zero would mean that solute and other thermally activated species contribute to the strain rate sensitivity of the material, over and above dislocation dislocation interactions (Diak *et al.*, 1998, p.235). From the experiments, the Mg-Sm and Mg-Gd were greatly influenced by solute-dislocation interactions in tension, as all compositions had a positive y-intercept, and the slope of the Haasen plot decreased with increasing solute, and the highest concentrations exhibited a negative strain rate sensitivity. Mg-Gd exhibited the same behaviour in compression. However Mg-Sm showed relatively minor changes in strain rate sensitivity in compression. Correlating this to the Kocks - Mecking plots (Figure 4.69(a)), aside from the 0.29 at% Sm alloy, increasing levels of solute did not alter the point at which dislocation annihilation dominated, and thus the solute atoms play a lesser role than

dislocation-dislocation interactions along the active slip systems engaged via compressive loading. Reviewing the Kocks - Mecking plots in tension (Figures 4.65(a)- 4.68(a)), both binary classes showed basal-basal dislocation interactions, and thus the increasing level of solute would be expected to influence these interactions.

For Mg-Sc, there is a slight decrease in the strain rate sensitivity with increasing solute content, but not in the order of magnitude seen in Mg-Gd and Mg-Sm. Additionally, the y-intercept of the Haasen plots is very close to zero, and thus the dislocation-solute interaction is not as impactful as the dislocation-dislocation interactions. This impact could be due in part to the similar atomic radius of magnesium and scandium (150 pm and 160 pm respectively), as opposed to the much larger atomic radii of gadolinium and samarium ($\approx$180 pm).

Chapter 5

Conclusions

Based on the experimental work completed in this thesis, the following conclusions and observations can be made:

1. For the binary alloys explored, only gadolinium and samarium in compression followed the Labusch theory of solution strengthening; in which the yield strength scales with $c^{\frac{2}{3}}$. At low levels of solute, gadolinium provides the greatest yield strength in both tension and compression relative to samarium and scandium. Conversely, samarium provides the greatest solid solution strengthening rate in both tension and compression relative to gadolinium and scandium.

2. Gadolinium additions provided the largest strain to failure in tension, and the largest maximum true stress in tension. Samarium additions provided the largest maximum true stress in compression.

3. In tension, increased solute content varies the initial hardening level, Θ_0 relative to pure magnesium. Gadolinium additions have a lower Θ_0 value than pure Magnesium for all concentrations, and Θ_0 decreases with increasing solute. Samarium additions,

at the lowest concentration have a Θ_0 value similar to that of pure magnesium, but then drop significantly to levels lower than gadolinium. Finally, scandium additions have much higher Θ_0 values than gadolinium and samarium, that remains rather constant until the highest concentration alloy. This lower Θ_0 value for the gadolinium and samarium could help to explain the increase strain to failure of these alloys in tension compared to pure Magnesium.

4. At the highest level of solute, both Mg-Gd and Mg-Sm exhibit negative strain rate sensitivity in tension. Both binary classes have decreasing strain rate sensitivity with increasing solute levels, and combined with the Kocks - Mecking plots, it can be assumed that the solute atoms influence the basal-basal dislocation interactions.

5. The asymmetry between tension and compression is only decreased in Mg-Gd binary system with increasing solute. With increasing solute in Mg-Sm, the asymmetry becomes larger due to greater strengthening in tension than in compression. The Mg-Sc binary system does not see any impact on yield asymmetry with increasing solute.

6. The combination of both texture and strain rate sensitivity is used to explain the differences in work hardening behaviour seen across the binary systems, although crystallographic orientation seems to have a much greater effect on the work hardening capacity than strain rate sensitivity.

7. Samarium and gadolinium both exhibit decreasing strain rate sensitivity with increasing solute in both tension and compression, that can lead to negative SRS at the highest solute level. However this behaviour is not seen in scandium, which could be due in part to the small atomic radius, which is similar to the atomic radius of

magnesium.

8. Based on results obtained it can be concluded that the asymmetry in work hardening behaviour and the form of the flow curves between tension and compression is the result of the difference in the dominating modes of deformation at a given stage of the plastic flow. The corresponding dislocation-obstacles interactions control the work hardening and the work-hardening levels provide a fingerprint of the dominant interactions. The present thesis allowed to establish the hardening levels characteristic of these interactions in Mg-RE alloys considered.

Bibliography

Ball, E. and Prangnell, B. (1994). Tensile - compressive yield asymmetries in high strength wrought magnesium alloys. *Scripta Metallurgica et Materialia*, **31**(2), 111–116.

Barnett, M. (2007a). Twinning and the ductility of magnesium alloys: Part i: "tension twins". *Materials Science and Engineering: A*, **464**(1-2), 1 – 7.

Barnett, M. R. (2007b). Twinning and the ductility of magnesium alloys: Part ii. "contraction" twins. *Materials Science and Engineering: A*, **464**(1-2), 8–16.

Blake, A. H. and Cáceres, C. H. (2008). Solid-solution hardening and softening in mg–zn alloys. *Materials Science and Engineering: A*, **483-484**(0), 161–163.

Bohlen, J., Nürnberg, M. R., Senn, J. W., Letzig, D., and Agnew, S. R. (2007). The texture and anisotropy of magnesium-zinc-rare earth alloy sheets. *Acta Materialia*, **55**(6), 2101 – 2112.

Cáceres, C. and Lukáč, P. (2008). Strain hardening behaviour and the taylor factor of pure magnesium. *Philosophical Magazine*, **88**(7), 977–989.

Chun, Y. B. and Davies, C. H. J. (2011). Twinning-induced negative strain rate sensitivity in wrought mg alloy az31. *Materials Science and Engineering: A*, **528**(18), 5713–5722.

Clausen, B., Tomé, C. N., Brown, D. W., and Agnew, S. R. (2008). Reorientation and stress relaxation due to twinning: Modeling and experimental characterization for mg. *Acta Materialia*, **56**(11), 2456–2468.

Czerwinski, F. (2008). *Magnesium Injection Moulding*. Springer Science+Business Media, LLC.

Diak, B. J., Upadhyaya, K. R., and Saimoto, S. (1998). Characterization of thermodynamic response by materials testing. *Progress in Materials Science*, **43**(4), 223–363.

Gao, L., Chen, R. S., and Han, E. H. (2009). Effects of rare-earth elements gd and y on the solid solution strengthening of mg alloys. *Journal of Alloys and Compounds*, **481**(1-2), 379–384.

Hantzsche, K., Wendt, J., Kainer, K., Bohlen, J., and Letzig, D. (2009). Mg sheet: the effect of process parameters and alloy composition on texture and mechanical properties. *JOM Journal of the Minerals, Metals and Materials Society*, **61**, 38–42. 10.1007/s11837-009-0119-2.

Hauser, F., Landon, P., and Dorn, J. (1956). Fracture of magnesium alloys at low temperature. *Transactions AIME, Journal of Metals*, **206**, 589–593.

Hiura, F. (2010). *Latent Hardening in Magnesium Single Crystals*. Master's thesis, McMaster University.

Leontis, T. E. (1951). Effect of rare-earth metals on the properties of extruded magnesium. *Transactions AIME, Journal of Metals*, **191**, 987–993.

McDonald, J. C. (1940). Tensile properties of rolled magnesium alloys-binary alloys with

calcium, cerium, gallium, and thorium. *Transactions of the Metallurgical Society of AIME*, **143**, 179–182.

Mecking, H. and Kocks, U. F. (1981). Kinetics of flow and strain-hardening. *Acta Metallurgica*, **29**(11), 1865–1875.

Mordike, B. L. (2001). Development of highly creep resistant magnesium alloys. *Journal of Materials Processing Technology*, **117**(3), 391 – 394.

Muránsky, O., Barnett, M. R., Luzin, V., and Vogel, S. (2010). On the correlation between deformation twinning and lüders-like deformation in an extruded mg alloy: In situ neutron diffraction and epsc.4 modelling. *Materials Science and Engineering: A*, **527**(6), 1383–1394.

Pisch, A., Schmid-Fetzer, R., Cacciamani, G., Riani, P., Saccone, A., and Ferro, R. (1998). Mg-rich phase equilibria and thermodynamic assessment of the mg-sc system. *Zeitschrift Für Metallkunde*, **89**(7).

Rokhlin, L. (1998). Dependence of the rare earth metal solubility in solid magnesium on its atomic number. *Journal of Phase Equilibria*, **19**, 142–145. 10.1361/105497198770342607.

Rokhlin, L. (2003). *Magnesium alloys containing rare earth metals: structures and properties*. Taylor & Francis.

Rokhlin, L. (2006). Structure and properties of alloys of the mg-rem system. *Metal Science and Heat Treatment*, **48**, 487–490. 10.1007/s11041-006-0122-y.

Safi-Naqvi, S. H., Hutchinson, W. B., and Barnett, M. R. (2008). Texture and mechanical anisotropy in three extruded magnesium alloys. *Materials Science and Technology*, **24**(10), 1283–1292.

Senn, J. W. and Agnew, S. (2008). Texture randomization of magnesium alloys containing rare earth elements. *Magnesium Technology*, pages 153–158.

Stanford, N. and Barnett, M. R. (2008). The origin of "rare earth" texture development in extruded mg-based alloys and its effect on tensile ductility. *Materials Science and Engineering: A*, **496**(1-2), 399–408.

Stanford, N., Atwell, D., Beer, A., Davies, C., and Barnett, M. (2008). Effect of microalloying with rare-earth elements on the texture of extruded magnesium-based alloys. *Scripta Materialia*, **59**(7), 772 – 775.

Stanford, N., Sabirov, I., Sha, G., La Fontaine, A., Ringer, S., and Barnett, M. (2010a). Effect of al and gd solutes on the strain rate sensitivity of magnesium alloys. *Metallurgical and Materials Transactions A*, **41**, 734–743. 10.1007/s11661-009-0107-8.

Stanford, N., Atwell, D., and Barnett, M. R. (2010b). The effect of gd on the recrystallisation, texture and deformation behaviour of magnesium-based alloys. *Acta Materialia*, **58**(20), 6773–6783.

Wang, S. C., Zhu, Z., and Starink, M. J. (2005). Estimation of dislocation densities in cold rolled al-mg-cu-mn alloys by combination of yield strength data, ebsd and strength models. *Journal of Microscopy*, **217**(2), 174–178.

Chapter 6

Appendix

6.1   Haasen Plots for Individual Alloys
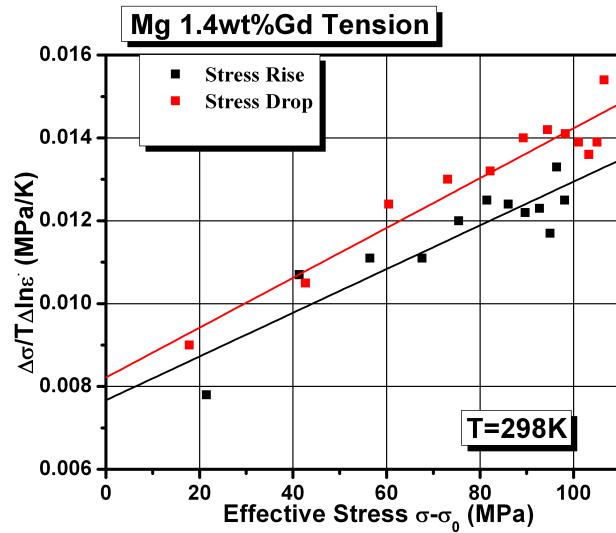
(a) Tension Haasen Plot for Mg-0.22 at% Gd
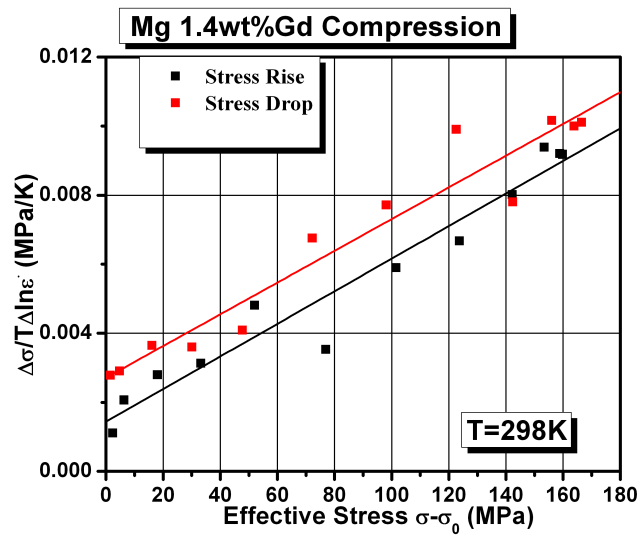
(b) Compression Haasen Plot for Mg-0.22 at% Gd

Figure 6.76: Haasen Plot for Mg-0.22 at%Gd
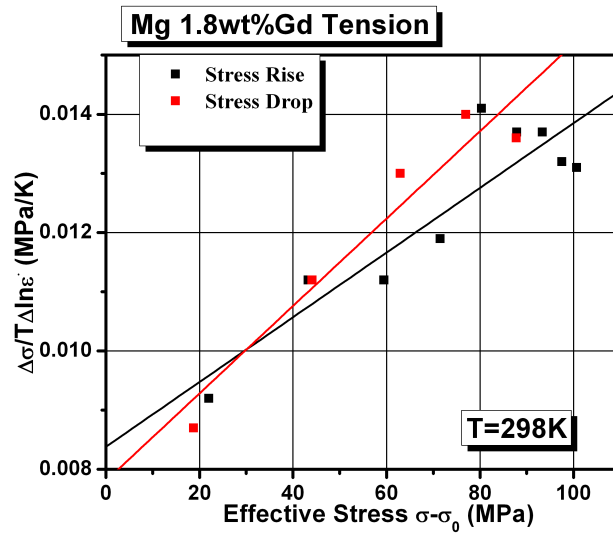
(a) Tension Haasen Plot for Mg-0.28 at% Gd
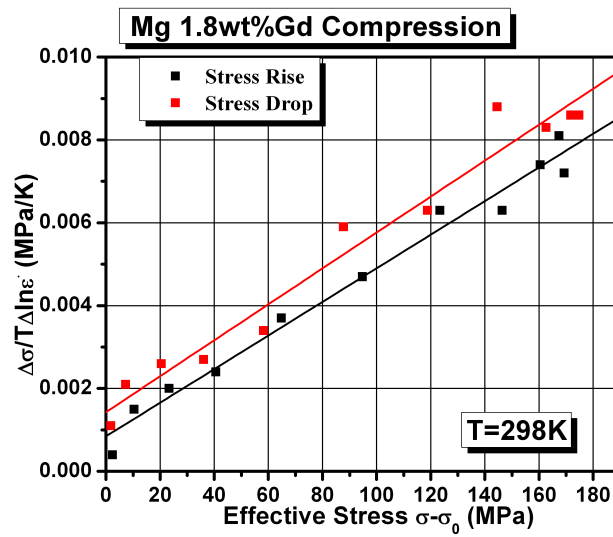
(b) Compression Haasen Plot for Mg-0.28 at% Gd
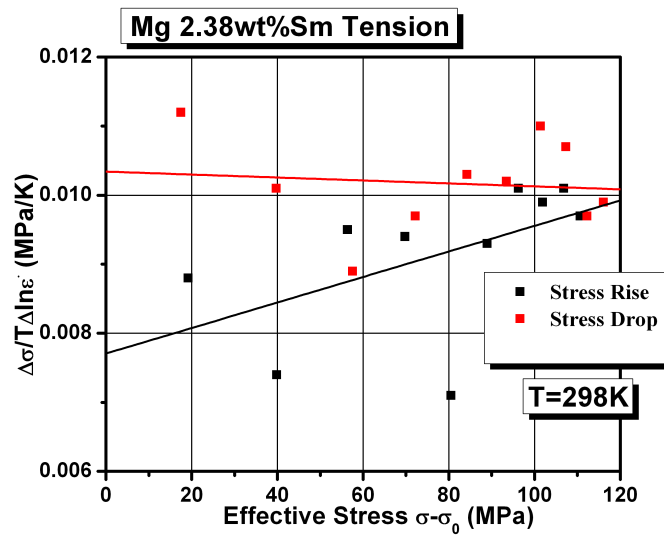
Figure 6.77: Haasen Plot for Mg-0.28 at% Gd
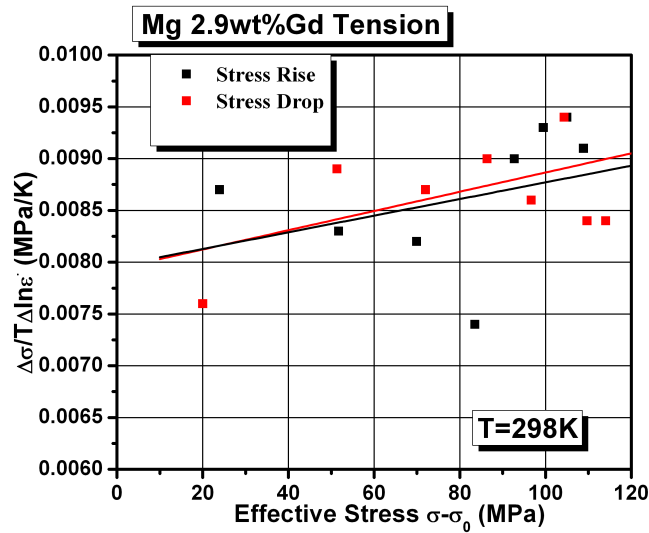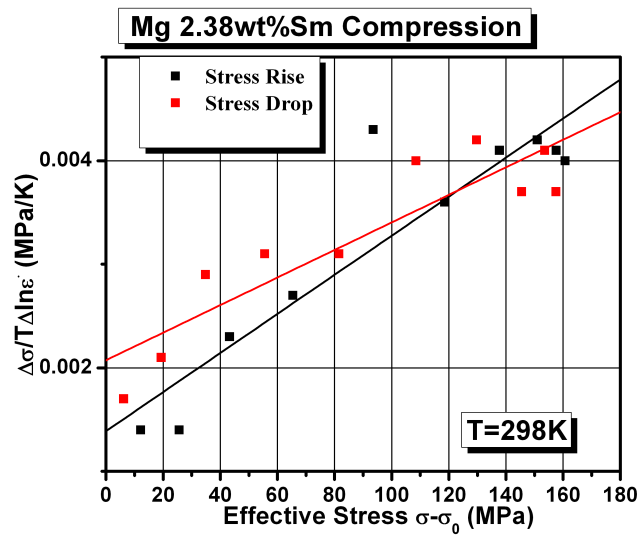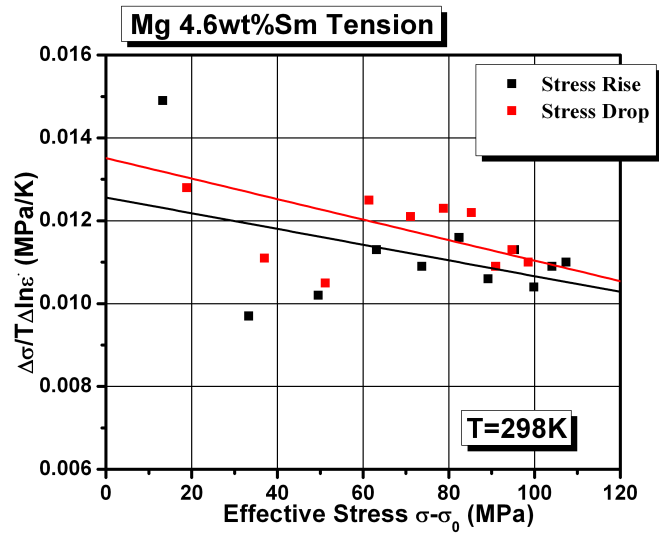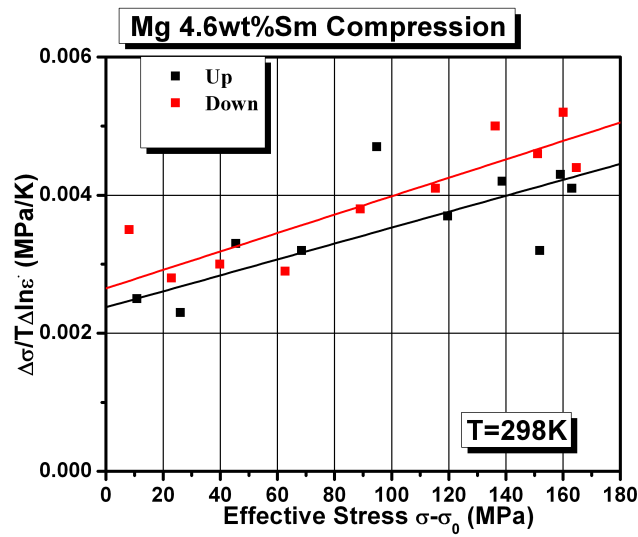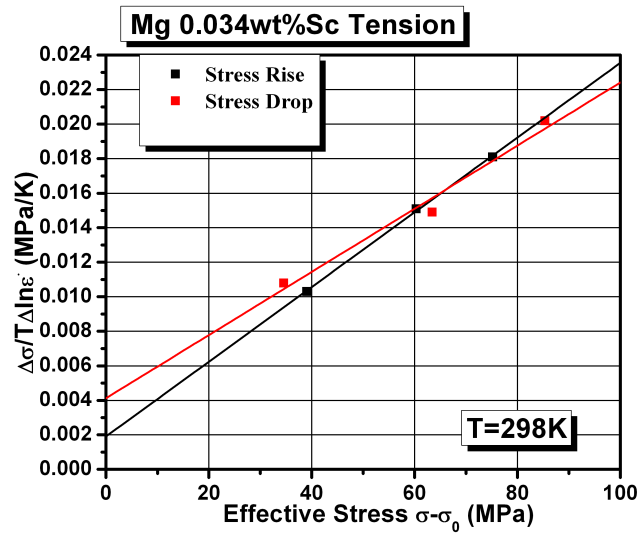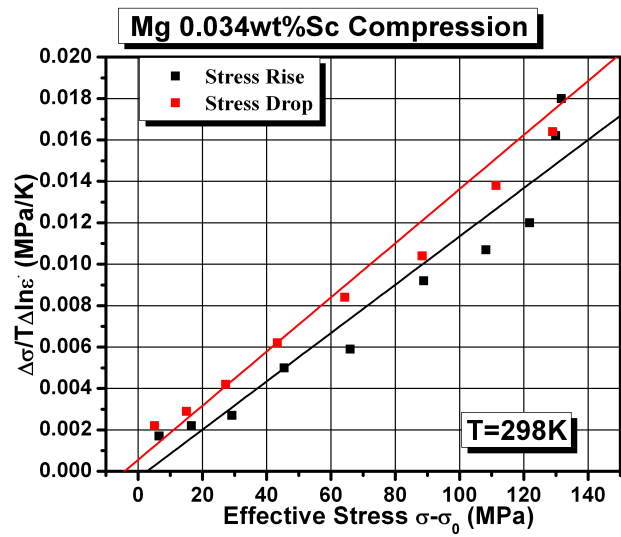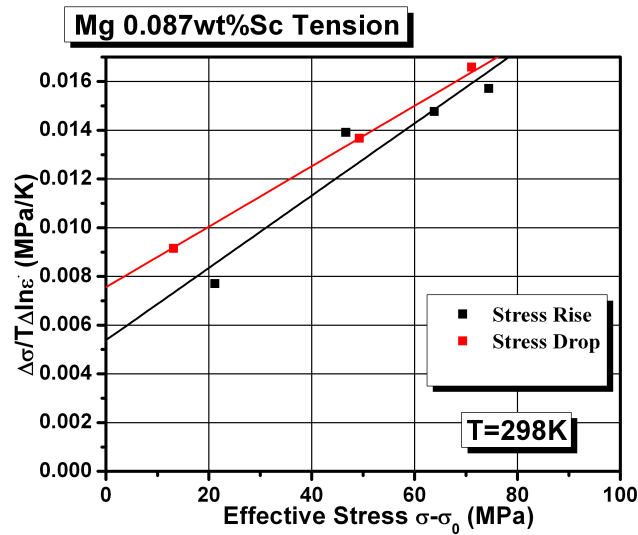
(a) Tension Haasen Plot for Mg-0.46 at% Gd
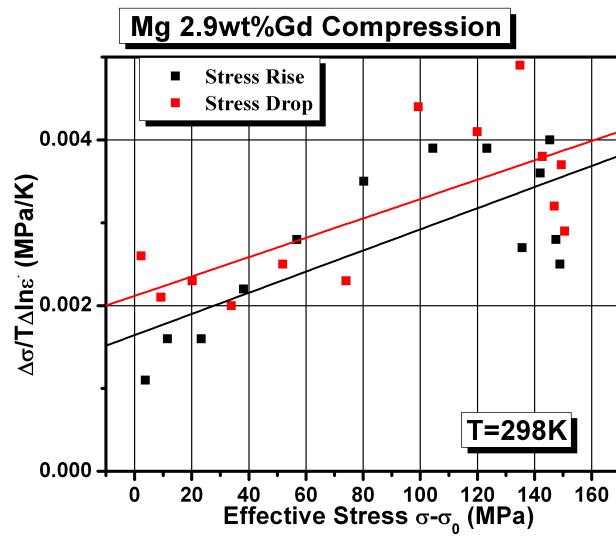
(b) Compression Haasen Plot for Mg-0.46 at% Gd

Figure 6.78: Haasen Plot for Mg-0.46 at% Gd
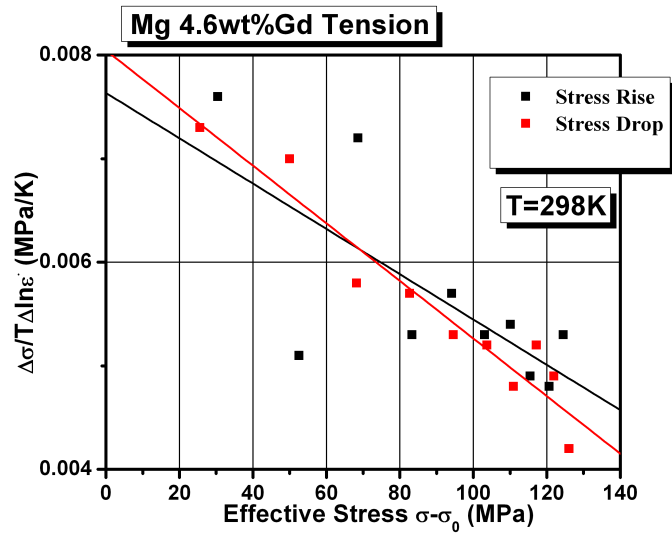
(a) Tension Haasen Plot for Mg-0.77 at% Gd
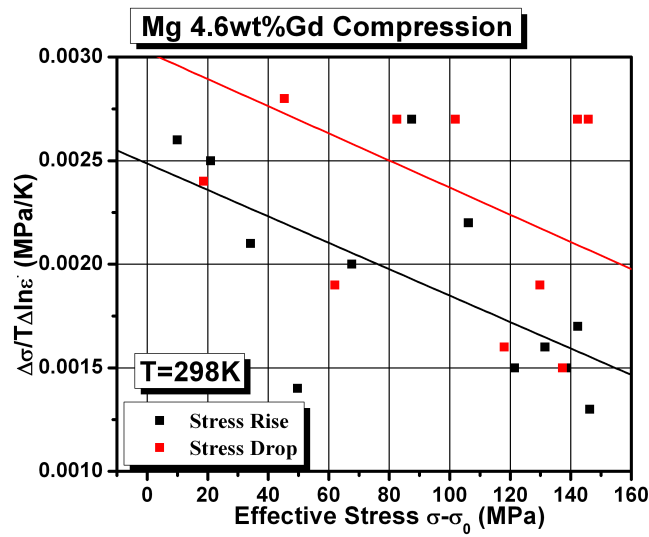
(b) Compression Haasen Plot for Mg-0.77 at% Gd

Figure 6.79: Haasen Plot for Mg-0.77 at% Gd
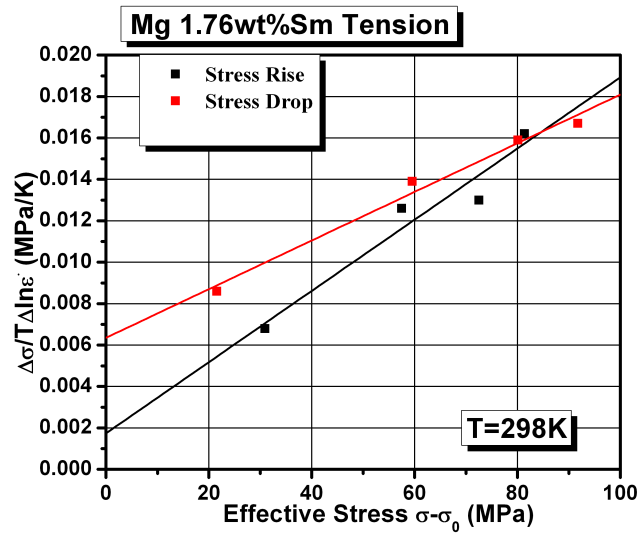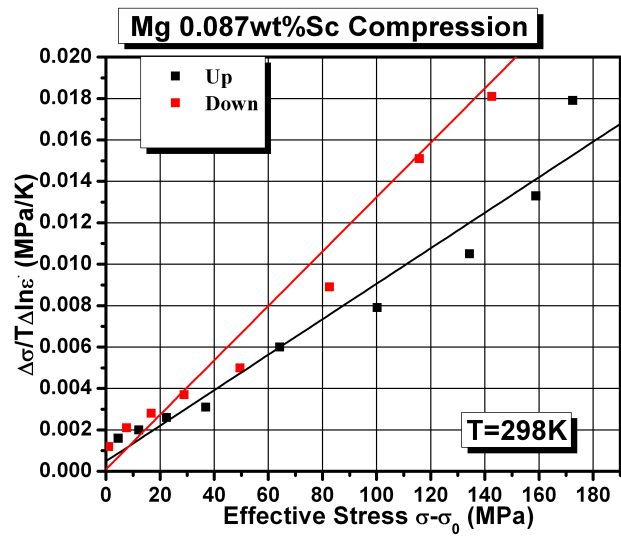
(a) Tension Haasen Plot for Mg-0.29 at% Sm
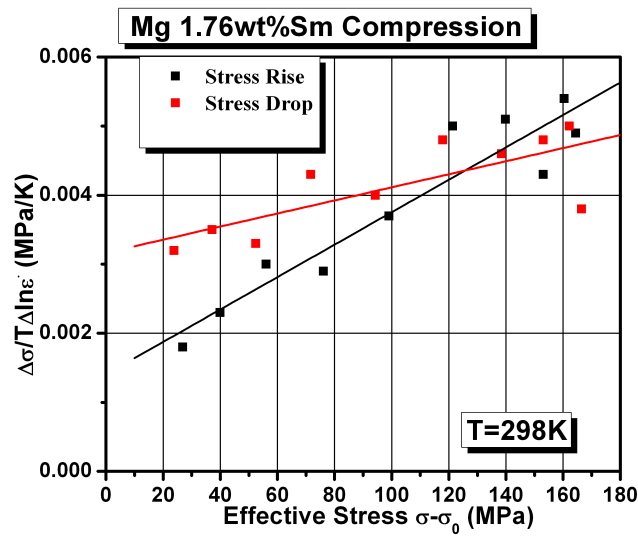
(b) Compression Haasen Plot for Mg-0.29 at% Sm
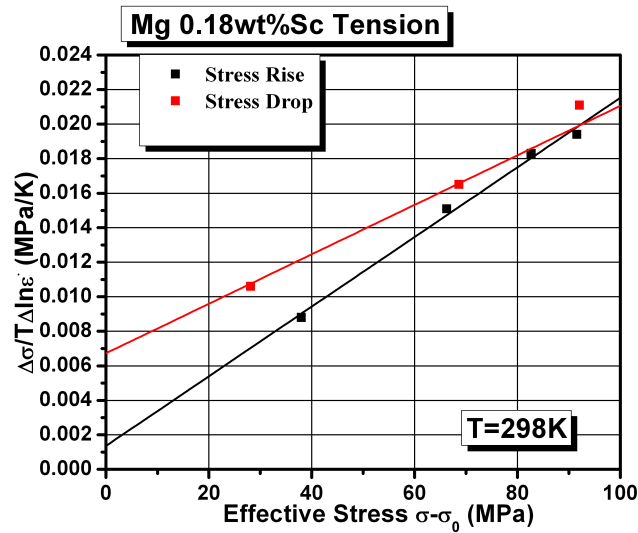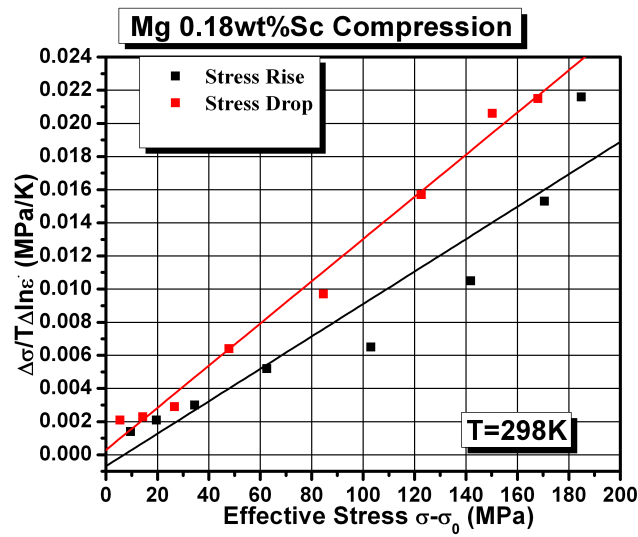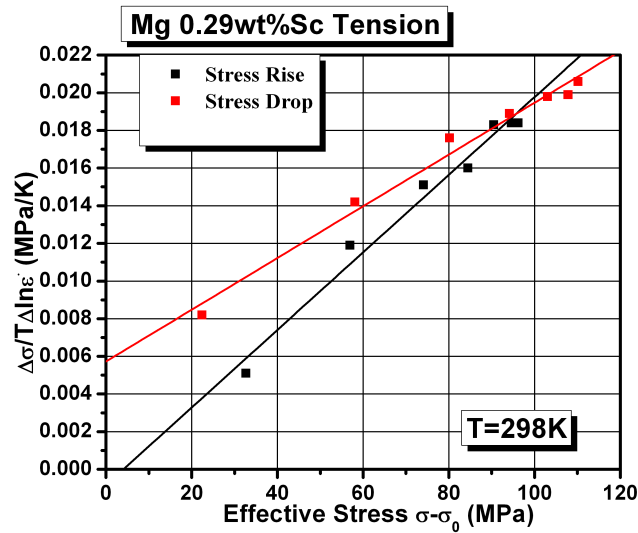
Figure 6.80: Haasen Plot for Mg-0.29 at% Sm
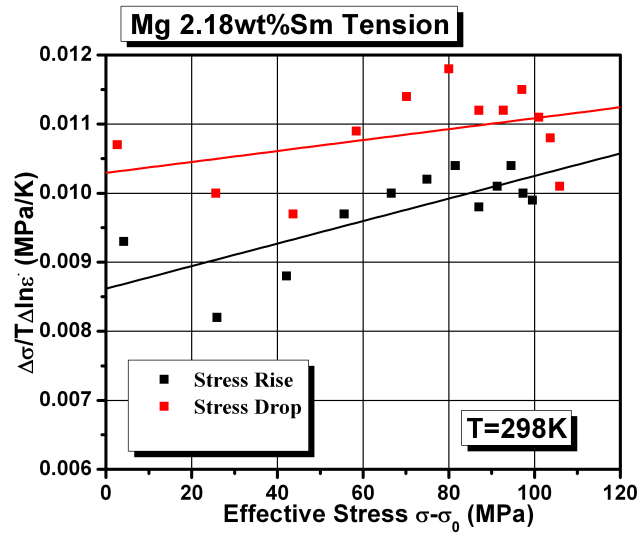
(a) Tension Haasen Plot for Mg-0.36 at% Sm
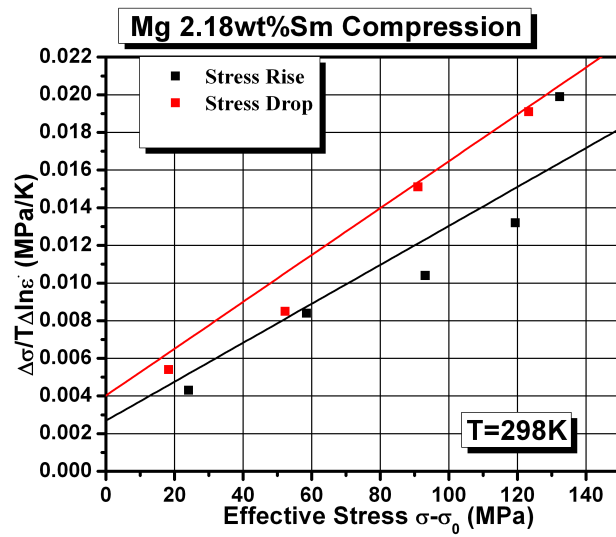
(b) Compression Haasen Plot for Mg-0.36 at% Sm

Figure 6.81: Haasen Plot for Mg-0.36 at% Sm

(a) Tension Haasen Plot for Mg-0.38 at% Sm

(b) Compression Haasen Plot for Mg-0.38 at% Sm

Figure 6.82: Haasen Plot for Mg-0.38 at% Sm

(a) Tension Haasen Plot for Mg-0.77 at% Sm

(b) Compression Haasen Plot for Mg-0.77 at% Sm

Figure 6.83: Haasen Plot for Mg-0.77 at% Sm

(a) Tension Haasen Plot for Mg-0.019 at% Sc

(b) Compression Haasen Plot for Mg-0.019 at% Sc

Figure 6.84: Haasen Plot for Mg-0.019 at% Sc
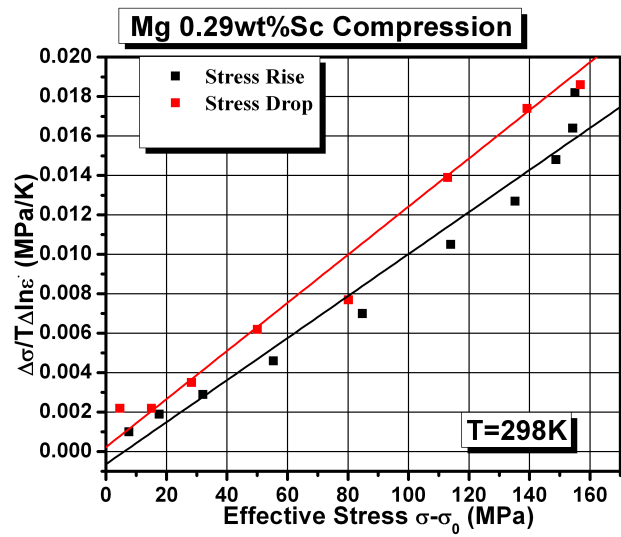
(a) Tension Haasen Plot for Mg-0.05 at% Sc

(b) Compression Haasen Plot for Mg-0.05 at% Sc

Figure 6.85: Haasen Plot for Mg-0.05 at% Sc

(a) Tension Haasen Plot for Mg-0.10 at% Sc

(b) Compression Haasen Plot for Mg-0.10 at% Sc
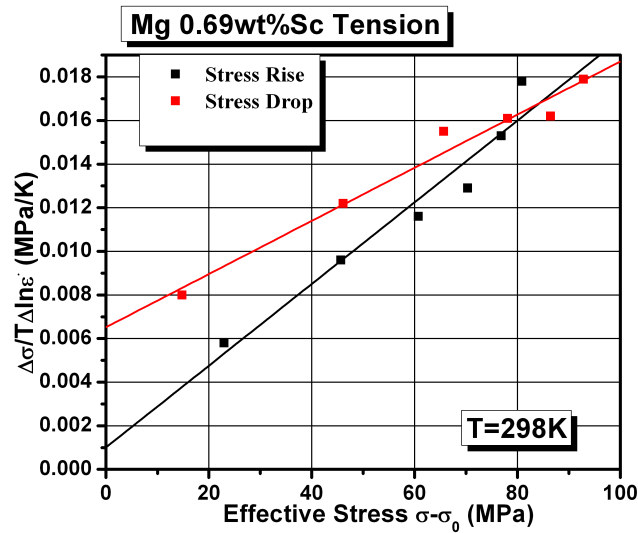
Figure 6.86: Haasen Plot for Mg-0.10 at% Sc
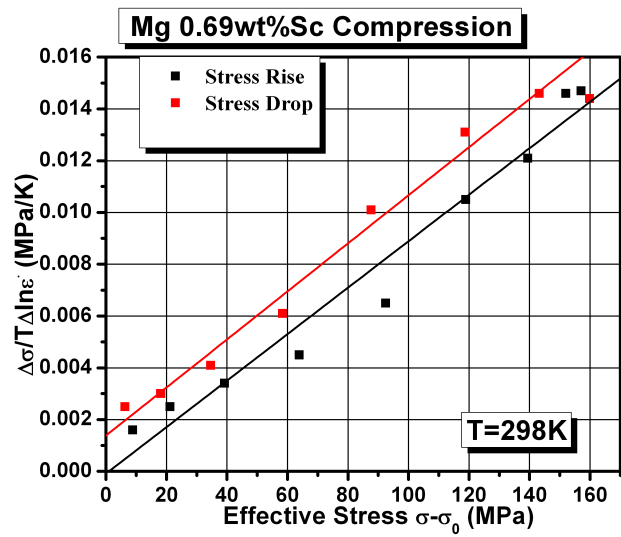
(a) Tension Haasen Plot for Mg-0.16 at% Sc

(b) Compression Haasen Plot for Mg-0.16 at% Sc
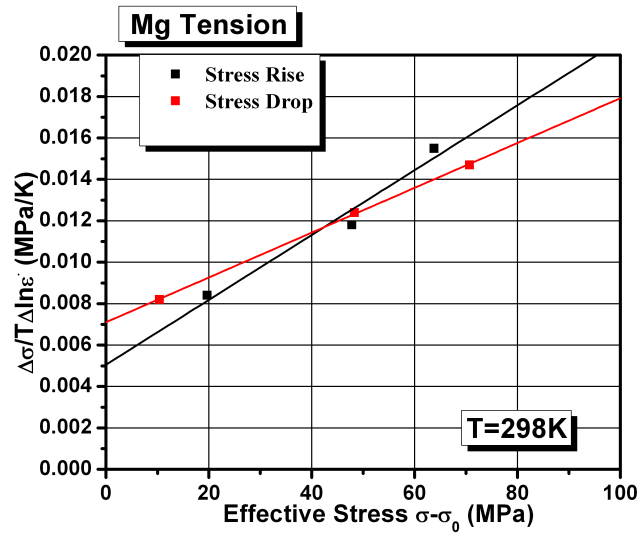
Figure 6.87: Haasen Plot for Mg-0.16 at% Sc

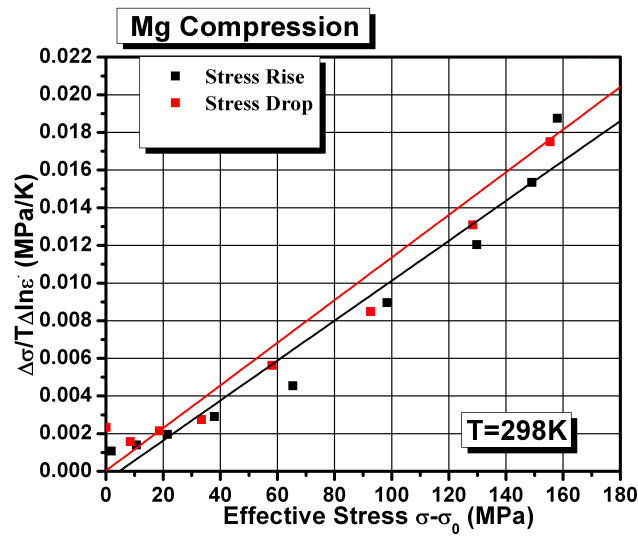(a) Tension Haasen Plot for Mg-0.31 at% Sc

(b) Compression Haasen Plot for Mg-0.31 at% Sc

Figure 6.88: Haasen Plot for Mg-0.31 at% Sc

(a) Tension Haasen Plot for Mg

(b) Compression Haasen Plot for Mg

Figure 6.89: Haasen Plot for Mg